

THE MECHANISM OF B.O.F. FUME FORMATION

by



FRED GOETZ, B.A.Sc.

A Thesis

Submitted to the School of Graduate Studies

in Partial Fulfilment of the Requirements

for the Degree

Master of Engineering

McMaster University

April, 1980

THE MECHANISM OF B.O.F. FUME FORMATION

MASTER OF ENGINEERING (1980),  
(Metallurgy and Materials Science)

McMASTER UNIVERSITY  
Hamilton, Ontario

TITLE: The Mechanism of B.O.F. Fume Formation

AUTHOR: Fred Goetz, B.A.Sc. (University of Toronto)

SUPERVISOR: Dr. D.A.R. Kay and Dr. D. Cosma

NUMBER OF PAGES: xii, 186

## ABSTRACT

An industrial B.O.F., located at the #1 Melt Shop of Dominion Foundries and Steel Ltd., was used to develop and evaluate a method of measuring the rate of fume emissions during steelmaking.

The fume rate was observed to decrease with increasing time into the blow. Approximately 60% of the total fume iron losses are emitted during the first one-third of the blowing time. The fume rate is influenced by such process variables as: metal carbon content, slag volume, metal temperature and lance practice.

The mechanism of fume formation was assessed using the size, shape and chemical analyses of the fume material. The major mechanism is that of the explosive oxidation of metal droplets in the oxygen impact zone. Evidence of vaporization was also observed, but this represented less than 10% (by weight) of the total fume iron losses during the blowing period.

## ACKNOWLEDGEMENTS

The author wishes to thank Dominion Foundries and Steel Ltd. for sponsoring this research project and for the extensive use of plant facilities and equipment.

The author also wishes to express his gratitude to the following:

Dr. D. Cosma, the research supervisor at Dofasco, for his continued guidance throughout all phases of the work.

Dr. D.A.R. Kay, the research supervisor at McMaster, for his guidance in the project.

Dr. B.A. Strathdee, Research Manager - Steelmaking, Dofasco, for his assistance and encouragement.

Fred Smith and Fred Pearson, McMaster technicians, for their assistance with the Transmission Electron Microscope.

Helen Lefebvre for her careful typing.

## TABLE OF CONTENTS

	<u>Page</u>
1. Introduction	1
2. Literature Survey	3
2.1 Industrial Fume Collection Systems	3
2.2 Classification of Fume by Size	11
2.3 Mechanism of Fume Formation	14
.1 Direct Vapourization of Iron	14
.2 Oxidation of Metal Spray from CO Bubbles	22
.3 Oxidation of Metal Spray from the Impact of the Oxygen Jet	33
.4 Influence of Bath Velocity	42
2.4 Fume from Industrial B.O.F.s	45
.1 Quantity, Size and Chemical Analysis	45
.2 Influence of Bath Carbon and Slag Volume	50
3. Design and Evaluation of Fume Sampling Device	56
3.1 The Gas Cleaning System	56
3.2 Sampling Location and Conditions	59
3.3 Description of Sampling Device	64
3.4 Effectiveness of Filter Canisters	75
3.5 Sample Reproducibility	78
3.6 Sample Representivity	82
4. Method and Results	87
4.1 Fume Weight versus Blowing Time	87
4.2 Chemical Analysis of Fume	91

	<u>Page</u>
4.3 Total Iron in Fume versus Bath Carbon	99
4.4 Total Iron in Fume versus Slag Weight	101
4.5 Effect of Scrap Quality	103
4.6 Microscopic Examination of Fume	108
4.7 Size Distribution of Fume Material	114
.1 Method and Accuracy	114
.2 Size Analysis Results	119
4.8 Relation Between Fume and Metallic Ejections	124
.1 Fume and Slopping	124
.2 Fume and Metallic Ejection	128
5. Discussion	131
5.1 Quantity and Chemical Analysis of Fume	131
5.2 Fume and Metallic Ejections	134
5.3 Quantity of Vapourization Fume	148
6. Conclusions	157
Bibliography	159
Appendix A	164
Appendix B	168
Appendix C	172
Appendix D	176
Appendix E	184

## LIST OF FIGURES

	<u>Page</u>
1. Combustion control in B.O.F. waste gas treating systems	5
2. Open hood gas collection systems	7
3. Closed hood gas collection system	8
4. Capital cost of CO-system	8
5. Operating cost of CO-system	9
6. Particle size of iron oxide fumes in various processes	12
7. Vapour pressure of iron and manganese as a function of temperature	15
8. Electron microscope photograph of vapourization fume particles	20
9. Manganese content of fume compared to that of bath (for vapourization)	20
10. Fume rate versus carbon content of melt	24
11. Droplet spray generated by bursting bubbles	26
12. Decarburization of Fe-C droplets in oxygen	29
13. Electron microscope photo of fume produced during carbon boil	31
14. Comparative geometry of various jet flow modes	34
15. Splash patterns with increasing jet flow	36
16. Splash patterns with different foam conditions	36
17. Splash patterns with different bath flow rates	36
18. Metal ejections being oxidized in the jet impact zone of a small scale BOF.	38
19. Effect of lance height on fume rate	38
20. Plot of jet penetration versus jet momentum	41



	<u>Page</u>
21. B.O.F. fume rate versus metal superheat	43
22. B.O.F. fume rate versus blowing time	49
23. Electron microscope photograph of B.O.F. fume	49
24. B.O.F. fume rate versus metal carbon content	51
25. Variation in B.O.F. slag height and volume during a blow	51
26. Sections through a B.O.F. converter at various stages of the blow	52
27. B.O.F. fume rate versus slag condition	55
28. Effect of slag and metal splash height on B.O.F. fume rate	55
29. #1 melt shop dust collection system	57
30. Location of fume sampling	60
31. Effect of damper configuration on gas velocity in the down duct	60
32. Results of Pitot tube measurements	62
33. Effect of error in sampling velocity on accuracy	65
34. Arrangement of simple sampling setup	65
35. Diagram of fume sampling device	70
36. Front, side and rear view of fume sampling device	72
37. Canister holder and filter canisters	73
38. Filter canisters installed in sampling device	73
39. Sampling device mounted on down duct	74
40. Dual samplers for representivity tests	74
41. Fume weight and gas velocity versus duct position	85
42. Fume weight versus blowing time	89
43. Fume analysis versus blowing time	94

	<u>Page</u>
44. Total iron in fume versus blowing time	95
45. Mn/Fe ratio versus blowing time	98
46. Total iron in fume versus bath carbon	100
47. Total iron in fume and slag weight versus blowing time	102
48. Effect of scrap quality on fume weight	106
49. Metal temperature versus blowing time	107
50. Scanning electron microscope photograph of 12-minute fume material	109
51. Transmission electron microscope photograph of 12-minute fume (1000x)	112
52. TEM photograph of fume particles (10000x)	112
53. TEM photograph of fume particles (20000x)	112
54. TEM photograph of fume particles (40000x)	113
55. TEM photograph of fume particles (80000x)	113
56. Typical frequency and weight distributions	115
57. Reproducibility of size analysis	117
58. Comparison of fume size distributions at various blowing times	120
59. Size comparison of pre-ignition, decarburization and reblow fume	122
60. Comparison of slopping and not-slopping fume size distributions	127
61. Fume weight versus metallic ejections	130
62. Decarburization rate versus blowing time	141
63. Plot of maximum size of metal droplet that can be entrained in the off-gas stream	142
64. Fume and ejection rates versus blowing time	144
65. Mn/Fe ratio and decarburization rate versus blowing time	152

LIST OF TABLES

	<u>Page</u>
I. Comparison of Main Process Data for 10, 30 and 100% Combustion	5
II. Summarized Operating Cost for CO-System	9
III. Calculated and Measured "Hot Spot" Temperatures	17
IV. Mn/Fe Ratio in Vapourization Fume	21
V. Calculated Jet Penetration for Dofasco Blowing Practice	41
VI. Chemical Composition of Dust in B.O.F. Gases	47
VII. Effect of Incorrect Sampling Velocity	68
VIII. Quantity of Fume Collected in 2nd and 3rd Canisters	76
IX. Fume Weight Collected at 20 Minute Mark	80
X. Reproducibility of Results	81
XI. Fume Weights at Various Positions Across Duct	83
XII. Fume Weight Versus Blowing Time	88
XIII. Reblow Fume Weight	90
XIV. Fume Analysis at Various Blowing Times	93
XV. Total Iron in Fume Versus Blowing Time	95
XVI. Level of Significance of Iron and Manganese Analysis	96
XVII. Mn/Fe Ratio in Bath and Fume	97
XVIII. Total Iron in Fume Versus Bath Carbon	100
XIX. Total Iron in Fume and Slag Weight Versus Blowing Time	102
XX. Fume Weight for Different Scrap Types	105

	<u>Page</u>
XXI. Reproducibility of Size Analysis	118
XXII. Summary of Size Distributions	123
XXIII. Fume Weight at 15 Minutes (Stopping, Not Stopping)	125
XXIV. Average Fume Weight and Iron in Metallic Ejections	129
XXV. Mn/Fe Ratio and Weight % $< 0.2 \mu\text{m}$ for Decarburization Period Fume	156

LIST OF SYMBOLS

<u>Symbol</u>	<u>Description</u>	<u>Units</u>
a	depth of penetration	m
d <sub>j</sub>	nozzle diameter	m
h	lance height	m
G	gravitational constant (9.81)	m. sec. <sup>-2</sup>
K	constant	
M	jet momentum	kg
Q	gas flow rate	m <sup>3</sup> . sec. <sup>-1</sup>
V <sub>c</sub>	centre line jet velocity	m. sec. <sup>-1</sup>
V <sub>j</sub>	jet velocity at nozzle	m. sec. <sup>-1</sup>
Y <sub>l</sub>	density of liquid	kg. m. <sup>-3</sup>
Y <sub>g</sub>	density of gas	kg. m. <sup>-3</sup>

## 1. INTRODUCTION

Basic oxygen steelmaking was developed in the early 1950's in Austria and now accounts for 55 percent of international steelmaking capacity. The basic advantages of this process are:

- i) speed of refining
- ii) economy of labour
- iii) lower capital requirements (assuming availability of molten pig iron)

An important problem associated with the B.O.F. process is the production of large quantities of fume. The amount of fume emitted ranges from 10 to 30 kg·tonne<sup>-1</sup> of steel produced, and a large percentage of this material is in the highly visible submicron size. A typical B.O.F. shop can produce upwards of 100 tonnes of fume material per day. This represents both a metallic yield loss and a serious air pollution problem, while the equipment necessary for fume collection and handling represents a significant capital investment and operating cost to the plant.

The usual appearance of oxygen steelmaking fume is the orange-brown ferric oxide (Fe<sub>2</sub>O<sub>3</sub>) which occurs in open hood gas collection systems where there is ample air entrainment into the waste gases to fully burn the CO present to CO<sub>2</sub>. In the case of closed hood gas collection systems where a minimum of air entrainment takes place, black fume containing predominantly metallic iron and ferrous oxide (FeO) is produced.

Two mechanisms for the formation of fume during B.O.F. steelmaking have been suggested. The first mechanism proposed is that fume is a result of the direct vaporization of iron which occurs in the high temperature region ("hot spot") where the oxygen jet impinges on the molten-iron surface. This iron vapor is then oxidized by the incoming oxygen jet. The second mechanism suggests that the major cause of fume is the oxidation and vaporization of iron droplets that are ejected from the liquid iron bath either by the mechanical force of the oxygen jet or by bubbles of CO bursting through the melt surface.

The aim of this work was to determine the relative importance of these two proposed mechanisms of fume formation in an industrial B.O.F. The furnace studied was located in the No. 1 Melt Shop of Dominion Foundries and Steel, Limited. The gas collection system on this particular furnace is of the open hood type.

A device was developed to take samples of the fume material from the B.O.F. exhaust gases during the course of refining. Tests were conducted to determine the reproducibility and representivity of this device. Information about the origin of the fume particles was gathered from their weight, chemical analysis and a microscopic examination of their size and shape.

## 2. LITERATURE SURVEY

### 2.1 Industrial Fume Collection Systems

The fume and dust formed during B.O.F. steelmaking is of considerable interest because it represents both a loss in metallic yield for the process and a serious source of air pollution. The quantity of iron lost as fume ranges from 0.7 to 2.0%<sup>1-4</sup> of the steel weight produced. A typical B.O.F. plant will produce from 100 to 200 tonnes of fume material per day<sup>5</sup>.

Dust loading in the furnace off-gases ranges on average from 40 to 80 g/Nm<sup>3</sup> <sup>2,6-8</sup> with periods of peak loading reaching 250 g/Nm<sup>3</sup><sup>6</sup>. Local air quality regulations require that plant emissions not exceed 0.01 g/Nm<sup>3</sup><sup>9</sup> and similar limits exist throughout the industrialized world. For example, the limit in Japan is also 0.01 g/Nm<sup>3</sup><sup>7</sup>. To meet these regulations, dust collecting efficiencies in the order of 99.9% are required.

In general, B.O.F. gas collection systems can be classified into two categories:

- i) open hood
- ii) closed hood

2 With an open hood system, a large amount of atmospheric air is drawn into the collection system along with furnace off-gases. The quantity of atmospheric or "excess air" entrained can range from 100 to 400 percent of that



necessary for combustion of all of the CO present in the furnace off-gases. The temperature of the gases leaving the furnace at approximately  $1500^{\circ}\text{C}^{10-12}$  is increased by this combustion process and has been calculated<sup>13,14</sup> to range from 1900 to  $2500^{\circ}\text{C}$  in the hood, depending on the quantity of excess air present.

Table I shows a comparison of the main process data for 10%, 30% and 100% combustion of the primary gases at the furnace mouth. It can be seen that with increasing excess air the gas temperature in the hood also increases. This means that more heat must be removed from the gases before they enter the cleaning stage of the system. More powerful fans are also required to handle these larger gas volumes, thus increasing both investment and operating costs. Open hood systems were the first to be used in B.O.F. plants and are still in use today.

The majority of the plants designed in the past five years use closed hood systems where the amount of excess air is limited to 5 to 70% of that needed for total combustion of the CO. Principle advantages as seen in Table I are lower gas temperature and volume which means reduced capital and operating cost. Another significant benefit is that part of the CO emitted can be recovered and used as fuel. The most common method to reduce the amount of excess air entrained is the use of a movable

TABLE I

COMPARISON OF MAIN PROCESS DATA FOR  
10, 30 AND 100% COMBUSTION [13]

Combustion Rate	100%	30%	10%
Total gas volume (Nm <sup>3</sup> /h)	223,000	123,000	94,000
Theoretical gas temperature inlet hood	2400°C	2200°C	1600°C
Heat to be removed in hood (Million kcal/h)	187	70	35
Fan horse power (high energy scrubber)	3500 kw	1900 kw	1400 kw

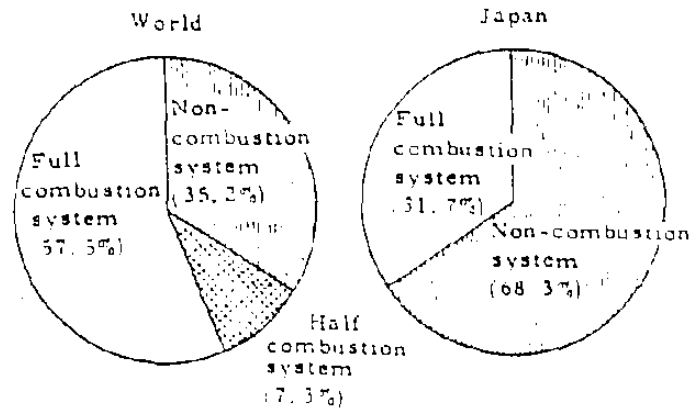


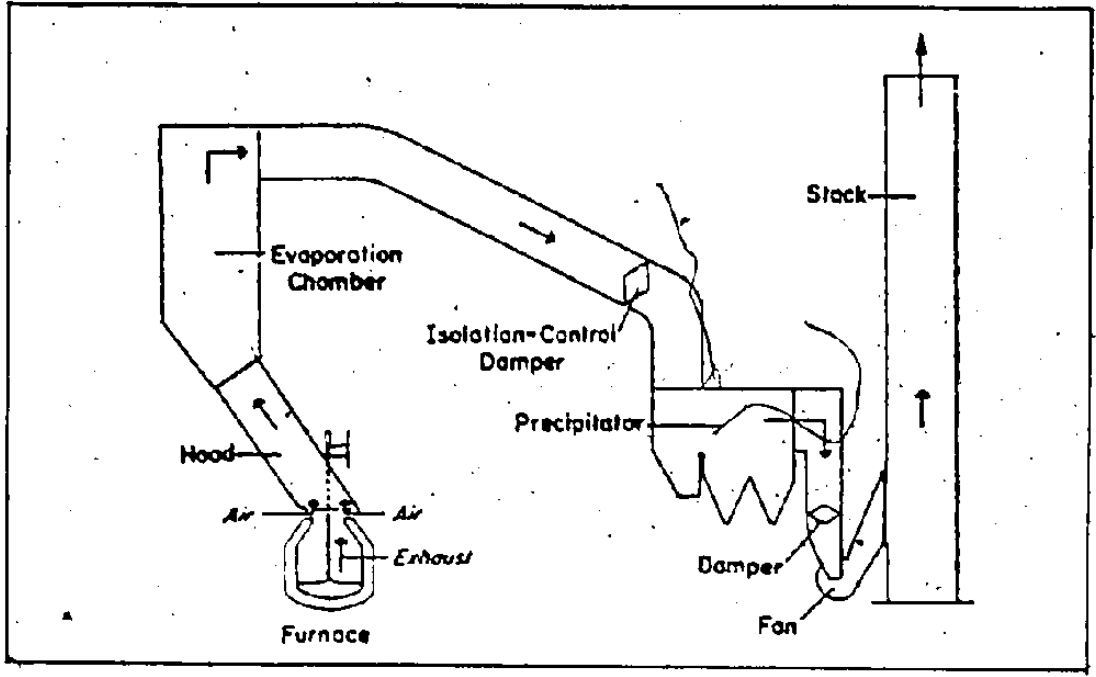
Fig. 1: Combustion control in the B.O.F. waste gas treating system (whose furnace capacity is over 100 T) (excluding communist countries) [7]

section of hood called a "skirt" that drops around the vessel mouth during the blow to form a restriction for the entering air. Since the CO is not completely combusted, special care must be taken to prevent explosions from occurring within the hood and gas cleaning system. Figure 1 shows the percent usage of these two types of gas collecting systems.

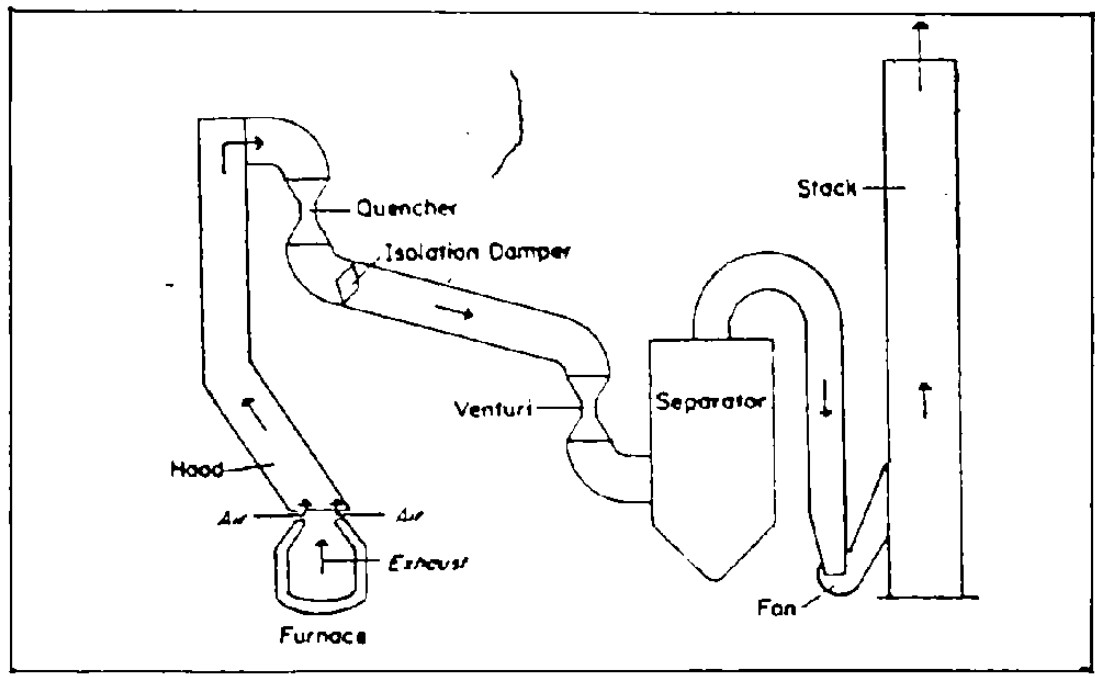
B.O.F. fume is very fine, in the order of  $1\ \mu\text{m}$  and smaller. The only equipment that can handle particles this size in the dry state are electrostatic precipitators. Though some B.O.F. plants use this equipment they are costly to purchase and maintain and handling of the dry dust collected is difficult. The present trend is towards wet cleaning systems, where in the majority of cases, venturi scrubbers are used. The action of these scrubbers cause the fume particles to be suspended in water droplets which are easier to collect due to their larger mass. This water is then sent to a thickener where the solids are recovered as sludge and the cleaned water is recycled.

Two typical open hood gas collection and cleaning systems are shown in Figure 2. A typical closed hood system is shown in Figure 3.

The appearance of the iron in the fume material is related to the type of gas collecting systems used. In open hood systems, the iron fraction is approximately 85%



A) Dry System



B) Wet System

Fig. 2: Open Hood Gas Collection Systems [15]

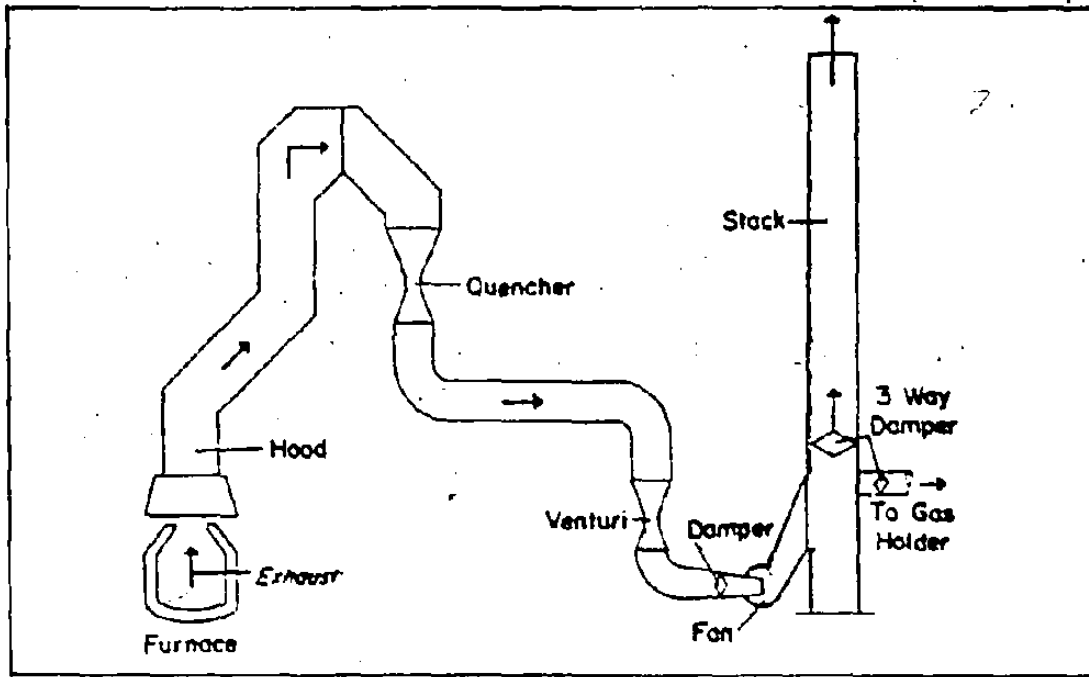


Fig. 3: Closed Hood Gas Collection System [15]

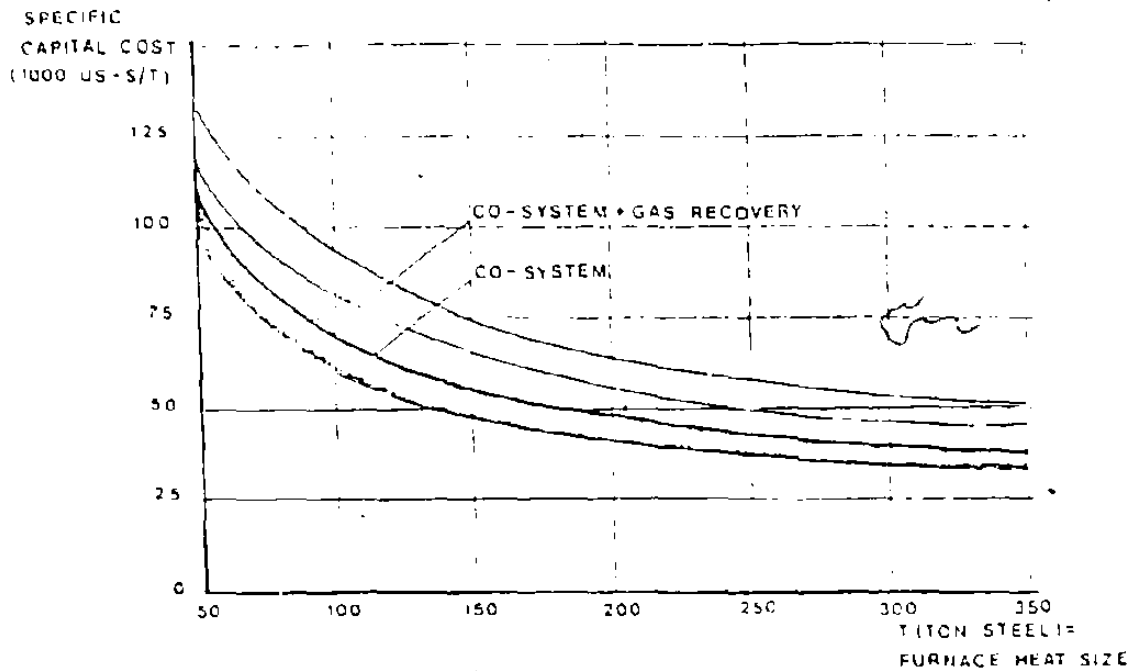


Fig. 4: CAPITAL COST OF CO-SYSTEM FOR TWO FCE BOP SHOP [13]

$\text{Fe}_2\text{O}_3$ , 15%  $\text{FeO}$ , less than 1% metallic iron and is orange-brown in colour<sup>2,3,6</sup>. With closed hood systems, the fume is black in colour, and the iron fraction is approximately 10% metallic, 55%  $\text{FeO}$  and 35%  $\text{Fe}_2\text{O}_3$ <sup>6,7</sup>.

These gas collection and cleaning systems represent a significant cost factor for a steel plant. Cost data based on a closed hood system<sup>13</sup> operating at 10% excess air are shown in Figures 4-5. Figure 4 shows the specific capital cost per ton of furnace capacity for a two-furnace shop (1977 U.S. dollars). For a 2 x 250 ton B.O.F. shop, the specific capital cost is approximately \$13 million in the order of 10-15%<sup>15</sup> of the shop cost. If equipment is installed to recover the CO in the off-gases, the capital cost is approximately 35% higher. Figure 5 shows the operating cost of such a system based on two vessel B.O.F. shop producing 24,000 heats per year. As in Figure 4, costs decrease with increasing furnace size but range from \$1 to \$2 per ton of steel produced. These costs represent those for the most energy efficient systems. Capital and operating costs for open hood systems with their hotter temperatures and larger gas volumes would be more.

Table II shows a breakdown of the operating cost for the above-mentioned system.

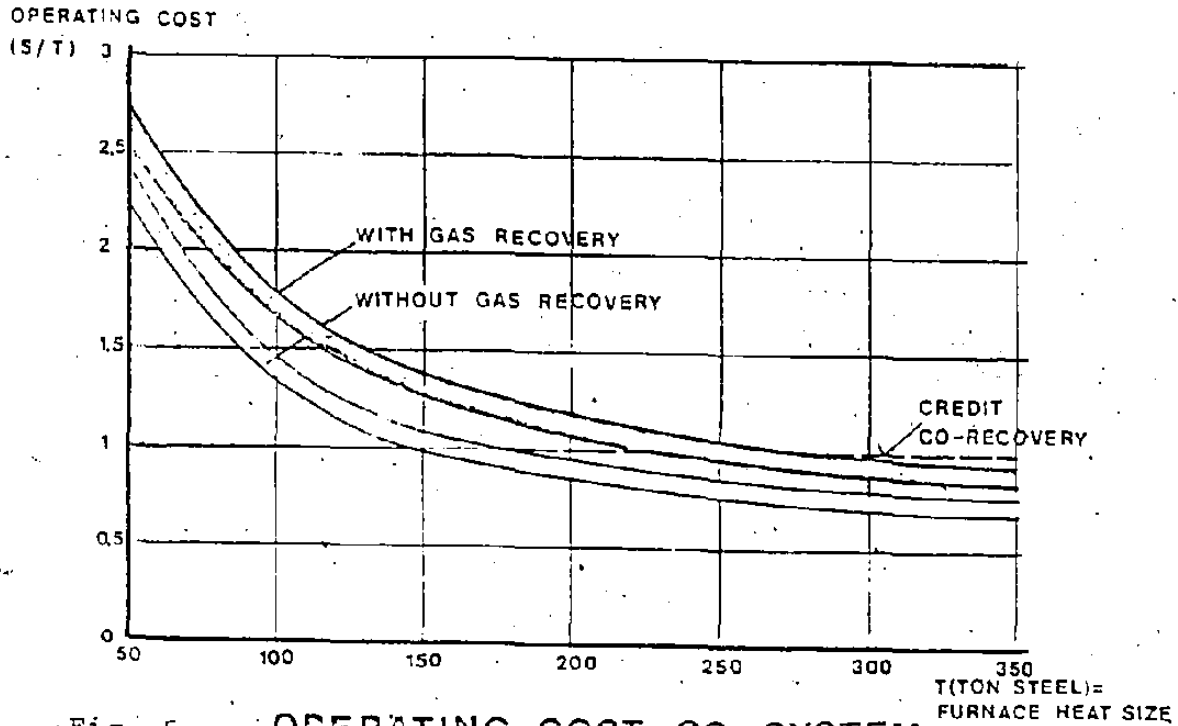


Fig. 5: OPERATING COST CO-SYSTEM.  
FOR TWO F'CE BOP SHOP [13]

TABLE II

SUMMARIZED OPERATING COST FOR CO-SYSTEM 2x200 T BOP [13]

COST FACTORS	CO-SYSTEM		CO-SYSTEM WITH GAS RECOVERY	
	US \$/T	%	US \$/T	%
UTILITIES	0,12	13	0,13	11
POWER	0,13	15	0,15	14
PERSONNEL	0,13	15	0,13	11
MAINTENANCE & REPAIR	0,07	8	0,10	9
CAPITAL	0,45	49	0,63	55
TOTAL	0,90	100 %	1,14	100 %

## 2.2 Classification of Fume by Size

It has been well documented<sup>16-18</sup> that metal droplets ranging in size from 1  $\mu\text{m}$  to 1 mm exist in B.O.F. slags during and after refining. The predominant source of these droplets are considered to be the shearing of the metal bath by the oxygen jet<sup>19,20</sup> and metal being carried across the metal and/or slag interface as a coating on CO bubbles<sup>21-23</sup>. Many of these droplets are small enough to be carried out of the furnace by the force of the exhaust gases. Laciak<sup>24</sup> has done an extensive study into the nature and cause of these ejections from Dominion Foundries and Steel, Limited's basic oxygen furnaces. His results showed that these particles ranged in size from 10-300  $\mu\text{m}$ , the majority being between 15 and 45  $\mu\text{m}$  in diameter. These particles are spheres of metallic iron having an oxide coating 5-15  $\mu\text{m}$  thick<sup>(3,24)</sup>.

Fume particles on the other hand are much smaller, the majority of particles being less than 1  $\mu\text{m}$  in diameter independent of the oxygen~~s~~teelmaking method as seen in Figure 6. The structure of these particles depends on the amount of excess air that is drawn into the exhaust gas collecting hood. As mentioned before, in open hood systems, the fume is predominantly orange-brown  $\text{Fe}_2\text{O}_3$  and in closed hood systems, the fume is metallic iron and  $\text{FeO}$ .



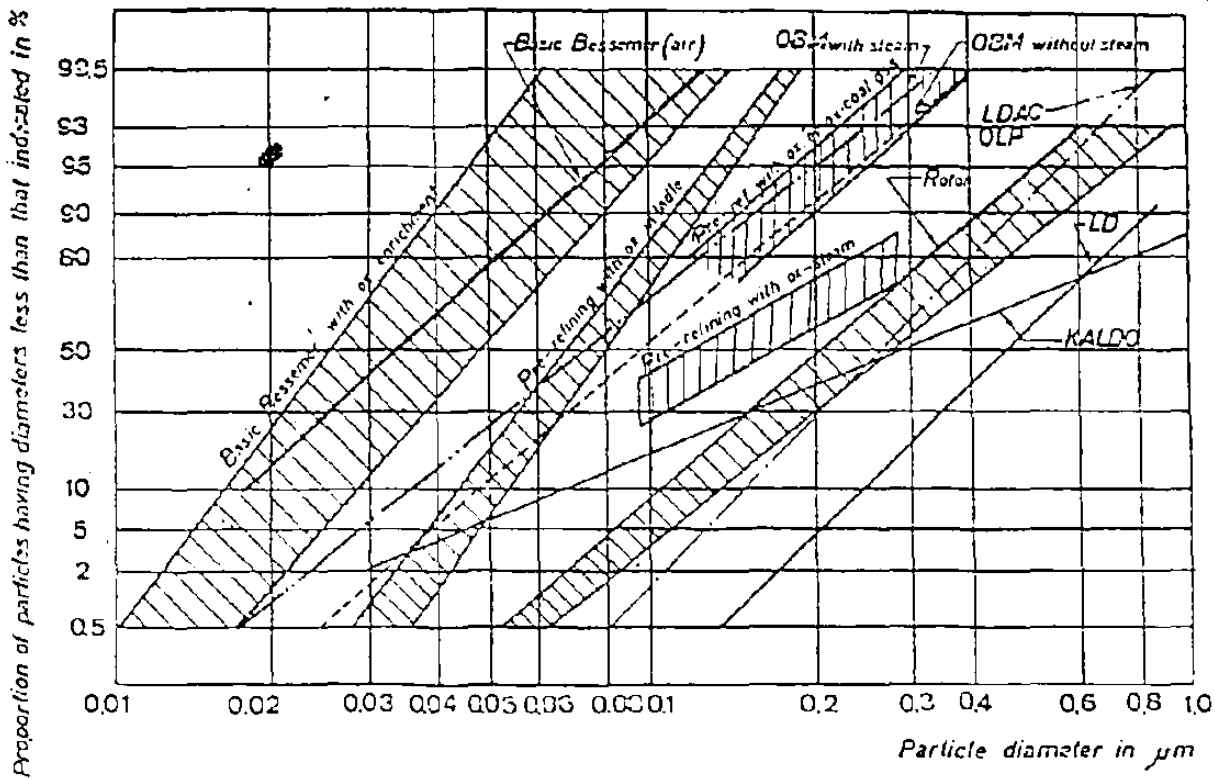


Fig. 6: Particle size of iron oxide fumes in various processes. [14]

Ellis & Glover<sup>25</sup> noted that in industrial practice particles with sizes greater than 5  $\mu\text{m}$  can be effectively removed from waste gases using low cost cyclones, but the cost of removing smaller particles is relatively expensive. For this reason they defined fume as being all particles less than 5  $\mu\text{m}$  in diameter.

The above definition will be used in this work.

## 2.3 Mechanisms of Fume Formation

### 2.3.1 Direct Vaporization of Iron

At steelmaking temperatures (1600°C), the vapor pressure of pure iron is approximately  $10^{-4}$  atm, but it increases rapidly with increasing temperature as shown in Figure 7. At 2400°C the vapor pressure of iron is approximately  $10^{-1}$  atm and the vaporization temperature is 2860°C.

When oxygen is blown onto the surface of an iron bath, it will be adsorbed almost instantly. Reaction products will appear as a result of the momentarily high oxygen concentration, and if carbon is oxidized, a bubble of CO will form. It is likely that the heats of reaction will produce high local temperatures making vaporization of iron possible.

Kosmider<sup>26</sup> has calculated that during oxidation of iron with pure oxygen, local interfacial temperatures of 3050°C can be reached. Bogdandy<sup>27</sup> calculated that if 30-40% O<sub>2</sub> enriched air was used, local temperatures could reach 2100 to 2600°C. This is in good agreement with measurements taken through the tuyeres of a Bessemer furnace by Naeser<sup>28</sup> who recorded temperatures of 2200°C using an optical pyrometer.

Measurements of the "hot spot" temperature at the metal surface in the oxygen impingement zone have also

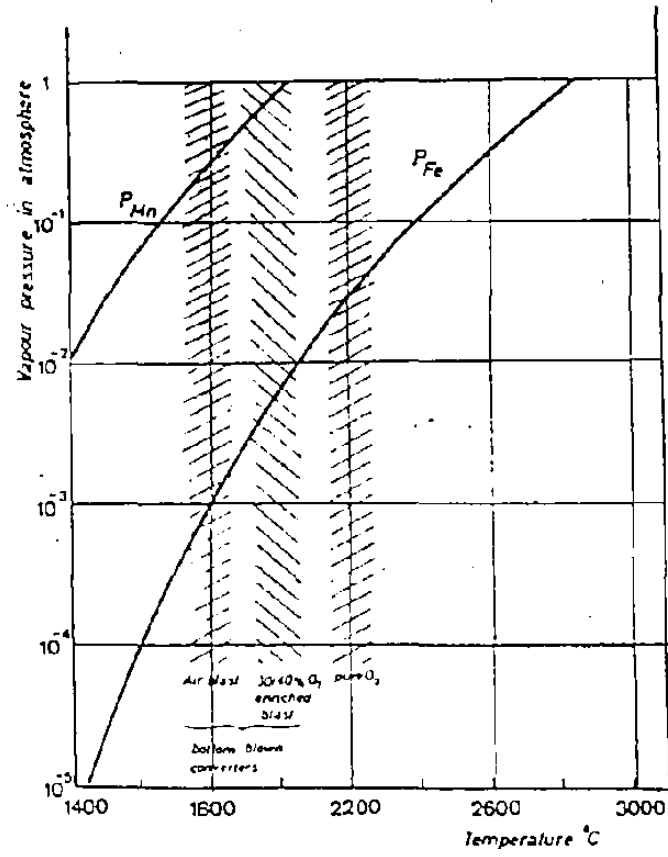


Fig. 7: Vapor pressure of iron and manganese as a function of temperature. Temperature ranges of the impingement zones are shown, conforming with Table III [14]

been made using optical pyrometry or photometric techniques. The accuracy of these type of measurements can be affected by the presence of any slag cover on the surface of the bath or by the presence of dust and fume in the gas phase. However, the results of both lab and industrial measurements indicate that in the B.O.F., "hot spot" temperatures range from 2200 to 2600°C<sup>29-32</sup> or 600-1000°C in excess of the bulk bath temperature (these results are summarized in Table III). It appears possible then that direct vaporization of iron could be the cause of fume formation during B.O.F. steelmaking.

Using thermodynamic<sup>33</sup> data, the calculated vapor pressure of FeO is  $2 \times 10^{-5}$  atm at 1600°C and increases to approximately  $2 \times 10^{-2}$  atm at 2400°C, values which are about five times smaller than those for Fe at the same temperatures. These calculated pressures are not very accurate because the heat of formation of (FeO)g is not well established; values determined range from -47 to -65 kcal/mole<sup>33</sup>. Other experimental data<sup>27,35,36</sup> indicates that the vapor pressures of FeO and Fe are very close in this temperature range. Wortenberg<sup>36</sup> has observed that iron oxide vaporizes at approximately 1800°C, a temperature that has already been shown to exist in the B.O.F. This would suggest that the iron

TABLE III

Calculated and Measured "Hot Spot" Temperatures

Author	Temp. °C	Comments	Ref.
Kosmider	3050	Calculated assuming oxidation of iron in pure O <sub>2</sub>	26
Kosmider	2650	Calculation assuming oxidation of iron in 40% O <sub>2</sub> enriched air	26
Von Bogdandy	2100	Calculation for 30% O <sub>2</sub> enriched air	27
Naeser	2200	Optical pyrometer measurement through tuyere of Bessemer converter (O <sub>2</sub> enriched air)	28
Kawakami	2400- 2600	Spectroscope measurement, lab scale model	31
Urbain	2130	Optical pyrometer lab scale model	29
Kocho	2450	Optical pyrometer, industrial B.O.F.	30
Beitelman	2400- 2600	Optical pyrometer, industrial B.O.F.	32

oxide found in the fume could be a result of vaporization of liquid iron oxide as well as the subsequent oxidation of vaporized liquid iron.

Ellis and Glover<sup>25</sup> studied the vaporization of iron from Fe-4% C melts at low oxygen pressures (< .1 atm). The collected fume particles were observed using electron microscopy. The particles were octagonally shaped and ranged in size from .05 to .15  $\mu\text{m}$  in diameter. A typical electron-micrograph is shown in Figure 8, where the octagonal shape is clearly evident. A similar shape was also observed by Meldau<sup>37</sup> who vaporized Fe - .02% C melts in pure oxygen.

The shape of these particles is a result of the condensation of iron oxide vapor from the gas phase. Pure crystals of  $\text{Fe}_3\text{O}_4$  are octagonal in shape, whereas the crystal structure of  $\text{Fe}_2\text{O}_3$  is rhombohedral.

If fume particles are produced entirely by the condensation of vapor, then a highly volatile element should become enriched in the fume. One such volatile element commonly found in steelmaking is manganese. Between 1400 and 2100°C, the vapor pressure of manganese is 100 to 1000 times that of iron (See Figure 7).

Bogdandy and Pantke<sup>27</sup> collected fume that was produced by the vaporization of Fe-C-Mn melts, and their

results showed that the Mn/Fe ratio in the fume is on the order of 150 times the Mn/Fe ratio in the bulk (Figure 9). The results of Ellis and Glover<sup>25</sup> (Fe - Mn - 4% C) showed the Mn/Fe in the fume to be approximately 30 to 80 times the Mn/Fe in the bath for vaporizing conditions. The results of their experiments are listed in Table IV.



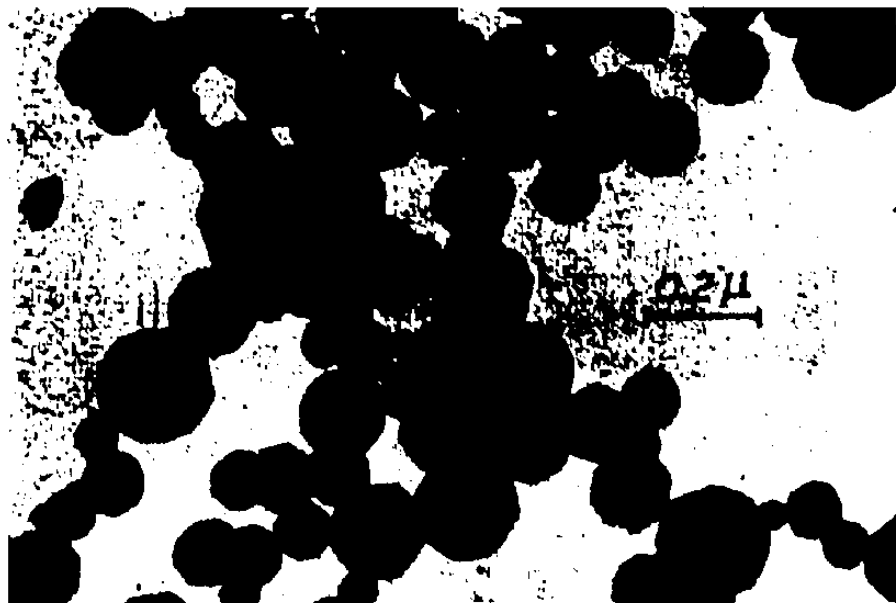


Fig. 8: Electron Microscope Photograph Of Vaporization Fume Particles [25]

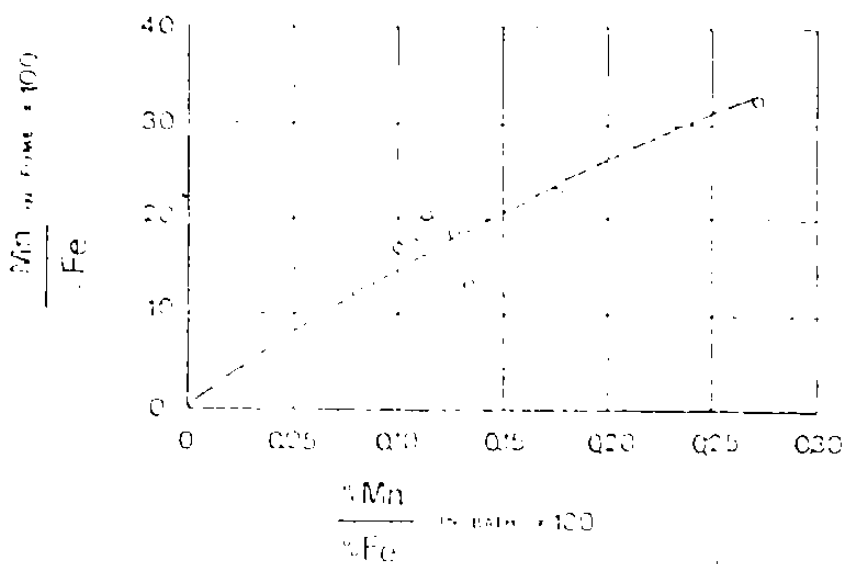


Fig. 9: Manganese content of fume, as compared to bath [27]

TABLE IV

MANGANESE TO IRON RATIO IN VAPORIZATION FUME [25]

Test	Wt. % C in Melt	Wt. % Mn in Melt	Wt. % Fe in Melt	Mn/Fe Melt	Mn in Fume (mg)	Fe in Fume (mg)	Mn/Fe Fume	Mn/Fe Fume Mn/Fe Melt
1	3.91	4.31	91.78	.047	7.5	5.0	1.50	31.91
2	4.31	4.47	91.22	.049	9.4	3.0	3.13	63.87
3	4.17	4.49	91.34	.049	10.1	3.0	3.37	68.77
4	4.35	4.20	91.45	.046	11.1	4.0	2.78	60.43
5	4.24	4.17	91.59	.045	10.1	3.0	3.37	74.88
6	0.00	4.12	95.88	.043	7.0	2.0	3.50	81.39
7	0.00	4.22	95.78	.044	11.5	3.0	3.83	87.04

W

### 2.3.2 Oxidation of Metal Spray from CO Bubbles

When studying the mechanism of the reduction of metallic oxides, Spandau and Kohlmeyer<sup>38</sup> noted that during the reduction of iron oxides by carbon and the oxidation of Fe-C melts by air or ferric oxide, volatilization of iron occurred. They reached the conclusion that the evolution of fume was brought about by the formation of an iron carbonyl which decomposed to iron and CO above the surface of the bath. This iron was then oxidized to fume by the oxygen present in the air.

A fair amount is known about the properties of iron pentacarbonyl ( $\text{Fe}(\text{CO})_5$ ). At  $25^\circ\text{C}$  its heat of formation from iron and CO is  $-0.3 \text{ kcal. kg}^{-1}$ , and its melting and boiling points are  $-21$  and  $105^\circ\text{C}$  respectively. This compound decomposes readily at moderately elevated temperatures, and it is unlikely that it can form at steelmaking temperatures ( $1600^\circ\text{C}$ ). In fact when CO is bubbled through Fe-C melts, no fume is observed<sup>34</sup>; therefore, this explanation for the effect of carbon on fume evolution can be disregarded.

Turkdogan<sup>34</sup> collected the fume evolved while blowing oxygen or air at low flow rates on Fe-C melts. His results indicate a strong relation between the quantity of fume evolved and carbon concentration in the melt;

the results are shown in Figure 10. The fume weight increased with increasing carbon in the melt and below 28 carbon in the melt, there was an appreciable reduction in the amount of fume evolved. These results are in agreement with those of Bates<sup>39</sup> and Morris et al<sup>22</sup> obtained under similar experimental conditions.

Morris et al<sup>22</sup> also noted that fuming was always accompanied by the formation of a metal spray above the surface of the bath. He concluded that since the soft jets used in the experiments did not have enough force to disrupt the bath surface, the spray must have resulted from CO bubbles breaking through the surface of the melt. Several other authors<sup>40-45</sup> have also suggested that fume formation could be the result of the oxidation of iron droplets formed as a result of CO bubbles bursting through the melt.

An understanding of how this spray is formed can be obtained from the observation of gas bubbles bursting through liquid surfaces. The schematic in Figure 11a shows what happens when an air bubble emerges from water<sup>52</sup>. The bubble first forms a hemispherical dome which ultimately bursts to give very fine droplets. This release of pressure leaves a crater behind and the inflowing liquid produces a jet which rises at high velocity and may detach large drops

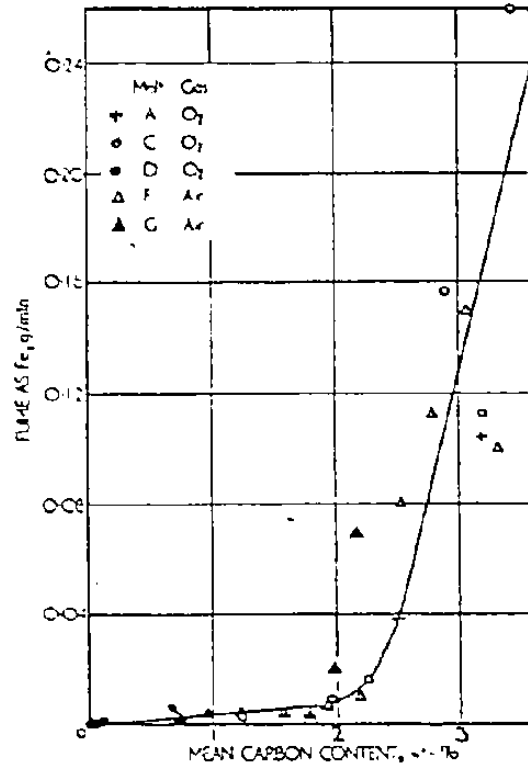
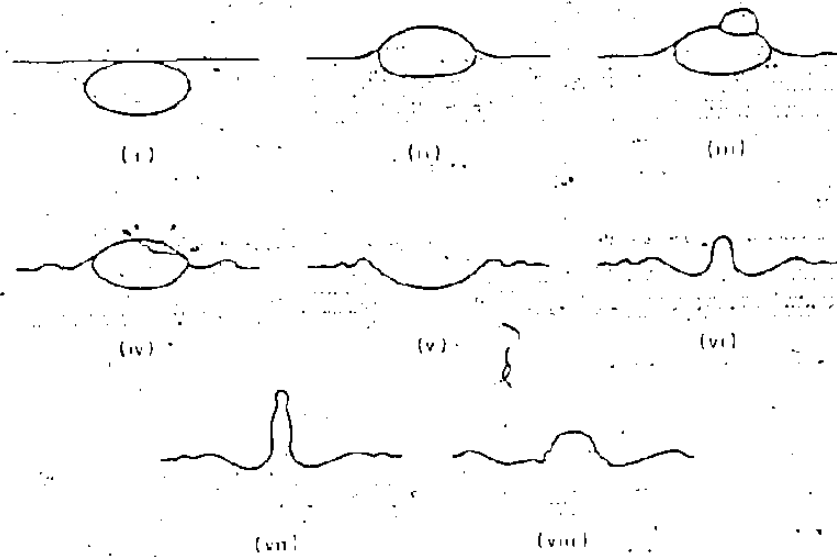


Fig. 10: Fume as total iron related to mean carbon content of 900-g melt (gas flow rate 500 ml/min) [34]

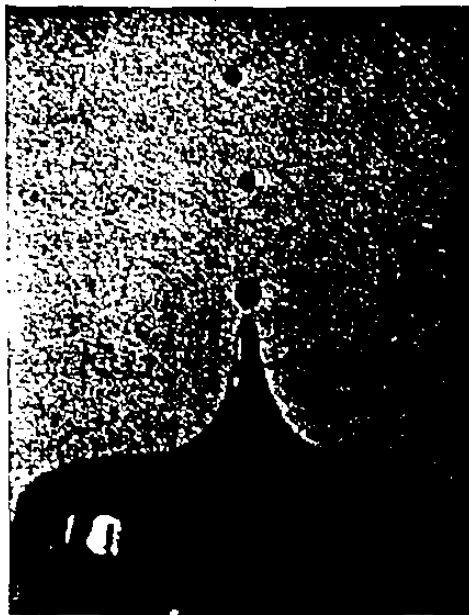
from its apex. Similar results from experiments with mercury (Figure 11b) and iron (Figure 11c) have also been recorded using high speed cine-film techniques.

It is well documented<sup>42-51</sup> that at high carbon contents, decarburization of Fe-C melts is the result of a surface reaction and that the rate of this reaction is limited only by the rate of oxygen transport in the gas phase. At lower carbon contents, decarburization becomes limited by the rate of transport of carbon and the reaction changes from surface to bulk generation of CO (a "CO boil"). The critical-carbon content for transformation from surface to bulk reaction can range from 2 to .5% C.

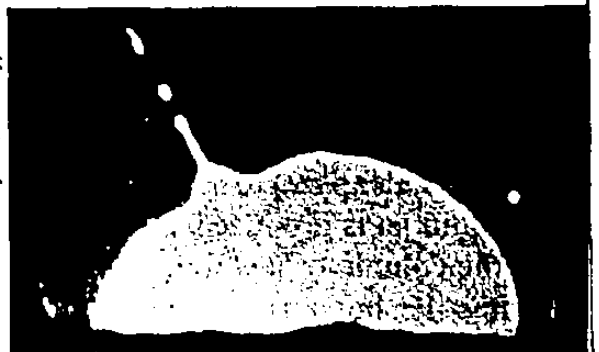
The value of the critical carbon content is related to the degree of bath agitation. If very little bath motion exists, as with a soft jet blowing on an iron melt held in a crucible, the major mechanism of carbon transport will be diffusion. Under this condition, the transition carbon content will be close to 2%<sup>49</sup>. When bath agitation is enhanced, as with iron droplets levitated in an electric field, bath circulation becomes a major factor in C transport. In this case, the critical carbon content is closer to .5%<sup>44</sup>.



(a)



(b)



(c)

Fig. 11: Droplet Spray Generated by Bursting Bubbles [23]

(a). Series of events in the bursting of a bubble through a liquid surface

(b)  $N_2$  bubble from a mercury droplet

(c)  $CO$  bubble from an Fe-C droplet

As mentioned, Morris et al<sup>22</sup> observed that fuming of Fe-C melts was associated with the generation of a fine metal spray that was caused by CO bubbles bursting through the melt surface. They also noted that the decrease in fume rate with decreasing carbon content was related to the mechanism of decarburization and its influence on the size of the metal spray produced.

At high carbon levels, they observed that decarburization occurred mainly at the bath surface and in the area of jet contact. The CO bubbles produced were very small and generated a fine spray as they broke through the melt surface. The size of this metal spray was found to be less than 75  $\mu\text{m}$  in diameter. Since the spray is localized in the jet contact area, it is quickly oxidized to fume.

At lower carbon levels, the CO bubbles are generated within the bulk of the melt. Due to their longer residence time in the bath, they grow to a larger size than those generated in the high carbon melts. The resulting metal spray is also larger in size and Morris measured it to be in excess of 250  $\mu\text{m}$ . Due to the smaller surface to weight ratio of these droplets, they have a smaller chance of being oxidized to fume before they fall back into the bath or are blown out of the system.



An understanding of the mechanism by which these ejected droplets are oxidized to fume can be obtained from studies of the decarburization of Fe-C droplets, either levitated or free falling in oxidizing atmospheres<sup>40-44</sup>.

High speed film of the decarburization of free falling Fe-C droplets in oxygen, taken by Roddis<sup>43</sup>, are shown in Figure 12. Figure 12a shows a drop of high carbon content (4.4%) iron from which CO is being produced on the surface and is burning to CO<sub>2</sub> at the rear of the drop. Figure 12b shows the reaction which occurs at lower carbon levels (1.18% C in this case). The sample is boiling, CO is being generated within the droplet resulting in ejection of smaller particles which oxidize to fume. Figure 12c shows the transition from surface to internal CO formation. The carbon boil (bulk section) becomes more violent as the carbon content decreases until eventually the droplet explodes into many fine particles as seen in Figure 12d. At this point, fume formation is observed to be at its maximum.

Fume formation should be highest when the droplets ejected from the bath are smallest since a small-sized particle has a higher probability of decarburizing explosively because of its higher surface area to volume

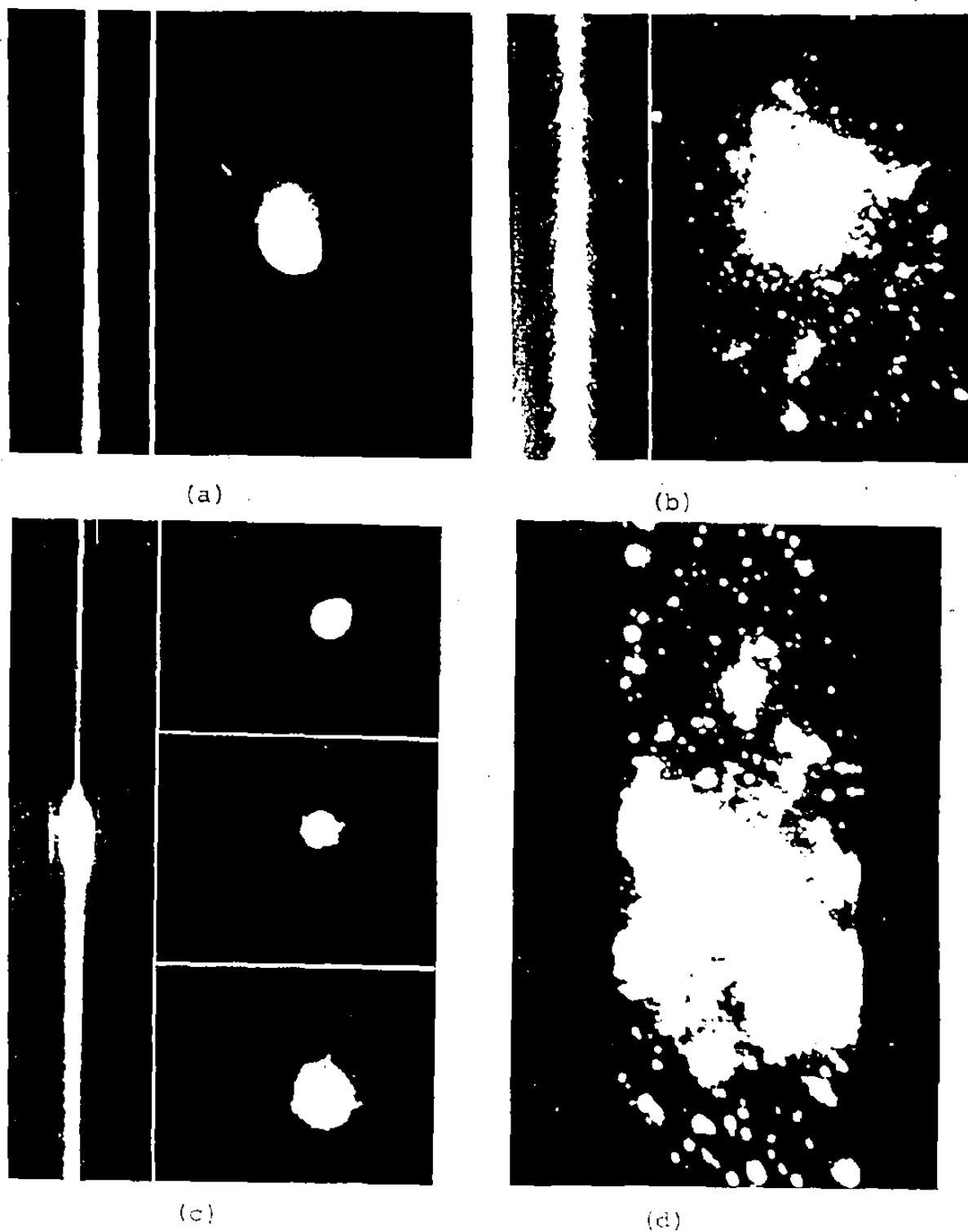


Fig. 12: Still and Streak Photographs Of Fe-C Droplets  
 Falling in  $O_2$  Atmosphere [43]

- (a) Surface reaction, 4.4% C
- (b) Bulk reaction, 1.2% C
- (c) Transition, 3.5% C
- (d) Explosive reaction, 0.4% C

ratio. This is in agreement with the previously discussed results of Morris et al<sup>22</sup>.

It can be seen in Figure 11 and Figure 12 that the spray formed by bubbles bursting through liquid surfaces or from the explosion of metal droplets are spherical in shape. If fume is the result of the oxidation of these particles, then it would be expected that the fume particles would also be spherical in shape.

Fume particles recovered during the decarburization of Fe-C melts were observed microscopically by Morris et al<sup>22</sup> and Ellis and Glover<sup>25</sup>. In both cases, the particles were spherical in shape and ranged in size from .05 to 5  $\mu\text{m}$  in diameter. A typical micrograph is shown in Figure 13.

If fuming is primarily a consequence of ejections being thrown out of the bath, then the concentration of an alloying element in the fume should be equivalent to that in the bath even in the case of a highly volatile element like manganese. After decarburizing Fe-C-Mn melts with oxygen, Ellis and Glover<sup>25</sup> measured the Mn/Fe ratio in the fume and bath and found:

$$\frac{\text{Mn}}{\text{Fe}} \text{ fume} = 0.81 \frac{\text{Mn}}{\text{Fe}} \text{ bath}$$

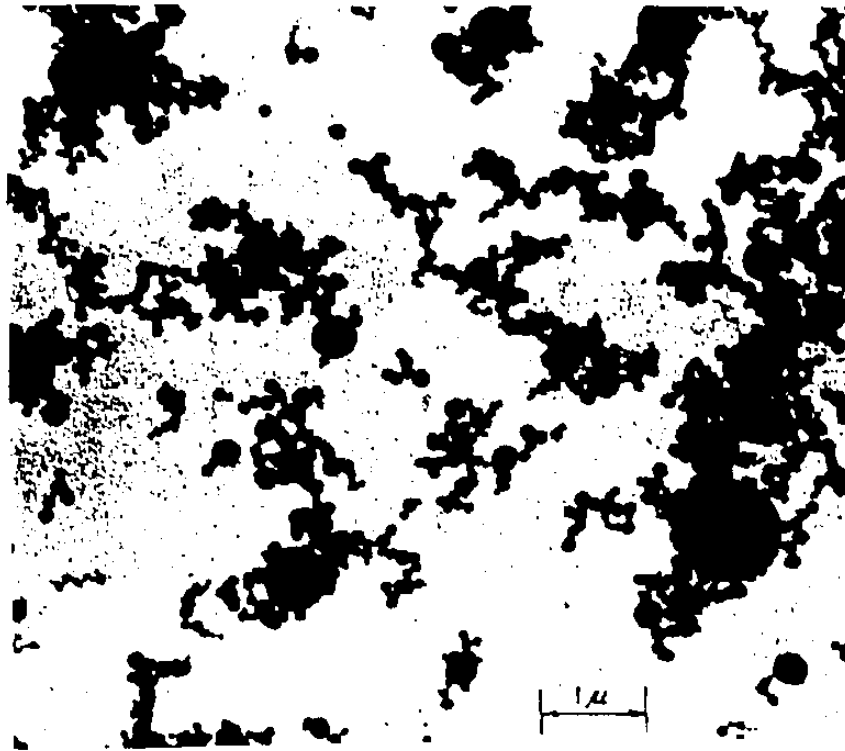


Fig. 13: Electron Microscope Photograph Of  
Fume Produced During Carbon Boil [25]

which is in good agreement with a coefficient close to one as expected for oxidation of ejected droplets.

The implication is very strong that fuming is caused by the oxidation of fine spray that is ejected into the oxygen stream by the bursting of CO bubbles through the melt surface. The carbon content of the bath affects the fume rate by controlling the size of the spray generated in the oxidizing zone of the jet.

### 2.3.3 Oxidation of Metal Spray from the Impact of the Oxygen Jet

In a B.O.F. metal splash can also be produced by the mechanical force of the oxygen jet. From model studies<sup>53,54</sup> using aqueous media and non-assimilating gases, three modes of jet impingement have been characterized (as in Figure 14).

- a) dimpling with a slight surface depression
- b) splashing with a shallow depression
- c) penetration with an apparent reduction of outwardly directed splash

In B.O.F. operations where O<sub>2</sub> velocities leaving the lance tip are Mach 2 and the lance to bath distance is 1 to 4 m, only modes b) and c) above are encountered; both tend to form metal droplets.

Li<sup>55</sup> studied the quantity and size of droplets produced when blowing air through a lance onto a water bath that was fluidized by bubbling air into it from the bottom. These conditions are similar to those which exist in a B.O.F. during refining.

A piece of filter paper was exposed for a fixed time period to the splashing water. The water was coloured with ink so that the splash pattern could be examined visually. With increasing lance flow rates, it was observed that both the quantity and size of splash increases. The splash patterns are shown in

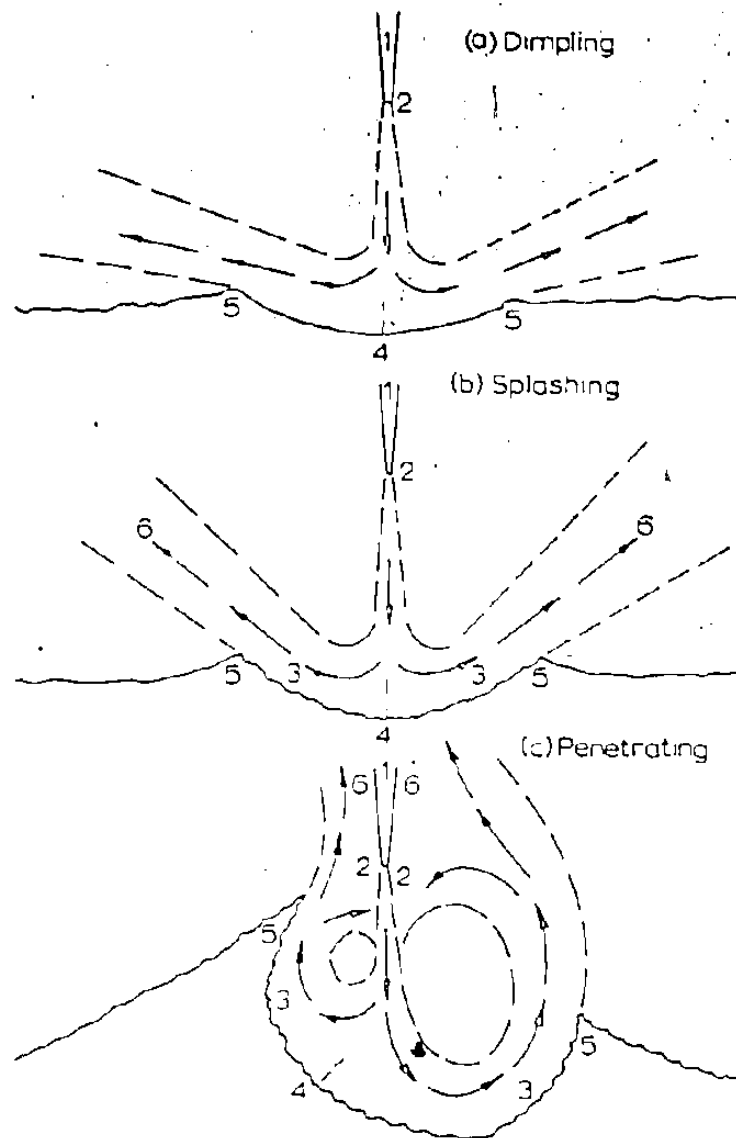


Fig. 14: Comparative geometry of the flow modes. Legend: (1) nozzle body; (2) entrainment region of the original jet; (3) entrainment region of the wall jet across the phase interface; (4) stagnation point of the original jet; (5) separation point of the wall jet; (6) two-phase exit flow. [54]

Figure 15. It was also observed that for a fixed lance flow rate if a froth was present on the surface of the bath (simulating slag cover in the B.O.F.), that the quantity of droplets was reduced (Figure 16).

Li also studied the influence of bath motion on droplet generation by regulating the flow of air through the bottom of the bath. At a fixed lance flow rate, the quantity of droplets formed decreases rapidly with increasing bath flow rate as seen in the splash patterns in Figure 17.

The nature of the jet impingement zone has also been studied<sup>56,63</sup> in hot models of the B.O.F. by using transparent quartz windows. Under slag-free conditions, Okhotskii et al<sup>62</sup> observed that at low oxygen flow rates, the jet forms an open crater (like that in Figure 14 (a)) and that droplets with a diameter of .5-1 mm break away from the ridge of the crater. At higher flow rates, isolated metal expulsion develops at the crater edge. This expulsion is initially directed away from the lance but above some particular blast intensity, it is drawn into the zone of the oxygen stream. This entrapped metal is broken up into a flow of droplets with dimensions of .5-1 mm. The colour of these droplets is much brighter than the initial expulsion indicating intensive interaction with oxygen, as shown in Figure 18.



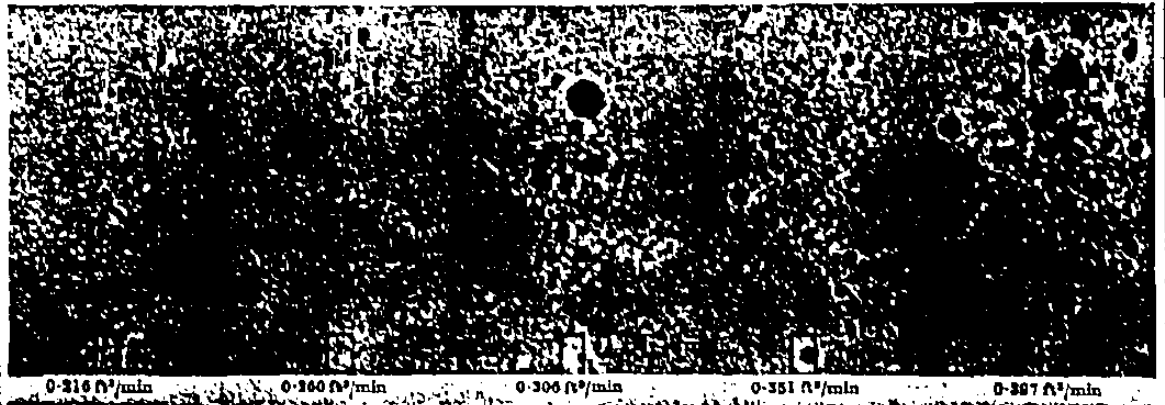


Fig. 15: Splash Patterns At Increasing Jet Flow Rate [55]

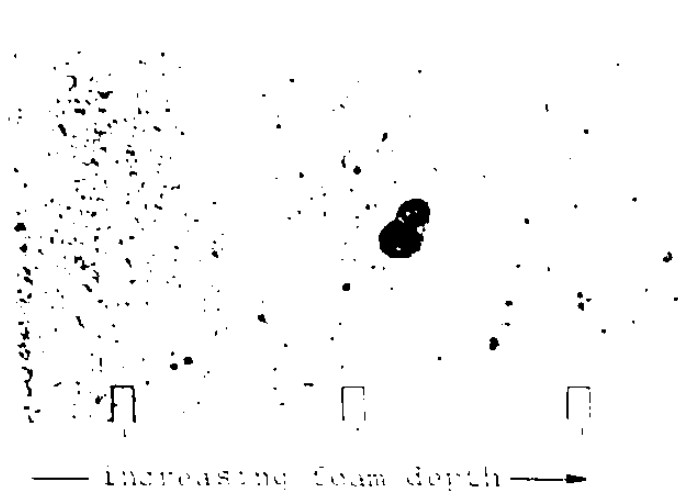


Fig. 16: Splash Patterns With Different Foam Depths [55]

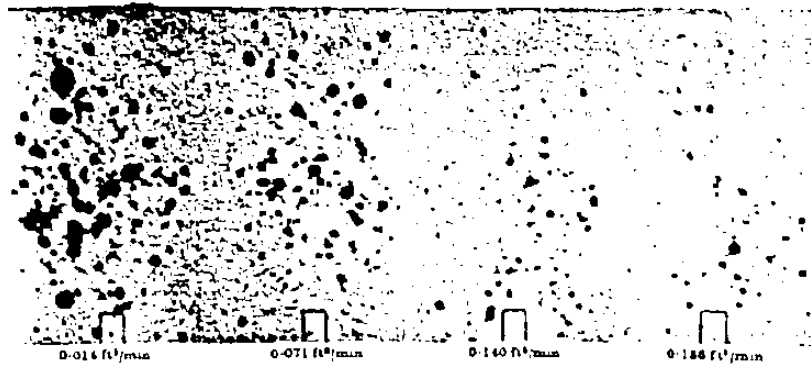


Fig 17: Splash Patterns At Increasing Bath Flow Rate [55]

Molloy<sup>54</sup> also observed that in the penetrating mode the efflux from the crater edge was entrained in the region of the jet where it reacted with the oxidizing gas.

Peregudov et al<sup>45</sup> studied the effect of lance height (at a fixed blowing rate) on the quantity of fume evolved when blowing pure oxygen through a single hole lance onto an Fe - 3.5% C melt. The melt was contained in a graphite crucible and maintained at 1550°C. The amount of fume evolved as a function of lance position is shown in Figure 19. Raising the lance produces a sharp increase in the fume evolution rate which then decreases with a further increase in lance height.

The authors concluded that with a low lance position the O<sub>2</sub> stream penetrates the metal causing it to sputter coarse droplets (.5 to 5 mm) which do not completely oxidize before falling back into the bath. The proportion of fine droplets (< .5 mm) increases as the level is lifted higher above the bath. Due to their smaller mass, these droplets will have a longer contact time in the oxidizing atmosphere giving more complete droplet oxidation (or chance of explosive decarburization) and fume formation.

At very high lance heights, the jet will have a much smaller impact force and the quantity of droplets

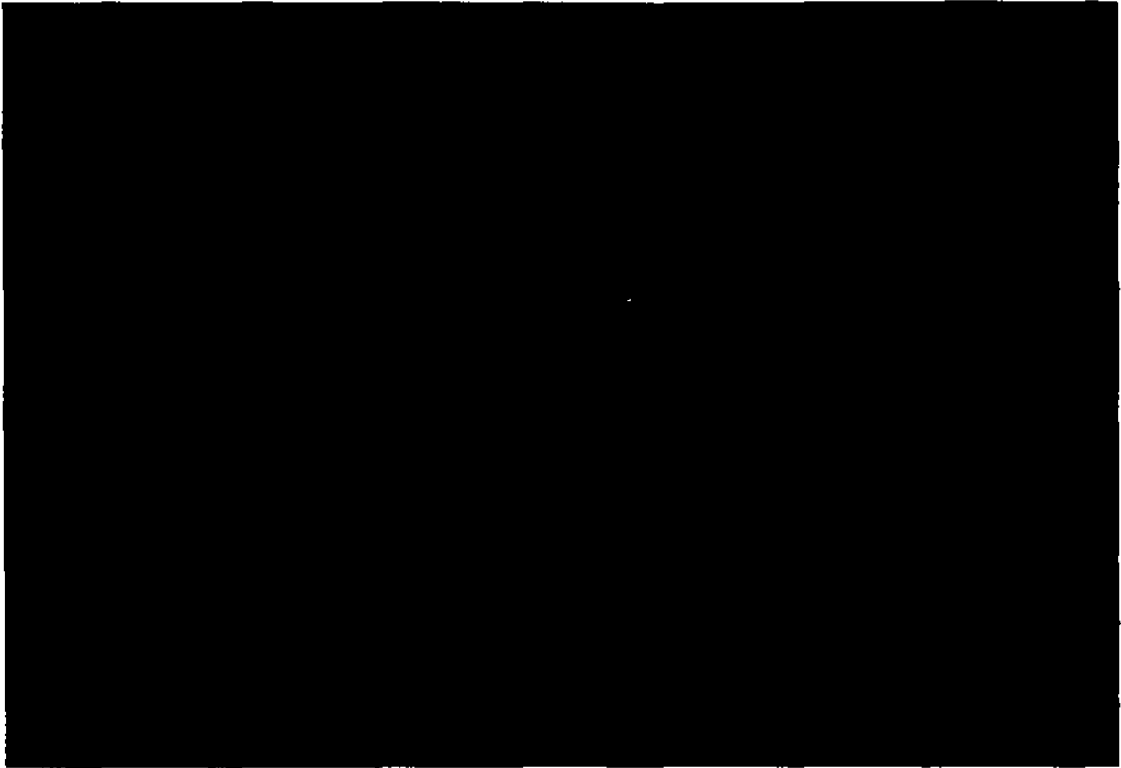


Fig. 18: Metal Ejections Being Oxidized in the Jet Impact Zone of a Small Scale BOF. [90]

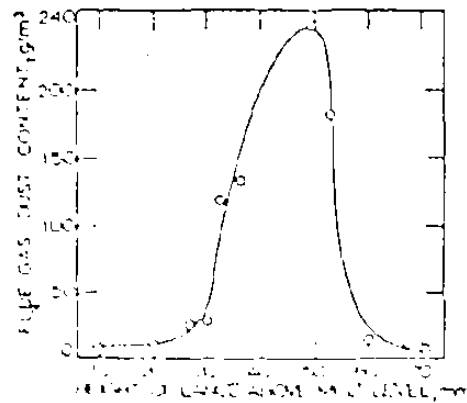


Fig. 19: Effect of lance height above melt level on amount of dust in flue gas. [45]

will decrease. This is basically the same condition that Li<sup>55</sup>, as previously mentioned, observed when at a fixed lance height reducing the flow rate drastically reduced the number of droplets produced.

If surface tension and shear on the cavity wall are neglected, the gas penetration depth into a liquid can be determined by the dynamic pressure associated with the centre line velocity of a free, turbulent, incompressible jet. The centre line velocity decays with distance from the nozzle due to viscous mixing. The centre line velocity at the undisturbed surface level of the liquid can be obtained from:

$$\frac{V_c}{V_j} = K \frac{d_j}{h} \quad (2.1)$$

where K is an empirically determined constant. A value for K of 6.4 has been found to fit a number of different gas-liquid systems including that of oxygen and molten iron.

Equation (2.1) has been developed by Cheslak<sup>87</sup> to yield a relationship between jet momentum and cavity depth as follows:

$$\frac{M}{\gamma_l h^3} = \frac{\Pi}{2K} \frac{a}{h} \left[ 1 + \frac{a}{h} \right]^2 \quad (2.2)$$

$$\text{where } M = \frac{Q V_j \gamma_g}{G} \quad (2.3)$$

A plot of  $a/h$  versus  $M/\gamma_1 h^3$  (the dimensionless jet momentum) for experimental results and equation (2.2) is shown in Figure 20.

Using the lance height and oxygen flow schedule for a typical Dofasco heat, the dimensionless jet momentum was calculated and the jet penetration determined using Fig. 20. The data and results are listed in Table V. The jet penetration increases rapidly during the first three minutes of the blow, after which it remains relatively stable at about .97 m. This would indicate that the maximum amount of outwardly directed spray (splashing mode) would occur only during the first one or two minutes of the blow.

The results of these model studies indicate that the action of the oxygen jet can play a significant role in producing metal spray that can be oxidized to fume.

Since fume produced from the oxidation of metal spray caused by the lance is a result of mechanical force, it would be expected to have a spherical shape. The fume formed from the explosive decarburization of levitated droplets has been observed to resemble that formed by the bursting of CO bubbles<sup>41-44</sup>; the particles are spherical in shape and range in size from 0.05 to 2.0  $\mu\text{m}$  in diameter.

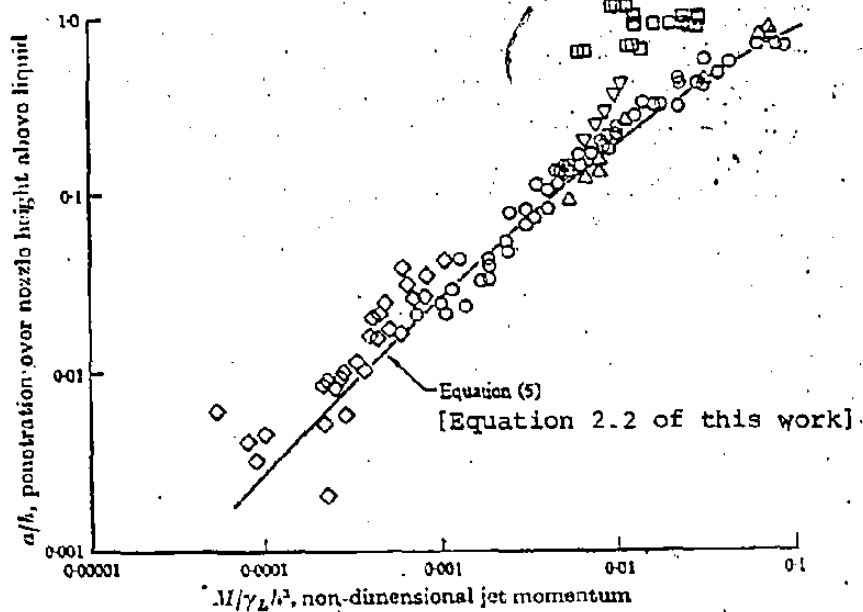


Fig. 20: Plot of  $a/h$  versus  $M/\gamma_L h^3$  (experimental) and equation (5).  $\diamond$ , Banks & Chandrasekhara (1963);  $\nabla$ , mercury;  $\circ$ , cement;  $\Delta$ , water;  $\square$ , molten iron (oxygen jet). [87]

TABLE V

CALCULATED JET PENETRATION FOR DOFASCO BLOWING PRACTICE

Blowing (min.)	O <sub>2</sub> Flow Rate (m <sup>3</sup> hr <sup>-1</sup> )	Lance Height (m)	Dimensionless Jet Momentum* $\frac{M}{\gamma_L h^3}$	Jet Penetration** (m)
0	18000	3.0	.010	.38
1	19000	2.7	.015	.70
2	20000	2.4	.023	.84
3	21000	2.1	.038	.91
4	21000	1.8	.061	.94
5	21000	1.5	.105	.95
6	21000	1.2	.205	.97
7 to end	21000	1.2	.205	.97

\* oxygen density = 1.43 kg m<sup>-3</sup>  
 metal density = 7000 kg m<sup>-3</sup>  
 nozzle diameter = .05 m

\*\* From Fig. 20

#### 2.3.4 Influence of Bath Velocity

Yakovley and Filippov<sup>64</sup> have studied the evolution of fume as a function of bath temperature from a lab scale simulation of an industrial B.O.F. Tests were performed at various levels of superheat in excess of the melts liquidus temperature and the bath carbon content was maintained relatively constant to prevent the effect of carbon level from masking the temperature effect. The results of their work are shown in Fig. 21.

For a fixed bath carbon content, the fume rate increases with decreasing superheat (lower bath temperature). It can also be seen that this relationship holds true regardless of the bath carbon content, although the fume rate increases as the carbon content increases at a fixed superheat level. It is not the decrease in bath temperature in itself that causes the increase in fuming, but rather the influence that this decrease has on the bath viscosity and hence the bath velocity.

As a result of the mechanical force of the jet and the action of rising CO bubbles, the metal bath begins to move. Several authors<sup>65-68</sup> have noted that lower bath temperatures (higher bath viscosity) result in slower bath circulation. This velocity can be related to the fume rate through the previously mentioned results of Li<sup>55</sup> who observed an increase in the amount of jet

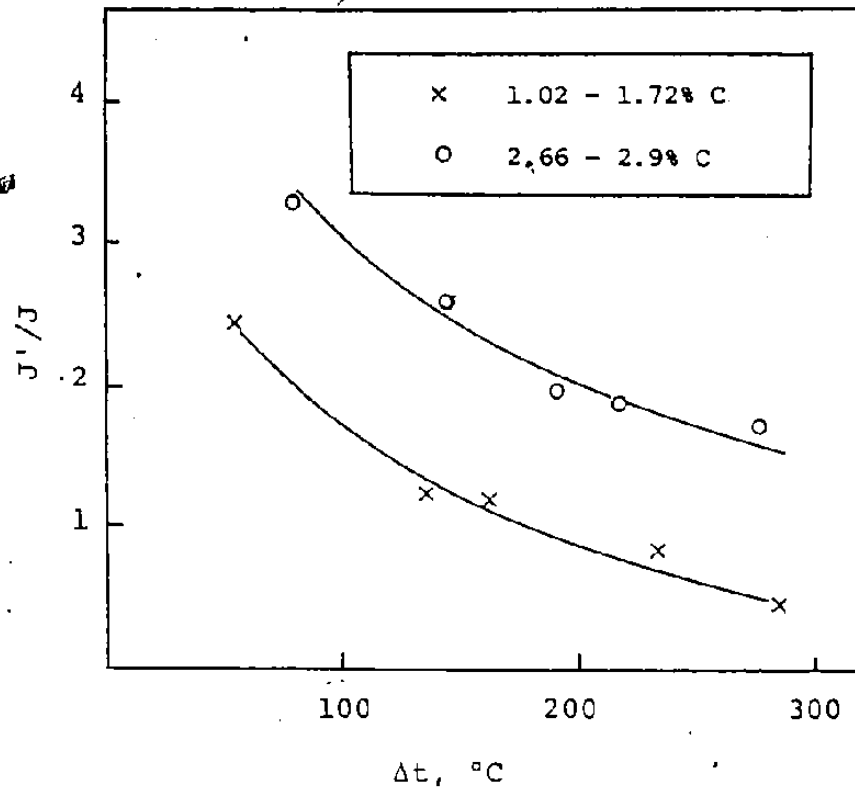


Fig. 21: Photometer signal drop during fume formation ( $J'/J$ ) as a function of metal superheat above liquidus temperature ( $\Delta t = t - t_{\text{liq}}$ ) [64]



produced spray with decreasing bath velocity (Fig. 17). Thus, for any given carbon content, lower bath temperatures will indirectly result in greater metal ejection and a higher fume rate.

Lower bath temperatures will also result in lower slag temperatures and, therefore, higher slag viscosities. This would also lead to increased fume rates since it would hinder the formation of a stable foamy slag cover that would entrap a part of the metal spray being generated in the jet impact zone.

## 2.4 Fume from Industrial B.O.F.s

### 2.4.1 Quantity, Size, Shape and Chemical Analysis

The results of laboratory experiments have shown that fuming could be caused by either:

- i) direct vaporization of iron
- ii) the oxidation of metal droplets ejected above the bath either by the action of CO bubbles or by the mechanical force of the jet.

It was also seen that the size and shape of the fume particles are dependent on the process by which they were formed. The fume particles that result from vaporization are either hexagonal or octagonal in shape (depending on their degree of oxidation) and exist over a limited size range of 0.05 to 0.2  $\mu\text{m}$  in diameter. Fume resulting from vaporization also has a higher concentration of volatile elements (approximately 60-150 times as much Mn) than the bulk bath from which it originated.

The fume particles resulting from oxidation of ejected metal droplets are spherical in shape and exist over a larger size range from .05 to 5  $\mu\text{m}$  in diameter. Since they are formed by mechanical forces, the ratio of volatile elements (Mn) to iron in the fume is approximately equal to that in the bath. Therefore, it should be possible to identify the mechanism by which fume is

formed in an industrial B.O.F. from observations of its size, shape and chemical analysis.

The major constituent of B.O.F. fume is iron. Analysis of fume from B.O.F. operations<sup>1-3,69,70</sup> show that the total iron content ranges from 50 to 60%. Another major constituent is CaO, which has its origin in flux additions, as very fine particles can be carried away by the exhaust gases as they leave the furnace. The CaO content varies from 5-15% and peaks during periods of flux additions. Table VI shows the evolution of fume chemistry during a B.O.F. heat as measured by Krichevtsov<sup>2</sup>, (note that the off-gases were completely combusted). The dust content of the furnace exhaust gases ranges from 40-90 g/m<sup>3</sup> and the amounts of iron lost ranges from .8 to 2% of the total furnace charge weight<sup>1-4</sup>.

The amount of fume evolved during the process of a heat is not constant. It is greatest during the earliest parts of the blow and tapers off towards the end. Figure 22 is a graph of the fume weight vs. blowing time as measured by Krichevtsov<sup>2</sup>. In this particular case, the iron losses increase at the 10-16 minute mark of the blow due to the addition of iron ore. The increase in fume is associated with the entrainment of fine ore particles in the off-gases. If ore was not added during this period of the blow, the fume evolution rate would follow the broken line shown in Figure 22.

TABLE VI

CHEMICAL COMPOSITION OF DUST IN CONVERTER GASES (%)  
 AFTER GASES HAVE BEEN COMPLETELY COMBUSTED (AT TOP  
 OF GAS UPTAKE); ADDITIONS OF LIME (t) ARE SHOWN IN  
 BRACKETS [3]

t, (min.)	Fe <sub>tot</sub>	FeO	Fe <sub>2</sub> O <sub>3</sub>	SiO <sub>2</sub>	CaO	MgO	MnO
1(3)	43.88	8.25	53.62	4.33	26.99	0.45	1.66
2	42.85	6.63	53.55	3.16	31.52	0.00	1.42
3	50.69	11.16	60.15	3.14	21.09	1.26	1.25
4	56.76	10.47	69.60	2.78	12.56	1.02	1.44
5	61.46	7.89	79.20	2.21	6.38	0.92	1.87
6(3)	38.89	3.91	51.33	2.25	35.72	0.04	1.34
7	48.69	6.63	62.31	2.35	19.64	1.15	2.09
8	59.00	6.85	76.83	2.44	9.53	0.44	2.72
9	59.86	5.67	81.01	2.24	7.34	0.26	2.97
10	62.78	5.67	83.63	2.21	4.59	0.17	3.02
11	58.65	7.44	75.51	1.61	9.89	0.30	2.82
12(0.5)	44.45	14.59	56.66	1.58	33.03	0.30	1.53
13	56.90	11.40	71.56	1.62	9.69	0.16	2.34
14	59.98	10.94	73.62	1.75	7.76	0.30	2.62
15	61.90	12.32	74.81	1.58	5.70	0.00	2.55
16	64.53	15.10	75.30	1.17	3.57	0.00	2.55
17	62.85	10.86	77.81	0.88	2.82	0.00	4.32
18	63.03	13.71	74.90	0.81	4.47	0.34	3.22
19(0.5)	41.20	7.16	47.66	1.44	30.00	0.43	2.27
20	55.55	5.70	73.10	1.52	10.92	0.56	3.30
21(0.5)	51.06	6.32	66.00	1.89	15.53	1.19	2.76
Average	55.10	8.50	69.00	2.07	14.70	.40	2.40

A typical electron micrograph of fume particles recovered from an industrial B.O.F. by Bogdandy<sup>71</sup> is shown in Figure 23. The particles are an agglomeration of very small spheres. The size of industrial fume has been measured by several investigators<sup>3,14,70-72</sup> and ranges from .03 to 10  $\mu\text{m}$  in diameter, the majority (70 to 90%) being less than 1  $\mu\text{m}$ . Approximately 20% of the weight of iron in the fume is made up of particles less than 0.1  $\mu\text{m}$  in diameter<sup>72</sup>.

From Krichevstov's results in Table VI, the average ratio of Mn/Fe in the fume is approximately 0.03. In a B.O.F. the majority of the manganese is oxidized during the first few minutes of the blow, after which the bath manganese remains relatively constant at 0.15 to 0.3%<sup>24,73,74</sup> depending on initial hot metal manganese levels. Assuming the average bath manganese to be 0.2% and the average bath iron to be 98%, the Mn/Fe ratio in the bath becomes 0.002. This gives a Mn/Fe ratio in the fume 15 times higher than that in the bath.

The observed shape and size range of the industrial fume particles suggests they originate from the oxidation of ejected metal droplets. However, the Mn/Fe ratio in the fume is 15 times larger than the value of one expected for fume produced by this mechanism, indicating that direct vaporization is also a contributing factor in fume formation.

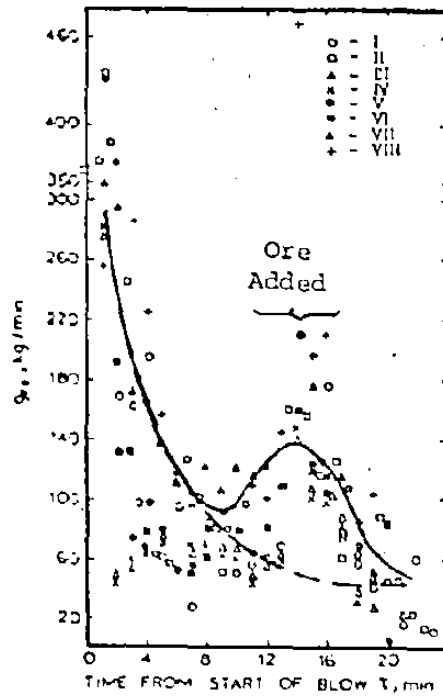


Fig. 22: Variation in losses of iron with furnace dust  $g_{Fe}$  during progress of blow in heats I-VIII [3]

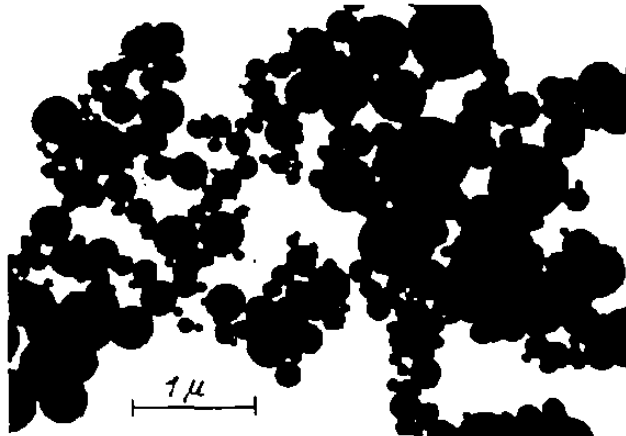



Fig. 23: Electron Micrograph of B.O.F. Fume [71]

#### 2.4.2 Influence of Bath Carbon and Slag Volume

The evolution of fume from industrial B.O.F.s has also been related to the carbon content of the bath<sup>1,2,64,75</sup> as shown in Figure 24. The quantity of fume decreases with decreasing bath carbon content, and the fuming rate is approximately constant when the bath carbon is less than 2%.

Several authors<sup>75-79</sup> have noted that the quantity of fume evolved during refining is influenced by the volume of slag present. The fume rate decreases with increasing slag volume independent of bath carbon content. Typical variations in slag height and weight as a function of blowing time are shown in Figure 25 and Figure 26. Slag weights are usually calculated using a mass balance for silicon (using slag and bath analysis) while slag height is measured using acoustic techniques<sup>79,80</sup>.

Okhotskii and Gorbic<sup>75</sup> studied the relationship between fume rate, bath carbon and slag condition using a 130 ton industrial B.O.F. Measurements were made during the three typical refining periods that exist during B.O.F. refining; these are:

- I. The rapid oxidation of silicon and manganese with low decarburization rates (< .1%/min.) and little slag cover.
- 

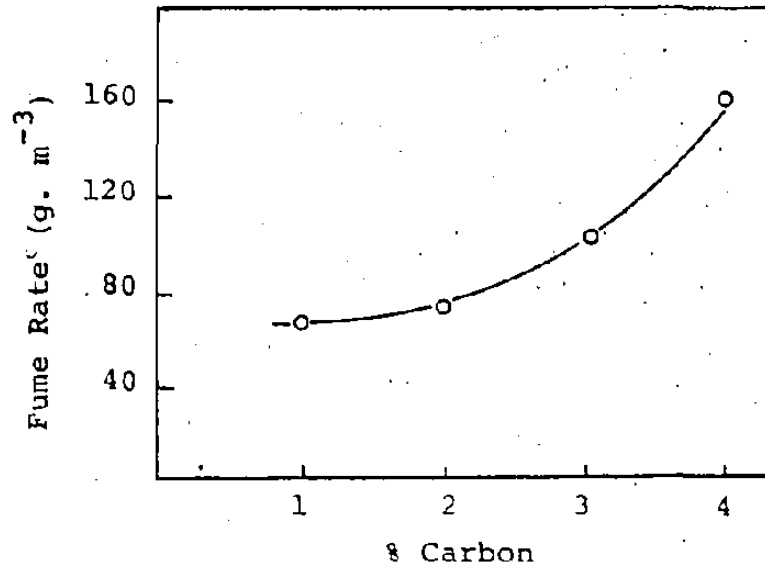


Fig. 24: B.O.F. Fume Rate Vs. Bath Carbon [75]

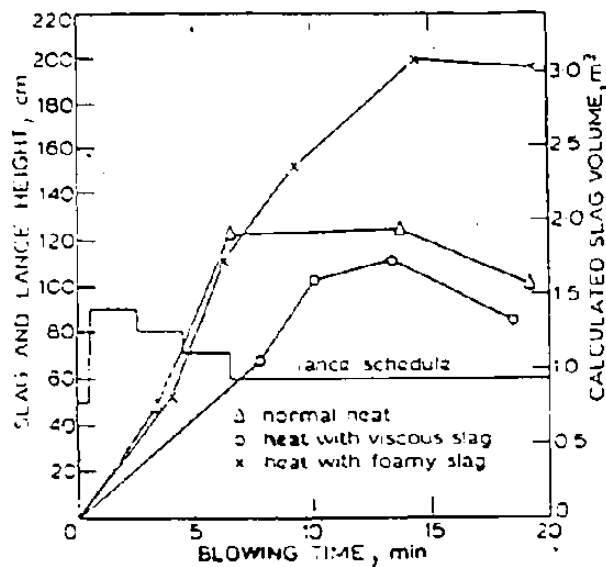


Fig. 25: Typical variations in slag height and slag volume during a blow [81]



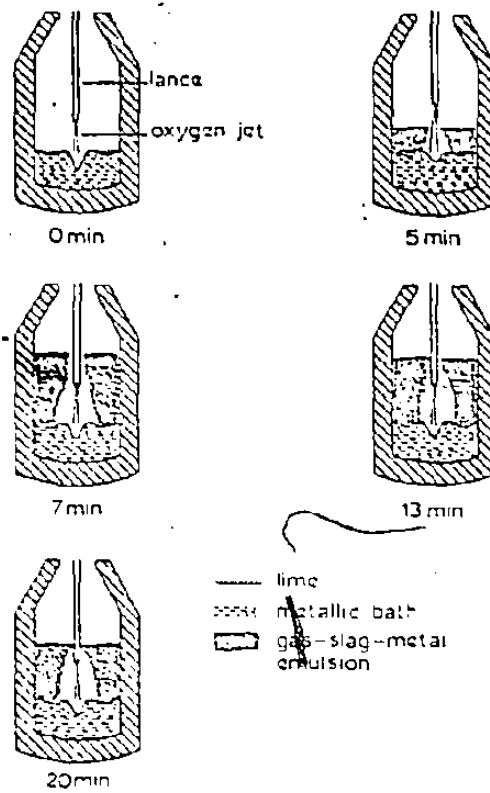


Fig. 26: Sections through a LD converter at various stages of the blow [81]

Pool Copy

- II. The rapid combustion of carbon ( $.1-.3\% \cdot \text{min.}^{-1}$ ) in the presence of a layer of foaming slag.
- III. The rapid combustion of carbon with a coagulated slag.

The results of Okhotskii and Gorbic are shown in Figure 27. In those periods of the heat characterized by a slag cover (Period I & II), the fume rate is roughly constant for the same carbon content. During the process of rapid decarburization, the slag is deoxidized and the concentration of iron-oxides in the slag decreases. This lowers its melting point and the slag loses its capacity to foam, thickens and decreases in volume (Period III). During Period III the fume rate exceeds that of periods I and II for a given carbon content. It was also noted that an increase in the level of a foaming slag from 1.5 to 2.5 m reduced the quantity of fume produced by approximately 50%. The results illustrate the effect that the slag layer can have on the rate of fume formation and how the slag can mask the relation between fume rate and bath carbon level.

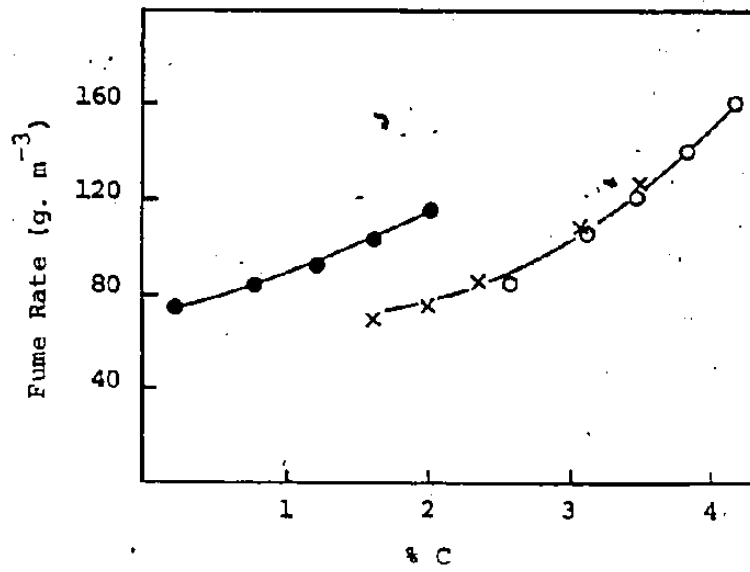
The authors also measured the effect of metal ejection on fume rate. In Figure 23, the effect of slag height (Periods I and II) and height the metal splash reaches above the level of the bath (Period III) on the rate of fume formation are shown. As the slag height

increases, the quantity of fume decreases; however, after a certain limit any further increase in slag height does not influence the fuming rate.

Taking into account that the height of the metal splash is governed by the intensity of splash formation, the results in Figure 28 show the strong influence of the oxidation of metal splash on the fuming rate.

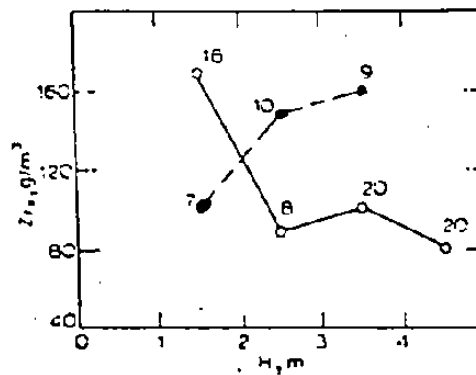
From these results, the authors concluded that fume formation is governed mainly by the process of metal evaporation in the reaction zone when there is an adequately thick slag cover. In the absence of this slag cover, the formation of spray begins to play an important role in the process.

This conclusion is in good agreement with the previously observed size, shape and chemical analysis (Fe/Mn ratio) of the fume material.



○, x Period I & II - Slag Cover  
 ● Period III - "Slagless"

Fig. 27: Relation Between B.O.F. Fume Rate and Bath Carbon Content for Different Slag Conditions [75]



○ periods I and II; ● period III

Fig. 28: Effect of height of layer of slag (—) and of level of metal splashes (---) on dust content of waste gases [75]

### 3. DESIGN AND EVALUATION OF FUME SAMPLING DEVICE

#### 3.1 The Gas Cleaning System

An overall schematic of Dofasco's #1 melt shop off-gas collection system is given in Figure 29. The system normally operates under 4 fan/3 furnace conditions and consists of the following units:

- i) 3 x 160 ton B.O.F.s.
- ii) 3 furnace hoods leading to corresponding spark boxes.
- iii) 3 individual ducts with individual dampers which lead to
- iv) a common cross-duct which is extracted by
- v) 4 individual venturi-scrubber/fan systems.

In the spark box, approximately  $10 \text{ m}^3 \text{ min}^{-1}$  of cooling water quench the off-gases to approximately  $93^\circ\text{C}$  ( $200^\circ\text{F}$ ); the action of these water sprays also removes the coarser particles of metal and slag from the gases.

Since 3 furnaces operate off a 4 fan common extraction system, the off-gas capacity of each furnace hood is dependent on the number of dampers open. The damper can be open, closed or modulating (opening and closing) depending on whether the furnace is operating or not. It will be shown later that the position of these dampers influence the pressure (and, therefore, the flow) in the other furnace ducts. If only one

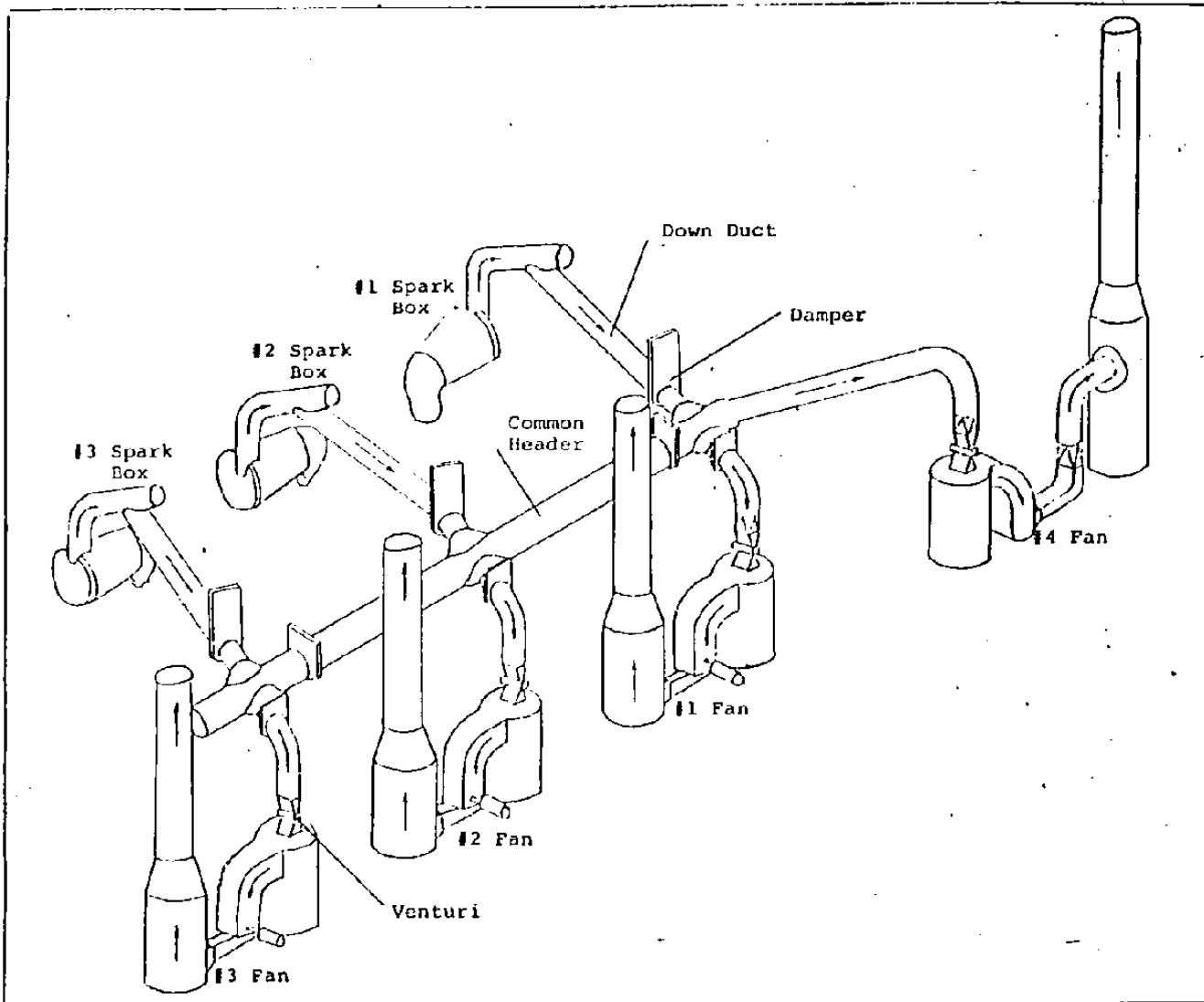


Fig. 29: #1 Melt Shop Dust Collection System

furnace is blowing, then its damper is open, one of the other two is closed and the third is modulating to maintain a constant pressure (approx. 25 cm of water) in the common header. If the third damper did not modulate, the pressure in the header would be too high and venturi efficiency would decrease. When two furnaces are blowing, their two dampers are open and the third is closed; under these conditions, the pressure in the common header is 18 cm of water.

In the venturi scrubbers, the gas and dust particles achieve a velocity of 100-150 m sec<sup>-1</sup> as they pass through a thin water curtain in the rectangular throat of the venturi. The high gas velocity causes the water curtain to be shattered into small droplets that wet the dust particles. The clean gases are exhausted to the atmosphere while the venturi discharge is sent to a thickener.

### 3.2 Sampling Location and Conditions

To determine the quantity of fume evolved from one B.O.F., the measurement must be made before the off-gas enters the common header. A diagram of the gas collection system between the furnace and common header is shown in Figure 30. The section of ductwork having the easiest access is the 2.4 m diameter downduct which is located outside the building. It is recommended<sup>82</sup> that the sampling point be located at least 5 pipe diameters (in this case 12 m) from any bends in the duct. The sampling point chosen was that of an access door located 10.7 m downstream and 6.1 m upstream of bends at the top and bottom of the downduct. The centre of the access door is 45° from the top of the duct.

The downduct has water sprays located at 3 m intervals along its length; also at 45° from the top of the duct. These water sprays further cool the off-gases from approximately 93°C leaving the spark box to 55-70°C at the point where the fume samples will be taken.

To determine the gas velocity in the downduct, Pitot tube measurements were taken as a function of blowing time and distance across the duct.

The flow conditions in the duct were found to be a function of both the distance across the duct and the configuration of the furnace dampers. The effect of



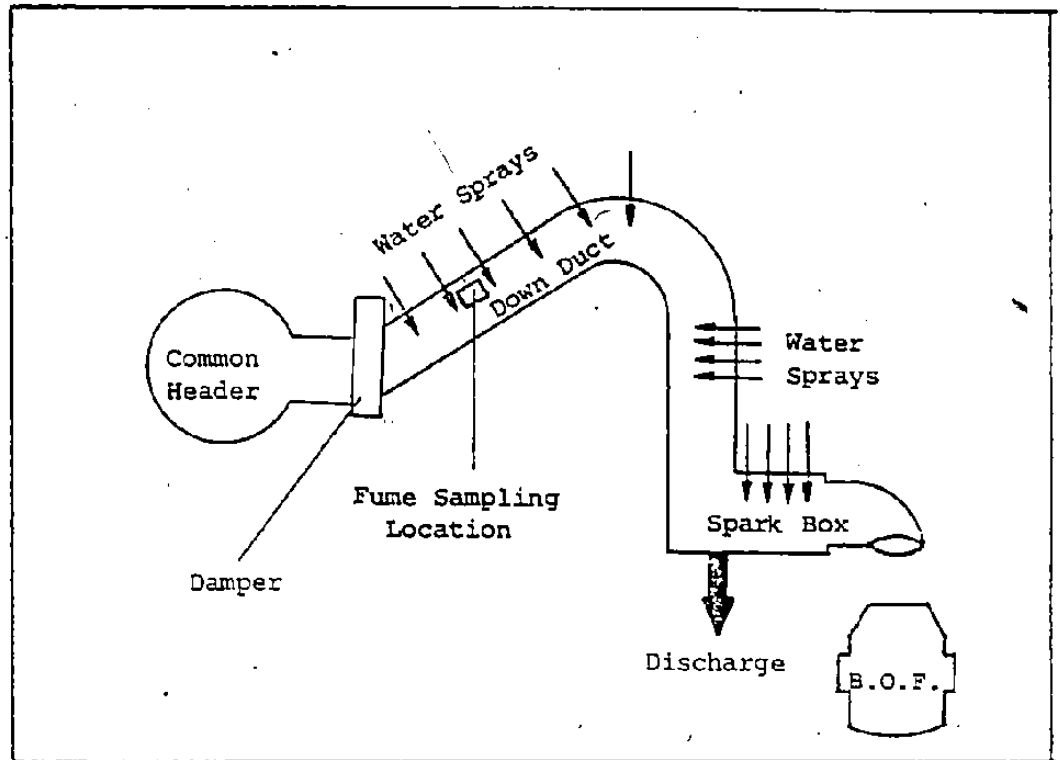


Fig. 30: Location of Fume Sampling

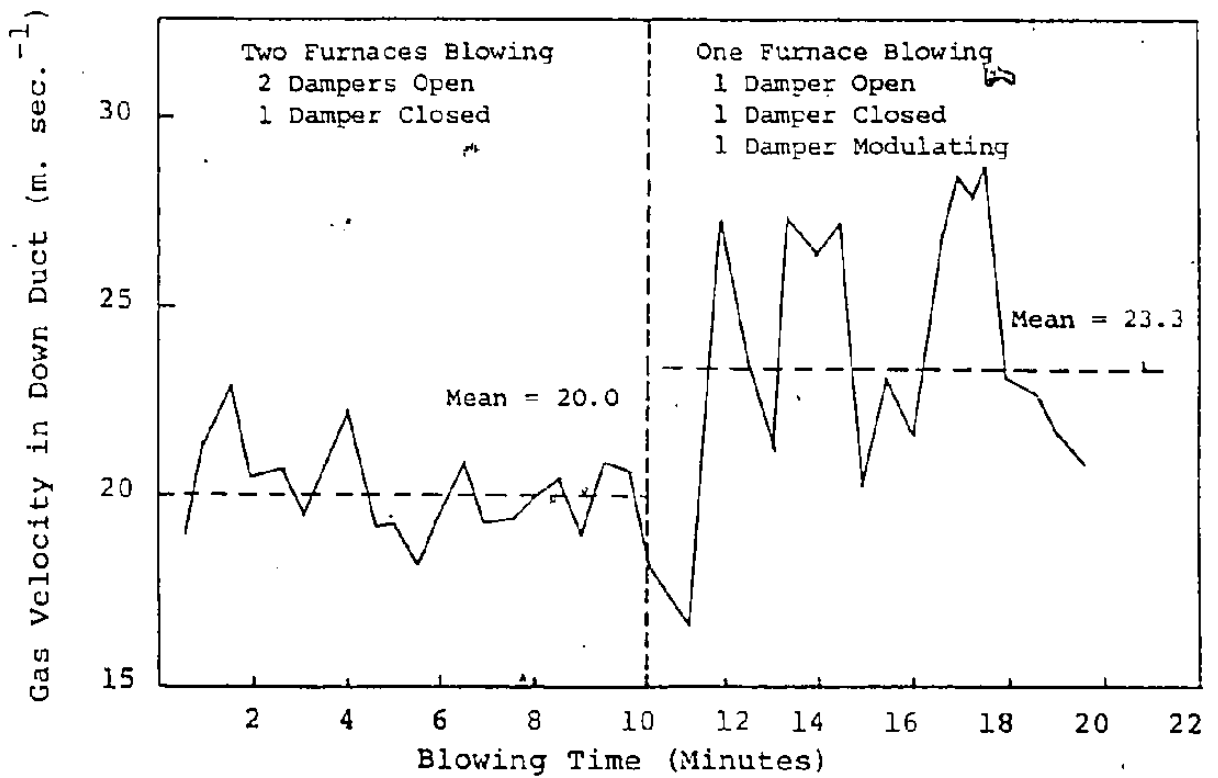


Fig. 31: Effect of Damper Configuration on Gas Velocity in Down Duct

damper configuration on gas velocity in the downduct is seen in Figure 31. These measurements were made during the course of one heat at a distance of 0.3 m from the duct wall with the water sprays on. The flow velocity is not constant because the pressure in the common header fluctuates; however, there is a noted change in the flow when one of the dampers begins to modulate. The flow rate increases due to the increase in crossduct pressure (from 18 to 25 cm of water), and the fluctuations become larger. When two furnaces are blowing (no damper modulation), the average gas velocity in the downduct is  $20 \text{ m sec.}^{-1}$ . When only one furnace is blowing (one damper modulating), the average gas velocity increases to  $23.3 \text{ m sec.}^{-1}$ . Most heats have some period when a damper is modulating.

To determine the velocity profile across the duct, Pitot tube measurements were taken every two minutes at 0.3 m intervals across the duct. This was repeated for five heats (approximately 50 measurements at each point in the duct). The average values at each point are plotted in Figure 32. The axis on which the Pitot tube measurements were made was directly in line with one set of water sprays (the fume samples were taken along the same axis). These water sprays form a resistance to the gas flow and the velocity profile is skewed to the far side of the duct; the average of the velocities across

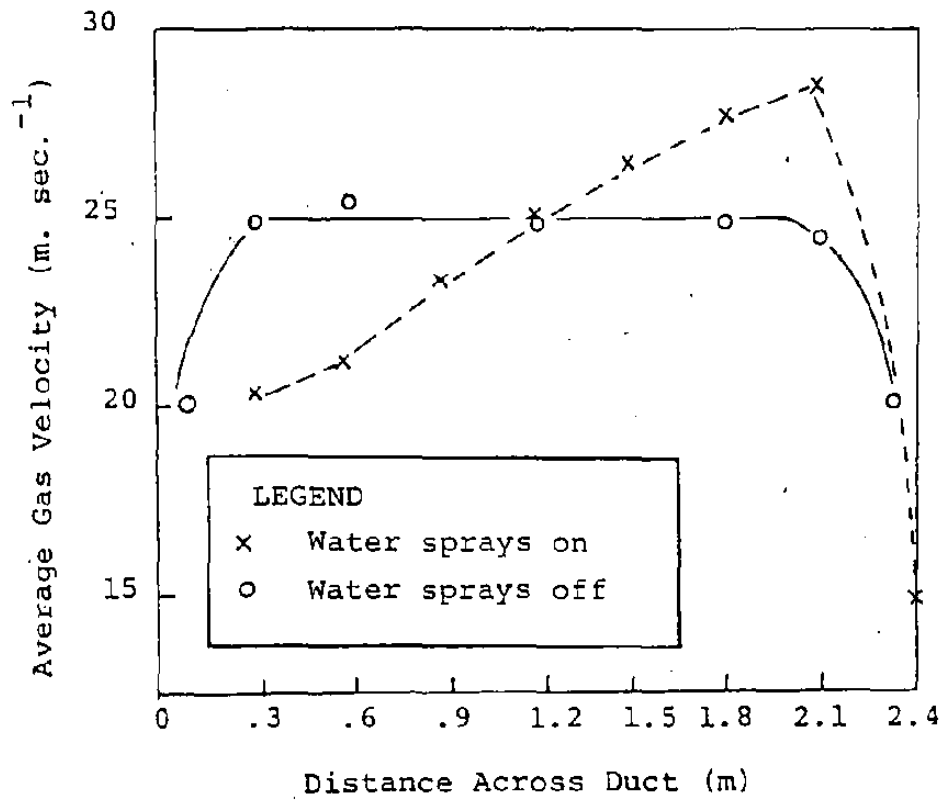
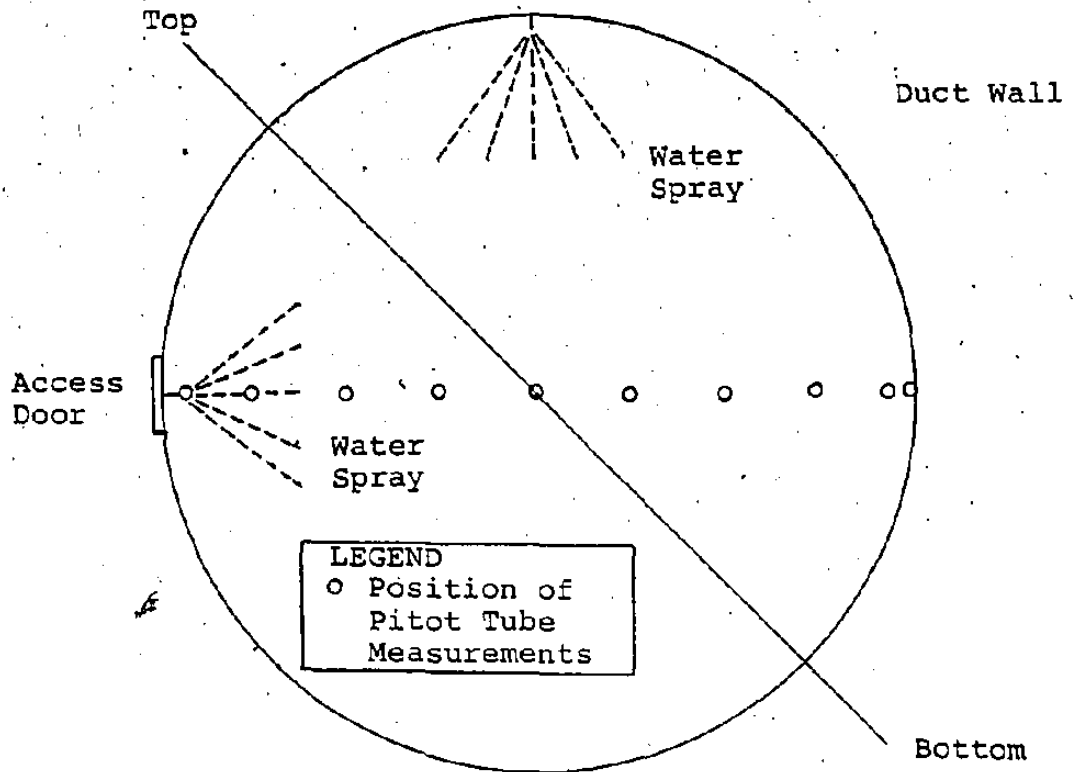


Fig. 32: Results of Pitot Tube Measurements

the duct is equal to that at the 1.2 m mark (duct centre).

Since the profile determined cannot be considered normal, permission was received from the production department to turn off the sprays for seven heats. The flow was measured at one minute intervals at a fixed location across the duct for each heat. The average gas velocities without the water sprays are also shown in Figure 32. Without the water sprays on, the flow is approximately constant across the duct except near the walls; this is the expected profile.

During normal plant operation, these water sprays are on and this is the condition under which the fume samples were collected.

### 3.3 Description of Sampling Device

When a sample of a particle-laden gas is removed from a gas stream without due regard for possible sampling errors, it will very likely be non-representative. Errors may occur because of the use of incorrect sampling location, sampling velocity, bends in the sampling line, settling of particles, heating or cooling of the sample, and improper orientation of the sampling nozzle.

As mentioned before, the sampling location was chosen as far as possible downstream from any bends in the duct and as will be seen, the design of the sampler is such that errors caused by bends in the sampling line, settling of particles, heating and cooling of the gas and improper orientation of the sampler nozzle can be ignored.

Investigators<sup>82-84</sup> have found that, in general, isokinetic sampling is required to obtain a representative sample of material in a gas stream. The need for isokinetic sampling is illustrated in Figure 33. Figure 33(a) depicts isokinetic sampling, and it may be seen that under these conditions, a representative sample will be collected. Figure 33 (B and C) shows the sample being withdrawn at a rate where the velocity through the nozzle is greater or less than in the main stream. The finer particles due to their smaller inertia will tend to follow the gas flow lines. As a result, the

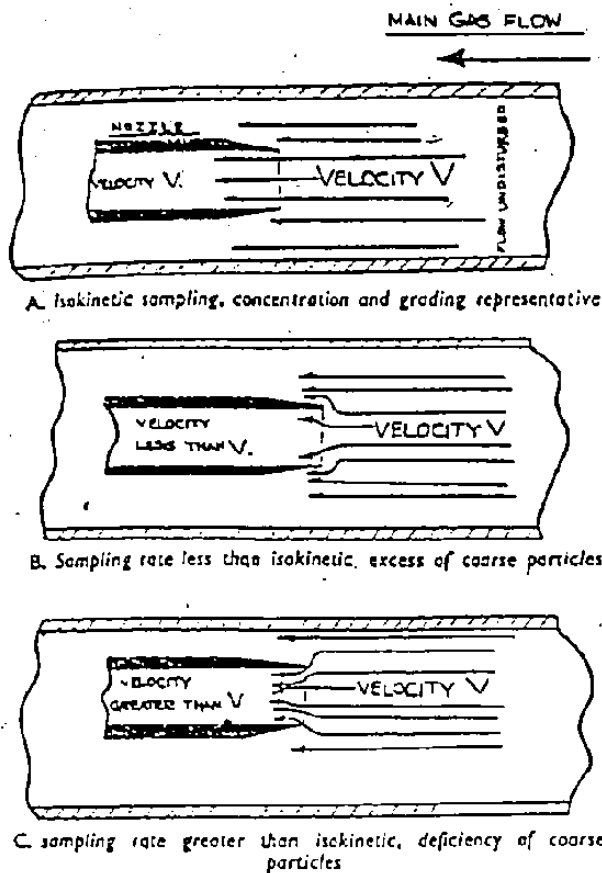


Fig. 33: Effect of error in sampling velocity on accuracy [83]

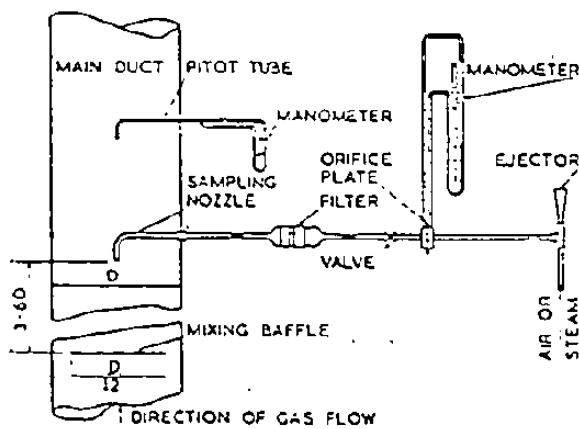


Fig. 34: Arrangement of simple sampling set-up [83]

POOR COPY

sample collected will have either an excess or deficiency of fine particles, and the size distribution of the collected particles will not be representative.

A typical isokinetic sampling system is shown in Fig. 34. In this case, either a compressed air or a steam ejector is used as a source of vacuum. A valve is used to regulate the pressure through the sampling nozzle so that the gas velocity is equal to that in the duct as measured by a Pitot tube.

For true isokinetic sampling, flow conditions in the duct should be laminar; however, it is still felt that even under turbulent flow conditions, isokinetic sampling gives the best results<sup>82</sup>. The average flow velocity in the downduct (from Fig. 32) is approximately 25 m.sec.<sup>-1</sup>; this corresponds to a Reynolds Number in the order of  $10^6$  which indicates turbulent flow.

It has already been shown that the gas velocity in the downduct (Fig. 31) can be highly irregular when one of the furnace dampers is modulating. As a result, it would be very difficult to maintain the same flow rate in the sampler nozzle as exists in the downduct considering sampling times are usually in the order of one minute or less.

The errors which can be introduced by non-isokinetic sampling of dry dust-laden gases as determined by Stair-

mand<sup>82</sup> are shown in Table VII. With coarse particles (greater than 10  $\mu\text{m}$ ), the ratio of observed concentration to true concentration is inversely proportional to the ratio of sampling speed to dust speed.

With the very fine particles (approximately 1  $\mu\text{m}$  in diameter) varying the ratio of sampling speed to dust speed from 0.5 to 1.5, only changed the ratio of observed concentration to true concentration by  $\pm 2\%$ . Thus, when the dust particles being collected are in the range of 1  $\mu\text{m}$ , errors caused by non-isokinetic sampling are not significant. As previously shown in Figure 6, over 90% of the fume particles evolved during B.O.F. steelmaking are less than 1  $\mu\text{m}$  in diameter.

The results shown in Table VII were obtained using dust particles having a density of 1  $\text{g cm}^{-3}$ ; however, similar results were reported by Little<sup>83</sup> using glass beads with a density of 2.8  $\text{g cm}^{-3}$ . The density of iron oxides is approximately 5  $\text{g cm}^{-3}$ .

When gas-born dust particles flow in a duct, the gas velocities are generally large in comparison with the free-falling speeds of the particles. The maximum particle size that can be carried by the gas stream can be calculated by equating the gravitational force to the viscous frictional drag force for a particular particle size. This calculation is shown in detail in Appendix A, the result based on the average gas flow



TABLE VII  
EFFECT OF INCORRECT SAMPLING VELOCITY [83]

Duct speed	30 ft./sec.	30 ft./sec.
Sampling speed	15 "	45 "
Sampling speed, duct speed	1/2 "	1.5 "
Particle diameter (Density 1 gm./c.c.)	Ratio: $\frac{\text{Observed concentration}}{\text{True concentration}}$	
100 microns ( $\mu$ )	1.99	0.67
10 " ( $\mu$ )	1.54	0.82
1 micron ( $\mu$ )	1.013	0.996

rate of  $25 \text{ m. sec.}^{-1}$  (Fig. 32) gives a maximum particle diameter of  $40 \mu\text{m}$ . Therefore, it is expected that particles ranging in size from  $40 \mu\text{m}$  down will be found in the samples collected from the downduct.

A diagram of the fume sampling device used in this study is shown in Fig. 35. The sampler is of a flow-through design. When suspended in the downduct, the gas and fume particles are drawn into it by the action of the flowing gas stream. The sampler has a  $2.5 \text{ cm}$  I.D. nozzle which directs the incoming gases to two inline filter canisters. Each of these canisters is  $5 \text{ cm}$  in diameter and  $5 \text{ cm}$  in length. They are each filled with  $2 \text{ g}$  of Longlife<sup>®</sup> synthetic filter material. The gas stream can also flow around the sides of the filter canister which should ensure that suction exists at the nozzle entrance even as the filter material gets loaded with water and solid particles. The design is such that the gas stream is drawn through it, not blown into it.

It is possible from the design of this device that the gas flow in the nozzle will be less than that of the surrounding gas stream. Although this would represent non-isokinetic sampling conditions, it is not expected to cause any serious error due to the very fine particle size of the fume, the majority being less than  $1 \mu\text{m}$  in diameter.

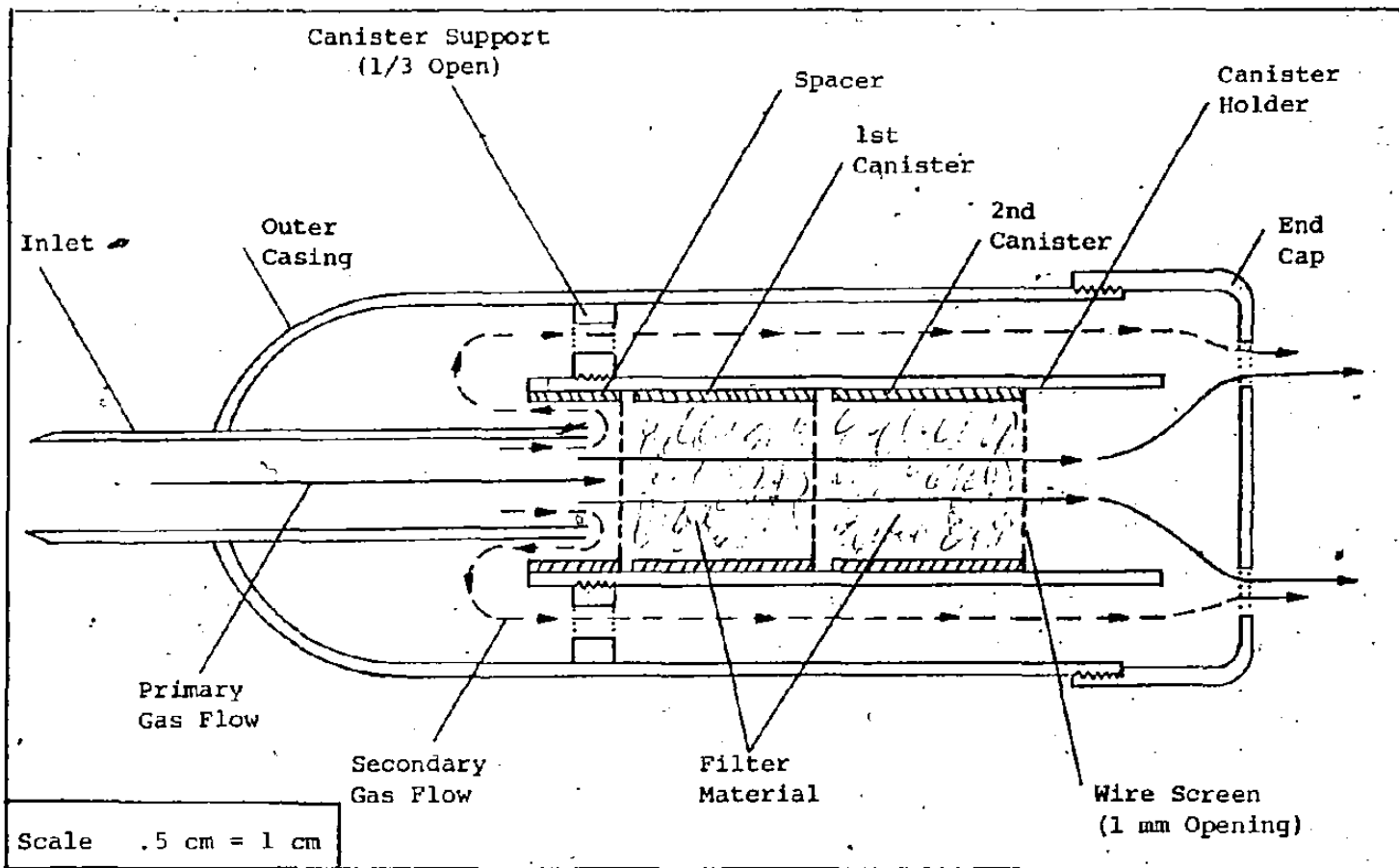


Fig. 35: Diagram of Fume Sampling Device Used in This Investigation

Photographs of the front, side and rear of the sampling device are shown in Figure 36. The canister holder and the two filter canisters are shown removed from the outer shell in Figure 37. The filter canisters are inserted in the canister holder and screwed into the outer casing as seen in Figure 38. This is a view of the exit end of the sampler with the end cap removed.

The sampling device is mounted on the side of the downduct as shown in Figure 39. To take a sample, the access door "A" is slid out of the way and the door "B" is closed over the opening. In this position, the sampler nozzle is facing into the gas stream. The sampler is moved to various positions across the duct by pushing the support rods "C" into the duct.

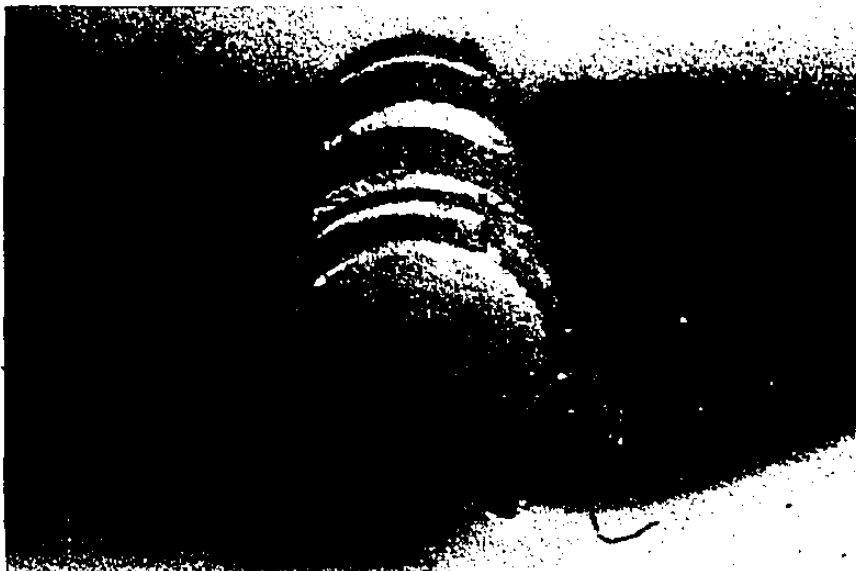
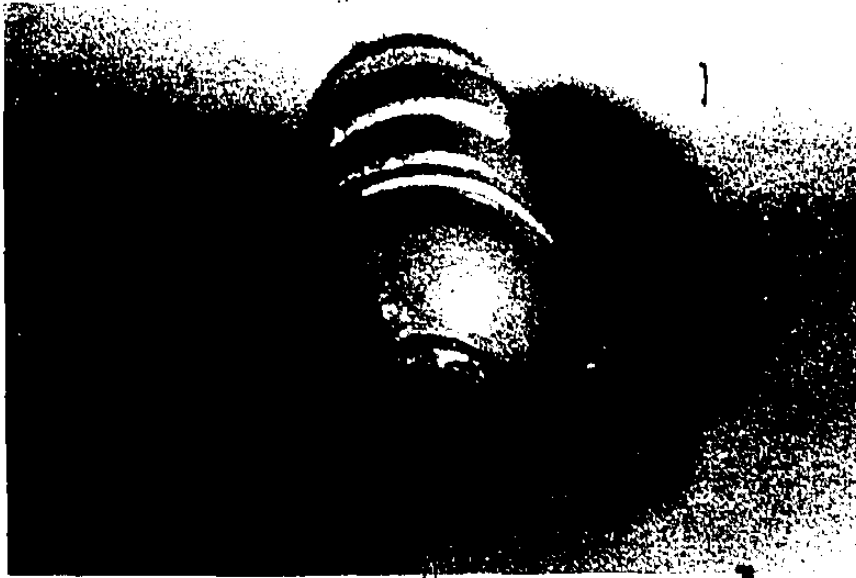


Fig. 36: Front, Side and Rear View Of Fume Sampling Device



Fig. 37: Canister Holder And Filter Canisters

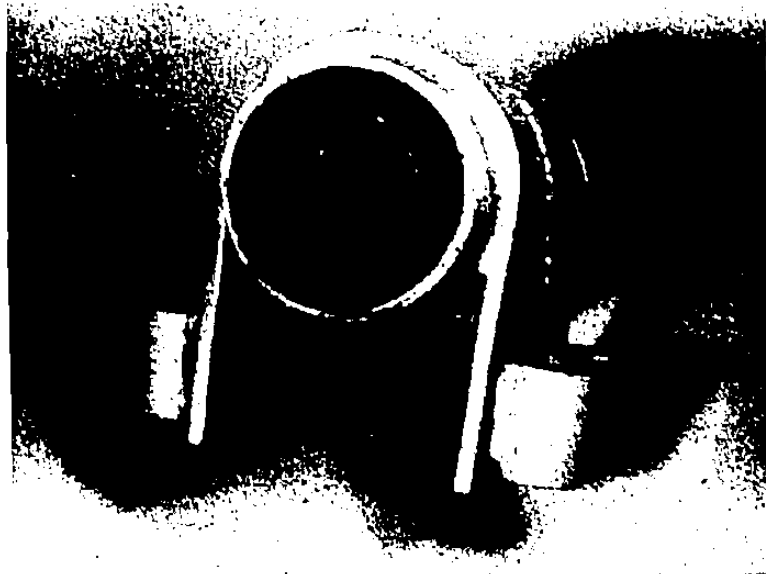


Fig. 38: Filter Canisters Installed In Sampling Device, Endcap Removed

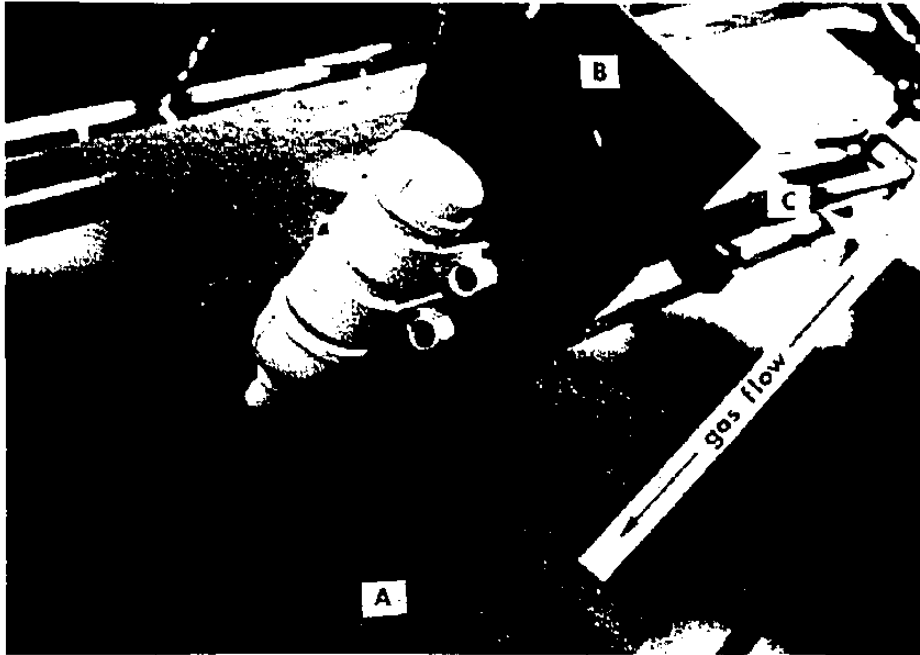


Fig. 39: Single Sampling Device

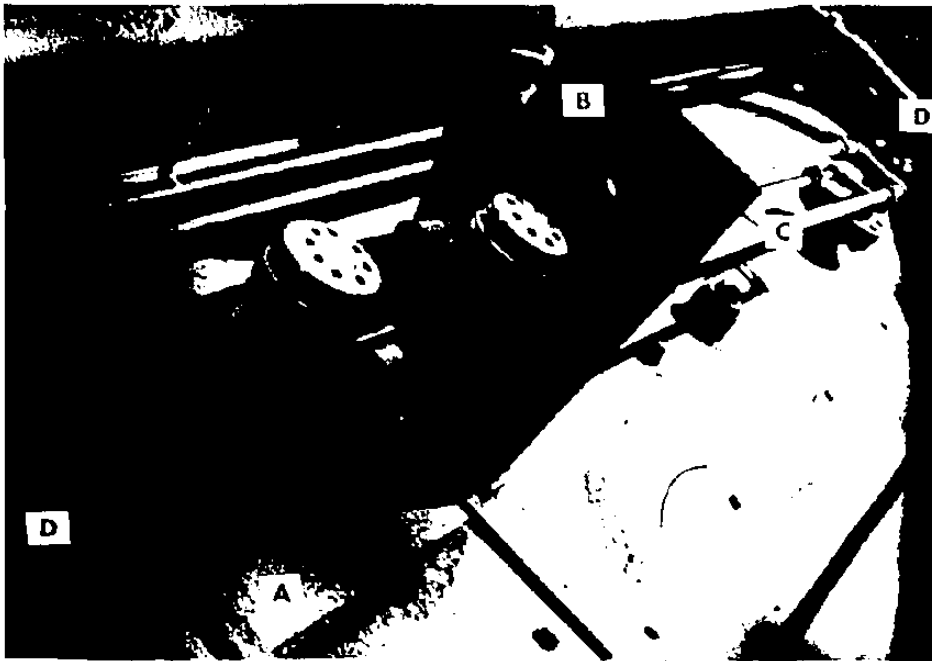


Fig. 40: Dual Sampling Devices For Representivity Tests

Fig. 39,40: Device Mounted on Down Duct  
 A) Access Door  
 B) Sampler Door  
 C) Support Rods  
 D) Water Spray Inlets

### 3.4 Effectiveness of Filter Canisters

Tests were conducted to determine if the filter canisters could collect all the material entering the sampler during a one minute sampling period. At first three filter canisters were used (three in a row instead of the two shown in Figures 35 and 37). The sampling procedure used was as follows:

Two ( $2 \pm .01$ ) grams of Longlife <sup>(R)</sup> filter material was placed in each filter canister and installed in the sampling device. The device was inserted in the duct and lowered to the centre of the duct where it was held for a period of one minute. The device was then removed from the duct and the filter material (now coated with fume particles) recovered.

Samples were taken at the 1, 5, 10, 15 and 20 minute mark of the blow. For each time period, clean filter material was used and a total of 5 heats were sampled.

The filter material was dried overnight at 65°C and weighed to determine the amount of fume material collected.

The results of these tests are listed in Table VIII. On average 17 weight percent of the total fume sample was collected in the second canister and 2.5 weight percent was collected in the third canister.



TABLE VIII

## QUANTITY OF FUME COLLECTED IN 2ND AND 3RD FILTER CANISTERS

Heat	Blowing Time (min.)	Weight % of Total Sample	
		in 2nd Canister	in 3rd Canister
1	1	15.07	1.64
	5	12.26	.32
	10	23.61	2.15
	15	30.32	3.19
	20	26.90	.51
2	1	17.72	1.80
	5	21.79	.73
	10	9.09	2.37
	15	28.94	5.26
	20	35.11	2.25
3	1	12.04	.22
	5	15.55	3.05
	10	1.19	2.77
	15	13.45	2.24
	20	37.38	1.86
4	1	8.25	2.97
	5	24.71	3.92
	10	9.03	4.86
	15	4.31	5.17
	20	8.00	2.00
5	1	8.92	3.69
	5	4.45	.41
	10	11.35	2.70
	15	37.00	2.00
	20	29.67	3.29
Mean		17.12	2.45
Std. Dev.		11.44	1.43
Level of Significance		50%	70%

Any natural process that is measurable will have a spread in the data that comes from various errors in data gathering. If the error is the sum of many component errors which may or may not necessarily be normal, then their sum will tend towards a normal Gauss distribution. A statistical test determining the degree to which the sample data represents the total population (level of significance) can be carried out using the Chi-Square method. This method is illustrated in Appendix B. Normally a minimum of 20 data points are necessary to determine the level of significance. For industrial data, a 50% level of significance is generally acceptable; low significance levels indicate the presence of some influential parameter that should be controlled (kept constant). This data analysis method is used extensively in this work since it gives a good indication of whether a natural process is being accurately measured.

This test was applied to the data in Table VIII and the level of significance was equal to or greater than 50%, indicating that this data was representative of the total population. Since on average only 2.5% of the fume material is collected in the third canister, it was decided that only two canisters could be used without undue error being introduced. In all further tests, only two filter canisters were used.

### 3.5 Sampler Reproducibility

To check the reproducibility of the device, it is necessary to measure the quantity of fume evolved under similar conditions for several different heats.

The quality of scrap in the furnace charge has a strong influence on the quantity of fume evolved during a particular heat. For example, the mean fume sample weight at the one minute mark of the blow is 3.7 g for one type of scrap charge and 6.2 g for another. This influence of scrap quality is noticeable during the first 15 minutes of the blow, the period in which the majority of the scrap is dissolved. The effect of scrap quality on fume evolution is presented in detail in Section 4.5.

To check the reproducibility of the sampling device, fume samples were taken from the centre of the duct at the 20 minute mark of the blow for a period of one minute. Sets of 25 heats were measured to normalize the influence of variations in blowing practice (operator controlled) and batch time (refining time varies from 21 to 25 minutes). The mean sample weight was determined for each set and checked for level of significance using the Chi-Square method.

Four sets of heats corresponding to four different scrap types were measured. The scrap types were:

Set I - randomly mixed scrap

Set II - scrap type A

Set III - scrap type B

Set IV - scrap type C

The results of these tests are shown in Table IX.

The mean sample weight for each of the four sets of heats are similar and range from 0.7 to 0.79 g. The level of significance of this data is also acceptable at 60 to 70%. As expected, the type of scrap has little or no influence.

The reproducibility of these results is calculated in Table X. If the true sample weight at the 20 minute mark is taken as the average of the four mean values, then the reproducibility is the difference between the measured value and the true sample weight. This difference is calculated in Table X and varies from -7.49% to + 6.84%.

These results indicate that the reproducibility error of the device is less than  $\pm 10\%$  which is an acceptable value.

TABLE IX  
FUME WEIGHT COLLECTED AT THE 20 MIN. MARK

No.	Sample Weight at 20 Min. (g)			
	SET I	SET II	SET III	SET IV
1	.76	1.04	.94	.45
2	.86	.54	1.30	.51
3	1.00	.87	.56	.39
4	.77	.46	1.03	.40
5	.44	.98	1.37	1.09
6	.58	.39	.69	.87
7	.76	.54	.70	.46
8	.67	.29	.53	.90
9	1.34	.56	.46	1.25
10	.68	.71	1.22	.68
11	.45	.69	1.03	.80
12	.72	.58	.56	1.29
13	1.30	.72	.91	.59
14	1.13	.79	.50	1.22
15	.27	.69	1.31	1.90
16	1.43	.55	.87	.40
17	.70	.68	.72	.37
18	1.01	1.21	.76	.28
19	.66	.84	1.05	.37
20	.3	.70	1.26	.43
21	.70	.88	.32	.46
22	.71	.56	.85	1.05
23	.89	1.15	.67	.99
24	.78	.62	.55	.88
25	.55	.78	.42	1.01
Mean	.78	.71	.82	.76
Std. Dev.	.29	.22	.31	.40
Level of Significance	70%	60%	60%	70%

TABLE X  
REPRODUCIBILITY OF RESULTS

Sample Set	Mean Sample Weight (20 min.) (g)	% Difference From Average*
I	.78	+ 1.63
II	.71	- 7.49
III	.82	+ 6.84
IV	.76	- 0.97
AVERAGE	.768	

\*  $\frac{\text{Value} - \text{Average}}{\text{Average}} \times 100\%$

### 3.6 Sample Representivity

The velocity of the gases in the duct is not constant across the width of the duct, as shown in Figure 32. If the dust particles are uniformly distributed throughout the gas (weight per unit volume), then for a fixed sampling time larger sample weights would be expected at the higher gas velocities.

To determine the representivity of the sample weight collected, fume samples were collected simultaneously from two positions across the duct. This was accomplished by mounting one sampler on a movable bracket attached to the support arms of the other. A photograph of this arrangement is shown in Figure 40. The two samplers can be positioned with an accuracy of  $\pm 5$  cm.

One device was always positioned at the 1.2 m (duct centre) position while the other was located at either the .6, .9, 1.5 or 1.8 m position. Samples were taken for a one minute period at the 1, 5, 10, 15 and 20 minute mark of the blow and the average fume sample weight was calculated. Twenty heats were measured for each of the four positions mentioned. The heats were chosen randomly.

The results of these tests are listed in Table XI. The mean sample weight for each set of measurements was determined and checked for level of significance. The level of significance ranged from 50 to 70% and is

TABLE XI

## FUME SAMPLE WEIGHT AT VARIOUS POSITIONS ACROSS THE DUCT

Heat Number	Average Fume Weight (g) Per Heat							
	SET A		SET B		SET C		SET D	
	0.6 m.	1.2 m.	0.9 m.	1.2 m.	1.2 m.	1.5 m.	1.2 m.	1.9 m.
1	.92	2.94	1.50	1.21	2.27	2.34	1.72	1.73
2	.92	2.21	1.59	1.56	2.35	2.21	1.98	2.45
3	.82	2.29	1.80	1.76	2.66	2.35	1.62	1.98
4	.85	2.61	1.62	1.71	2.42	1.91	2.29	2.20
5	1.06	2.66	2.25	1.78	2.08	1.89	2.07	1.39
6	.86	1.95	1.85	2.15	1.61	1.50	2.14	2.23
7	.77	2.06	1.12	1.96	2.60	2.18	1.79	1.67
8	.83	2.63	1.50	1.21	2.15	1.89	2.45	1.95
9	1.01	2.24	1.60	1.54	2.09	2.30	1.62	1.40
10	.91	2.67	1.55	1.90	2.95	3.03	1.30	2.20
11	.68	1.80	1.71	1.44	2.94	2.56	2.06	2.35
12	.79	1.88	1.22	1.92	2.47	2.48	2.16	1.78
13	.74	2.04	1.67	1.50	2.27	2.49	1.25	1.80
14	.89	1.38	1.34	1.53	3.46	2.69	1.23	1.67
15	.86	1.85	1.36	1.46	2.92	2.59	1.42	1.98
16	.78	1.84	1.71	1.30	2.97	3.24	1.98	1.96
17	.89	2.65	1.83	1.58	3.12	2.60	2.78	1.92
18	.62	1.89	1.70	1.90	2.89	2.93	1.11	1.96
19	.80	2.38	1.10	2.10	2.37	1.94	.91	1.58
20	.81	2.05	1.98	1.97	2.29	2.81	.92	2.25
21					2.10	2.00		
22					2.18	2.27		
23					2.51	2.33		
24					3.36	3.44		
25					2.50	2.31		
Mean	.84	2.20	1.60	1.68	2.35	2.51	1.74	1.92
Std. Dev.	.102	.396	.308	.303	.452	.443	.52	.412
Lev. of Sig.	60%	70%	50%	70%	50%	60%	50%	70%
[ Fume Wt. ] [ Fume Wt. ] [ (1.2 m) ]	.381		.953		1.068		1.103	
	[ .84 ] [ 2.20 ]							



acceptable. The ratio between the sample weight at the particular duct position to that at the duct centre was calculated (Table XI) for each set of measurements. This ratio is plotted along with the previously measured gas velocities in Figure 41.

In Figure 41, both ordinates are drawn to the same scale, and it can be seen that with the exception of the 0.6 m measurement, the fume weight ratio increases at approximately the same slope as the gas velocity.

There are two possible explanations for the small sample weight collected at the 0.6 m position. The first is the influence of the water sprays, one of which is located approximately 0.15 m downstream of the sampling point. The water spray is perpendicular to the gas flow, and this could interfere with the gas flow through the sampling device when sampling close to that side of the duct.

The second explanation is a similar influence caused by a large leakage of air around the access door. This would form a gas channel perpendicular to the sample nozzle as atmospheric air is sucked into the duct. When the sampler is not in use and the access door is open, such a channel has been observed to reach almost to the centre of the duct.

These results show that the device is sensitive to differences in gas velocity (as it should be) and that

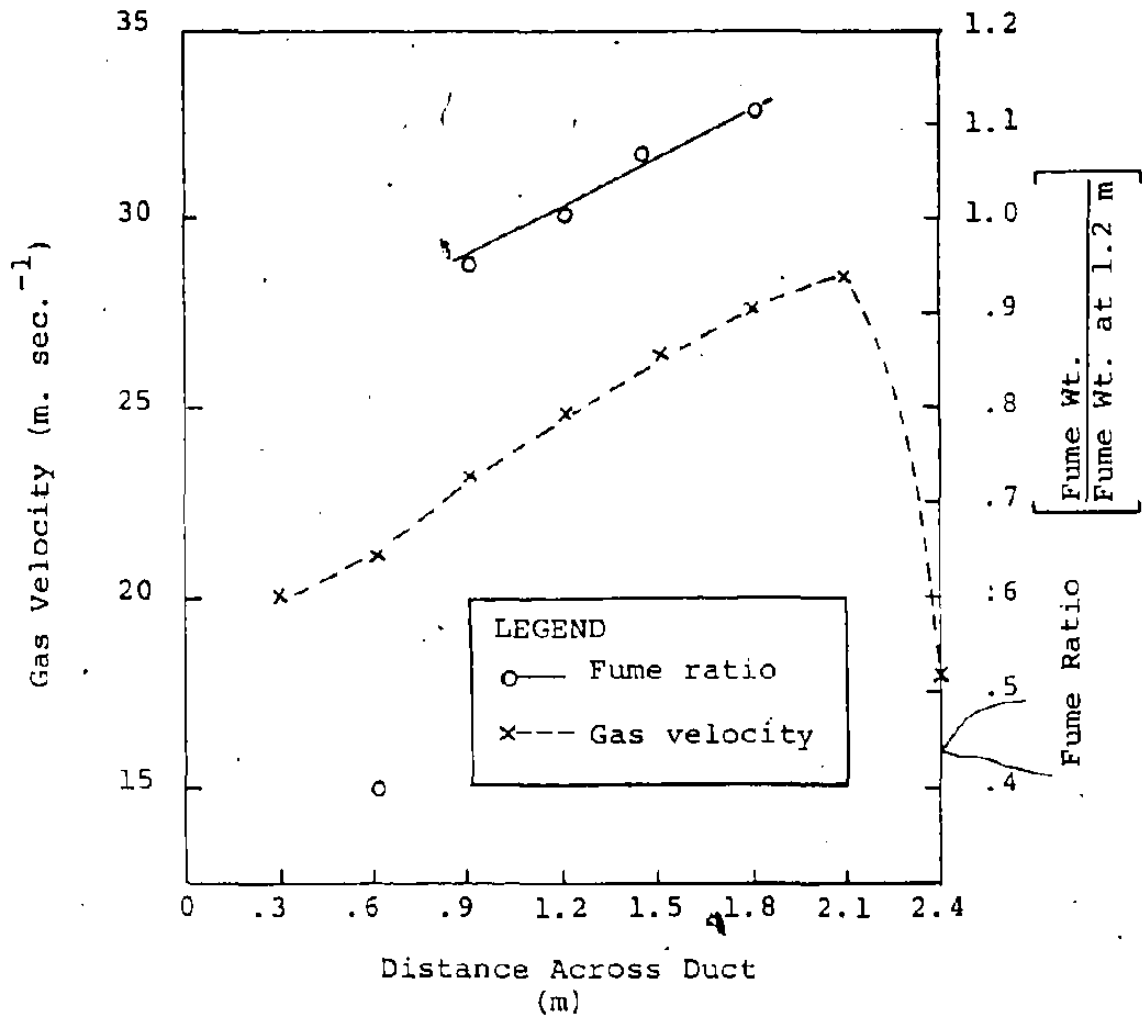


Fig. 41: Fume Weight and Gas Velocity Vs. Duct Position

the most representative sampling position is the centre of the duct, the position where the gas velocity is equal to the average of the gas velocities across the duct.

The results of the reproducibility and representivity test confirm that the device, when used in a statistical way (for a population of heats), gives results that are representative of the actual fume evolution rate.

#### 4. METHOD AND RESULTS

##### 4.1 Fume Weight Versus Blowing Time

To determine the quantity of fume evolved as a function of blowing time, samples were taken at the 1, 5, 8, 12, 15 and 20 minute points of the blow. The samples were taken from the centre of the duct for a period of one minute for 25 random heats.

The results of these tests are shown in Table XII. The mean sample weight was calculated for each time period and, in all cases, the level of significance exceeded 50%. The fume evolution rate decreases rapidly from  $4.86 \text{ g. min.}^{-1}$  to  $1.25 \text{ g. min.}^{-1}$  during the first half of the blowing time (0-12 min.); after which it decreases gradually to  $.78 \text{ g. min.}^{-1}$  over the second half of the blow.

The mean fume weight is plotted versus blowing time in Figure 42.

Approximately 40% of the heats made have an oxygen reblow because of off-aim steel analysis at first turn-down. The reasons for reblows can be improper bath C, Mn, S, temperature or high slag viscosity. Reblow fume samples were collected from 20 heats; the reblow times ranged from 15 seconds to 1 minute. The fume weights were converted to  $\text{g. min.}^{-1}$  assuming a linear relationship between fume evolution and time. These weights are listed in Table XIII. The mean reblow fume weight is .51g.

TABLE XII  
FUME WEIGHT VERSUS BLOWING TIME

No.	Fume Weight (g) at Various Blowing Times (Min.)					
	1	5	8	12	15	20
1	4.09	2.17	1.75	1.17	.59	.76
2	4.56	3.10	1.24	.82	1.06	.86
3	4.38	4.13	1.34	.89	1.30	1.00
4	4.60	3.60	1.24	.83	.98	.77
5	4.45	2.47	1.10	.74	.76	.44
6	2.17	2.07	.60	.40	.48	.58
7	5.82	2.94	.97	.65	.79	.76
8	4.17	2.71	1.43	.95	.75	.67
9	2.04	3.41	3.93	2.64	1.24	1.34
10	4.86	2.95	1.70	1.13	1.09	.68
11	6.20	2.67	1.47	.98	.76	.45
12	4.79	3.31	3.30	2.20	1.38	.72
13	4.20	3.06	3.59	2.39	1.86	1.30
14	6.87	4.47	3.17	2.11	1.49	1.13
15	5.40	4.65	2.42	.94	1.02	.27
16	4.74	2.58	1.86	1.24	1.36	1.43
17	6.78	3.85	.84	.56	.75	.70
18	7.51	5.31	1.42	1.50	1.67	1.01
19	3.63	5.71	1.33	.89	.81	.66
20	5.89	4.53	1.78	1.18	.75	.31
21	3.69	4.18	1.42	.95	.67	.70
22	5.12	4.39	1.66	1.10	.76	.71
23	4.04	5.42	1.67	1.80	1.51	.89
24	8.28	3.95	2.70	1.12	.56	.78
25	3.21	3.60	2.92	1.94	.62	.55
Mean	4.86	3.65	1.87	1.24	1.00	.78
Stan. Dev.	1.53	1.01	.89	.58	.38	.29
Level of Significance	50%	70%	60%	50%	50%	70%

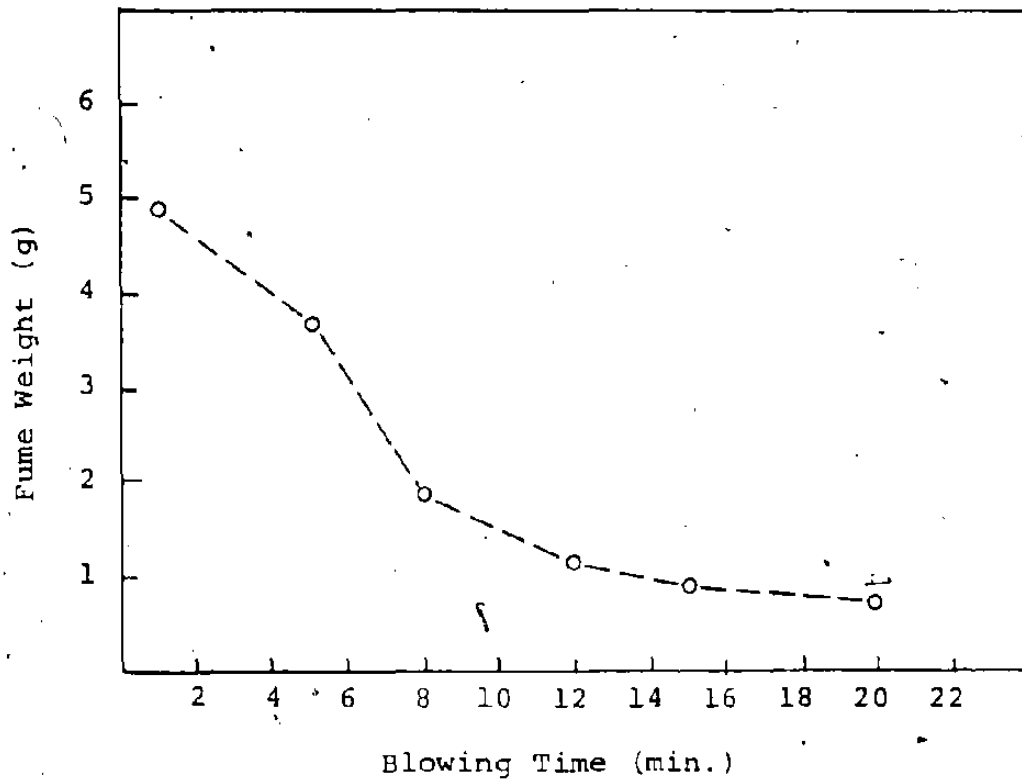


Fig. 42: Fume Weight Vs. Blowing Time

TABLE XIII  
REBLOW FUME WEIGHT

No.	Reblow Fume Weight (g. min. <sup>-1</sup> )
1	.76
2	.40
3	.65
4	.34
5	.73
6	.29
7	.42
8	.42
9	.53
10	.50
11	.42
12	.54
13	.59
14	.63
15	.52
16	.66
17	.41
18	.46
19	.58
20	.39
Mean	.51
Stan. Dev.	.13
Level of Significance	70%

#### 4.2 Chemical Analysis of Fume

Fume material from twenty random heats was submitted for chemical analysis. The fume material is separated from the filter material by shaking. Chemical analysis for metallic iron, ferrous and ferric iron, CaO, MgO and MnO were performed using wet analysis methods.

The average chemical analysis for each of these elements as a function of blowing time is listed in Table XIV and plotted in Figure 43. Other elements which are present in the fume (overall average values) are: Al<sub>2</sub>O<sub>3</sub> (.2%), SiO<sub>2</sub> (1.2%), S (.2%), Zn (2.4%), Pb (.3%) and CO<sub>2</sub> (8.2%). An average CO<sub>2</sub> concentration of 8.2% for an average CaO and MgO of 8.23 and 3.11% respectively (see Table XIV) indicates that approximately 80% of the flux particles in the fume reacted with CO<sub>2</sub> in the off-gases to form CaCO<sub>3</sub> and MgCO<sub>3</sub>.

The average iron loss in the fume as a function of blowing time is calculated in Table XV using the average fume weights (Table XII) and the average total iron analysis (Table XIV). These results are also plotted in Figure 44.

It was mentioned in Section 2.3.1 that the vapour pressure of Mn is 100 to 1000 times that of pure Fe at steelmaking temperatures and that the ratio of Mn/Fe in fume to that in the bath is an indication of the mechanism



of fume formation. Large ratios (approx. 100) indicate a mechanism of direct vapourization, while small ratios (approx. 1) indicate oxidation of metal spray.

The Mn content of the fume was calculated by connecting the MnO content of the fume in Table XIV to Mn. The Mn and total Fe analysis of the fume were checked for level of significance using the Chi-Square method. The results are listed in Table XVI. In all cases, the significance exceeded the acceptable limit of 50% and ranged from 50 to 80%.

The Mn/Fe ratios are calculated as a function of blowing time for both the fume and metal bath and are listed in Table XVII. The Mn and Fe contents of the metal bath were taken from a previous Dofasco study by Laciak<sup>24</sup>. The ratio of Mn/Fe in the fume to that in the bath ranges from 2.19 to 17.20. The Mn/Fe ratios are plotted versus blowing time in Figure 45.

In Table XVII, results are also listed for the reblow fume. The Mn and total Fe content of the reblow fume is from the analysis of the combined 20 reblow fume samples.

TABLE XIV

FUME ANALYSIS AT VARIOUS BLOWING TIMES  
 (Average of 20 Samples per Time Period)

Time (min.)	Analysis Weight %							$\frac{\text{Fe}_2\text{O}_3}{\text{FeO}}$
	Fe <sup>met</sup>	FeO	Fe <sub>2</sub> O <sub>3</sub>	Fe <sup>Tot</sup>	CaO	MgO	MnO	
1	0.46	15.61	50.90	48.19	7.14	5.08	1.00	3.26
5	0.41	6.69	40.53	33.96	21.50	6.17	0.65	6.06
8	0.38	9.96	52.67	43.41	8.04	4.37	0.63	6.62
12	0.39	11.35	68.20	56.92	4.82	1.42	1.00	6.01
15	0.36	11.85	71.50	59.59	3.37	.68	1.25	6.03
20	0.39	15.43	66.45	58.88	4.55	.95	2.10	4.31
Overall Average	0.40	11.48	58.40	50.16	8.23	3.11	1.11	5.38

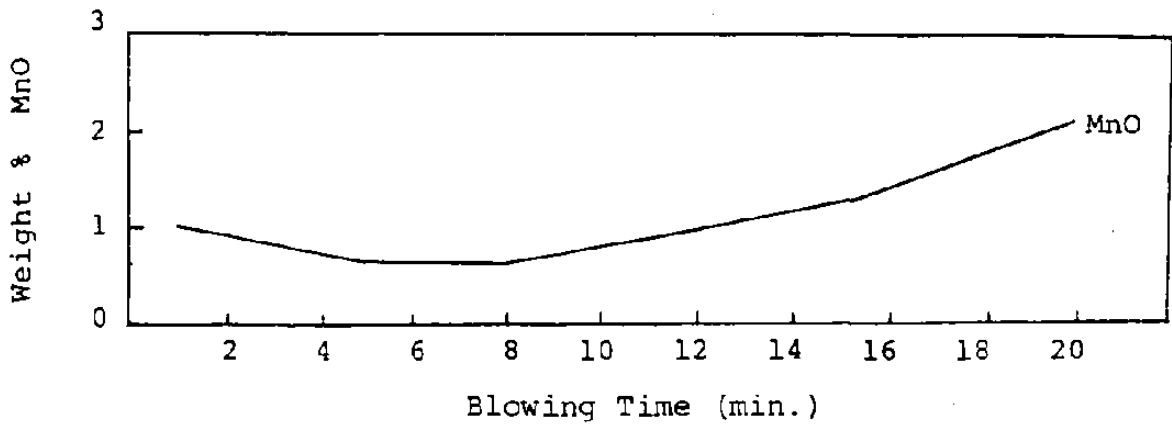
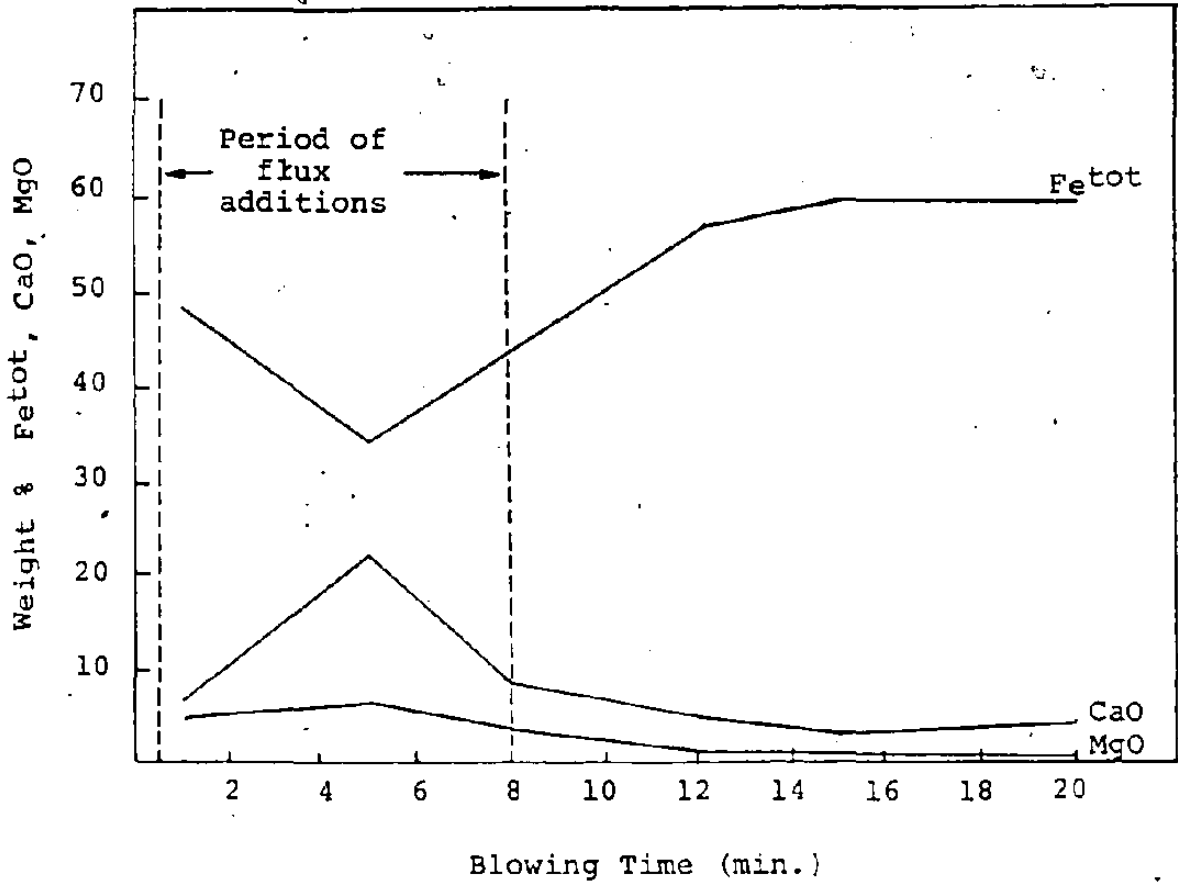


Fig. 43: Fume Analysis Vs. Blowing Time

TABLE XV

TOTAL IRON IN FUME VERSUS BLOWING TIME

Time (min.)	Fume Weight* (g)	% Fe Total**	Iron Weight (g)
1	4.86	48.19	2.34
5	3.65	33.96	1.24
8	1.87	43.41	.81
12	1.24	56.92	.71
15	1.00	59.59 <sup>r</sup>	.58
20	.78	58.88	.43

\* From Table XI

\*\* From Table XIII

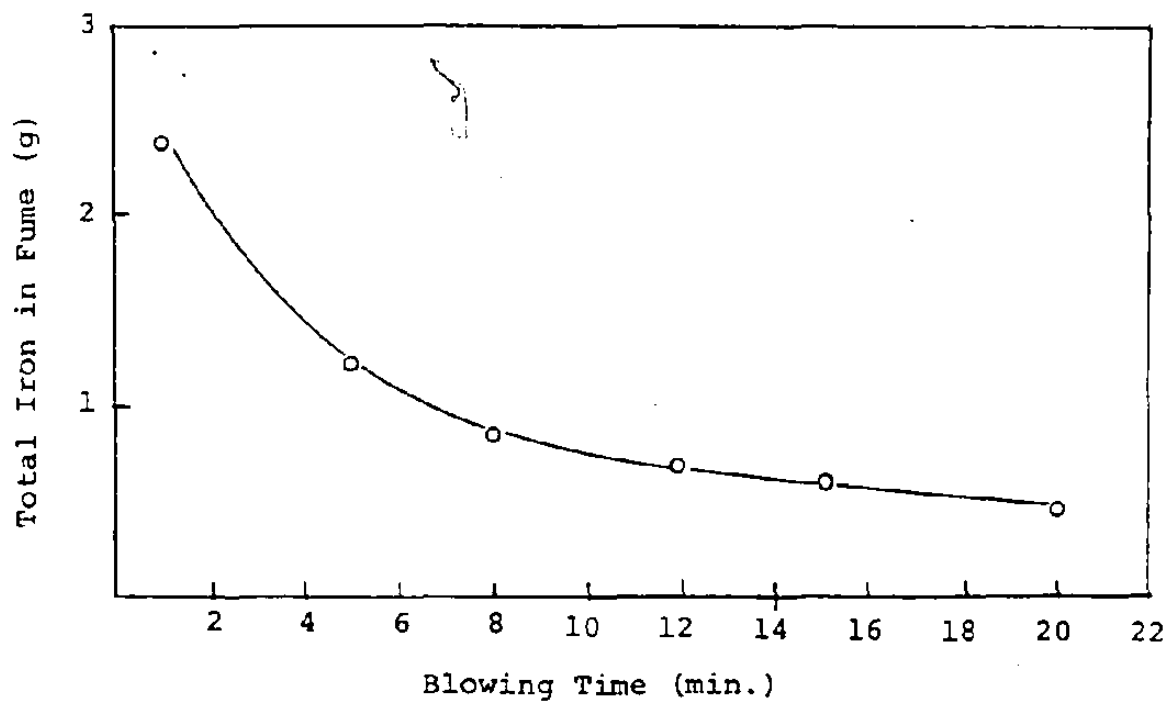


Fig. 44: Total Iron in Fume Versus Blowing Time

TABLE XVI

LEVEL OF SIGNIFICANCE OF IRON AND MANGANESE ANALYSIS

Time (min.)	Total Fe (%)			Mn (%)		
	Mean	Stan. Dev.	Level of Significance	Mean	Stan. Dev.	Level of Significance
1	48.19	8.10	70%	.76	.25	50%
5	33.96	4.45	50%	.51	.21	60%
8	43.41	6.95	60%	.49	.20	70%
12	56.92	3.22	80%	.76	.37	60%
15	59.59	1.85	50%	.97	.29	60%
20	58.88	2.36	60%	1.63	.57	80%

TABLE XVII

Mn TO Fe RATIO IN BATH AND FUME  
(Average of 20 Samples per Time Period)

Time	BATH*			FUME			$\frac{\text{Mn}}{\text{Fe}}$	Fume
	% Fe	% Mn	$\frac{\text{Mn}}{\text{Fe}} \times 10^{-2}$	% Fe	% Mn	$\frac{\text{Mn}}{\text{Fe}} \times 10^{-2}$	$\frac{\text{Mn}}{\text{Fe}}$	Bath
1	94.0	.68	.723	48.19	.76	1.58		2.19
5	96.7	.15	.155	33.96	.51	1.50		9.68
8	97.0	.11	.113	43.41	.49	1.13		10.00
12	98.0	.13	.132	56.92	.76	1.33		10.08
15	98.4	.17	.173	59.59	.97	1.63		9.42
20	99.4	.16	.161	58.88	1.63	2.77		17.20
Reblow	99.6	.14	.141	45.60	.98	2.14		15.17

\* from Reference 24.

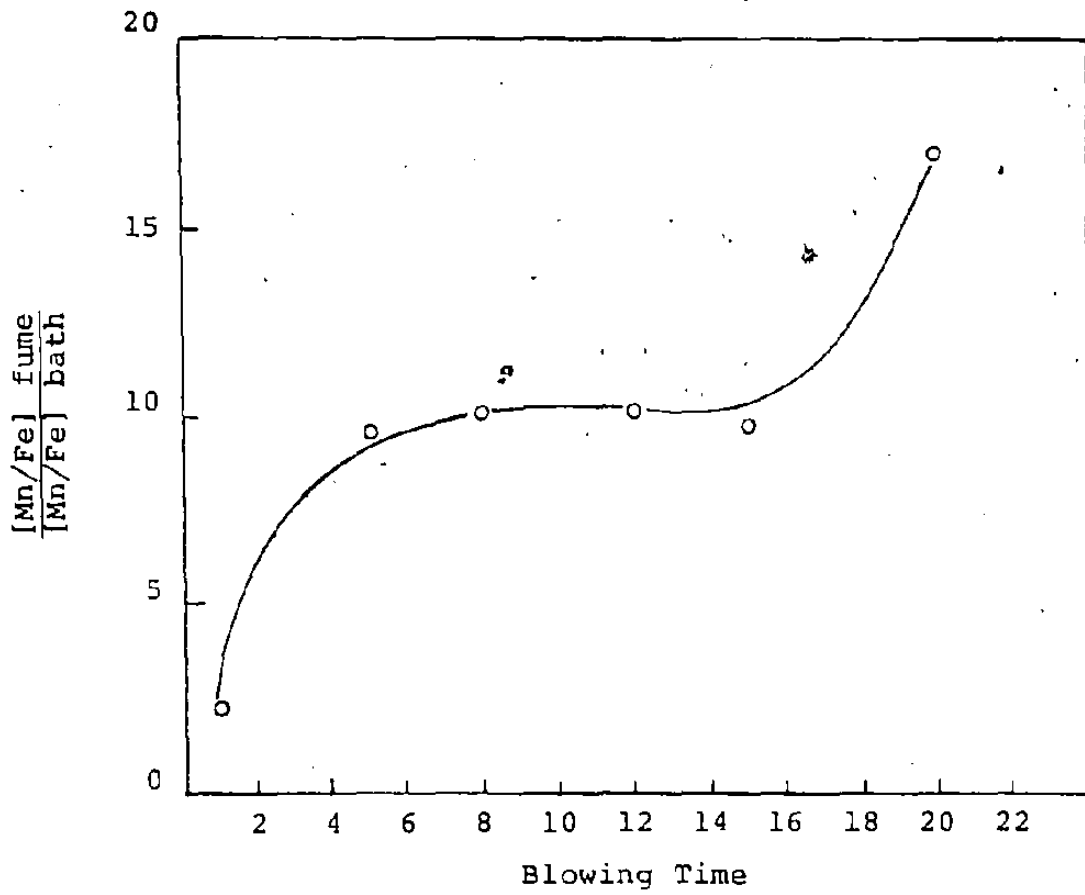


Fig. 45: Mn/Fe Ratio Vs. Blowing Time

#### 4.3 Total Iron in Fume Versus Bath Carbon

The decrease in bath carbon as a function of blowing time has been determined for Dofasco oxygen furnaces and is discussed elsewhere<sup>24</sup>. The average total iron in the fume (from Table XV) and the average bath carbon content are listed as a function of blowing time in Table XVIII. This data is plotted in Fig. 46.



TABLE XVIII

TOTAL IRON IN FUME VS. BATH CARBON

Time	Iron in Fume* (g)	Bath Carbon % [24]
1	2.34	3.90
5	1.24	3.30
8	.81	2.10
12	.71	1.90
15	.58	1.50
20	.43	.60

\* From Table XIV

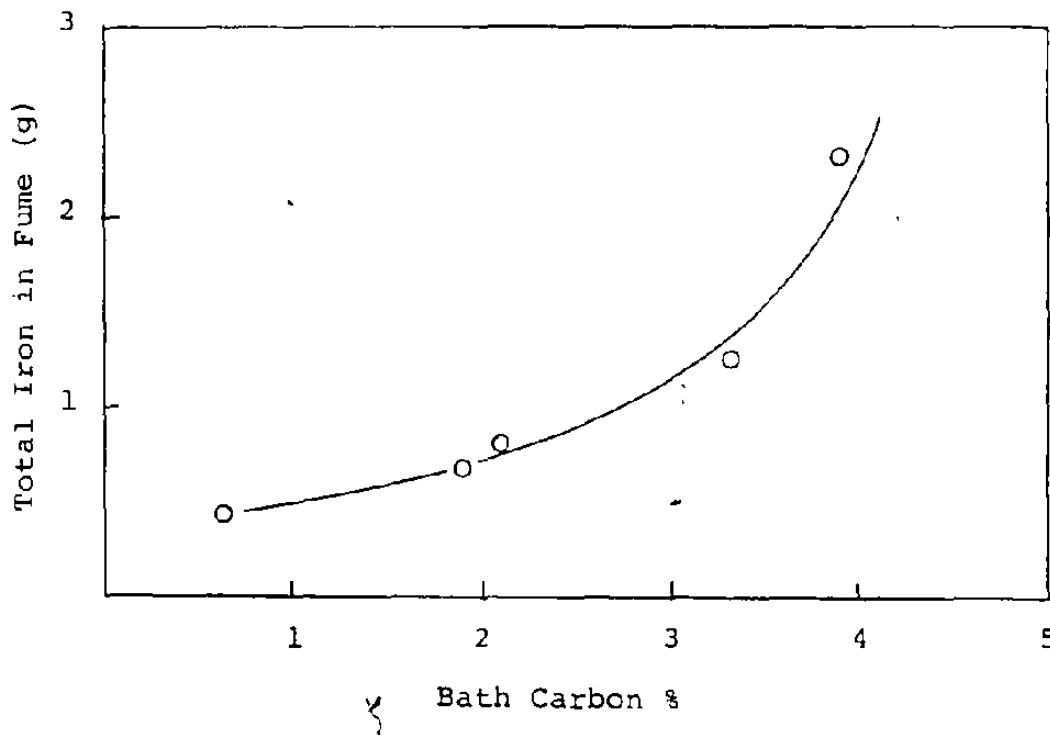


Fig. 46: Total Iron in Fume Vs. Bath Carbon

#### 4.4 Total Iron in Fume Versus Slag Weight

The slag weight at any time during the blow can be calculated using a silicon balance. This requires knowledge of the silicon content of the hot metal, scrap and fluxes charged to the furnace, as well as the silica analysis of the slag.

The slag weight as a function of blowing time has been calculated<sup>[85]</sup> for an average Dofasco heat and is listed along with the total iron in the fume in Table XIX. This data is plotted in Fig. 47.

TABLE XIX  
TOTAL IRON IN FUME AND SLAG WEIGHT  
AS A FUNCTION OF BLOWING TIME

Time	Total Iron in Fume* (g)	Slag Weight (kg) [85]
1	2.34	4100
5	1.24	9500
8	.81	10600
12	.71	10700
15	.58	11300
20	.43	13800
Turndown		18300

\* From Table XIV

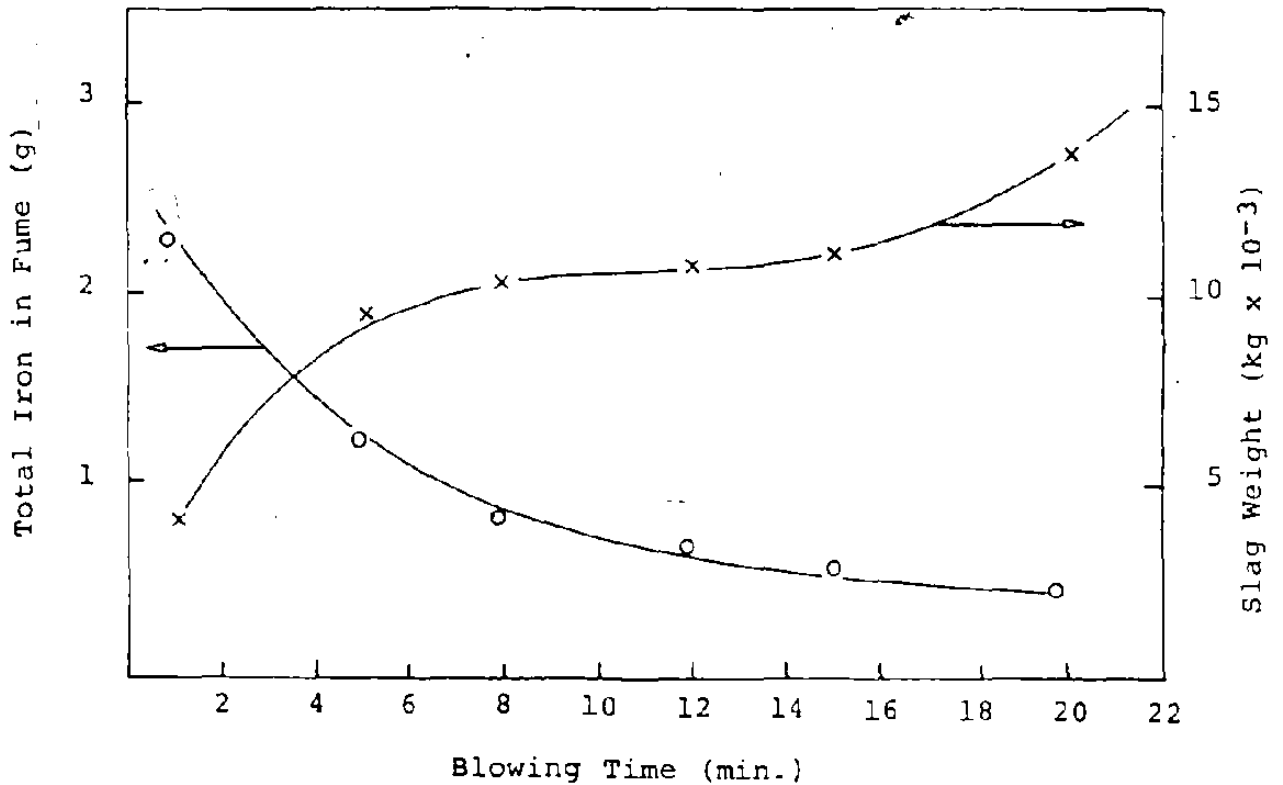


Fig. 47: Total Iron in Fume and Slag Weight as a Function of Blowing Time

#### 4.5 Effect of Scrap Quality

To determine the effect of scrap quality on the quantity of fume evolved, heats with specially prepared scrap charges were sampled. The iron oxide content (in the form of rust) of the three scrap charges were:

- A     Approx. 1% iron oxide
- B     Approx. 3% iron oxide
- C     Approx. 5% iron oxide

Samples were taken at the 1, 5, 8, 12, 15 and 20 minute mark of the blow and 25 heats were sampled for each of the three scrap classifications.

The mean fume weights as a function of blowing time are listed for the three scrap types in Table XX. The level of significance of these results was checked using the Chi-Square method and in all cases equalled or exceeded the acceptable limit of 50%. The data in Table XX are plotted in Fig. 48.

It was mentioned in Section 2.3.4 that bath temperature through its effect on the metal fluidity can influence the quantity of fume produced. To reduce and melt iron oxide in the B.O.F. requires approximately four times the heat to melt pure iron; therefore, scrap with a high iron oxide content should cause lower metal temperatures.

To determine the effect of scrap melting on metal temperature, direct measurements were taken, without stopping the blow, using consumable "bomb" type thermocouples. Ten heats of each of the "A" and "B" scrap type heats were tested.

The average metal temperatures as a function of blowing time are plotted in Figure 49. The metal temperature for the "B" type scrap (higher fume weights) is consistently less than that for the "A" type scrap. The iron oxide content of the "B" scrap is approximately three times that of the "A" scrap.

TABLE XX

FUME WEIGHT VS. BLOWING TIME FOR DIFFERENT SCRAP TYPES  
(20-25 Samples Per Time Period)

Time (min.)	Fume Weight (g)								
	TYPE A SCRAP			TYPE B SCRAP			TYPE C SCRAP		
	Mean	St. Dev.	Level of Significance	Mean	St. Dev.	Level of Significance	Mean	St. Dev.	Level of Significance
1	3.70	1.06	70%	4.86	1.53	50%	6.23	2.33	50%
5	3.10	1.07	60%	3.51	1.01	80%	3.92	1.20	80%
8	1.31	.56	70%	1.71	1.11	70%	2.07	1.34	70%
12	.82	.32	70%	1.14	.46	70%	1.38	.56	80%
15	.75	.29	60%	1.00	.38	70%	.99	.31	70%
20	.71	.22	60%	.82	.31	60%	.76	.37	60%
Average	1.73			2.19			2.56		
$\frac{\text{Avg.} - \text{Avg. Type "A"}}{\text{Avg. Type "A"}} \times 100\%$				26%			48%		

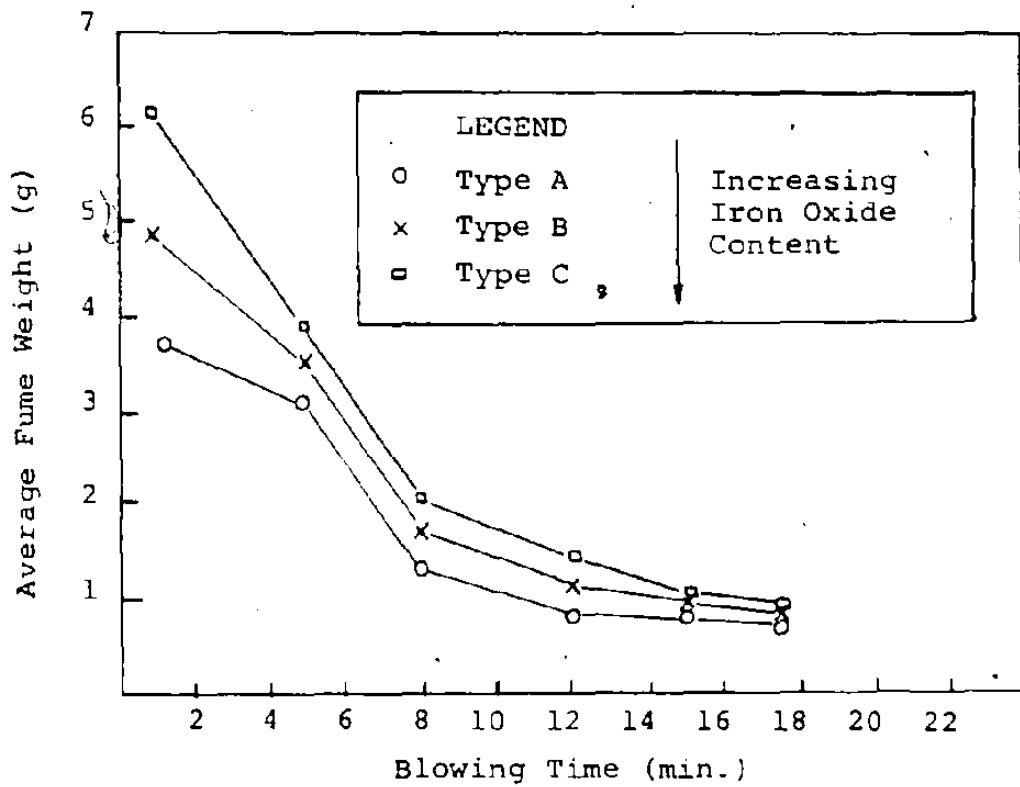


Fig. 48: Effect of Scrap Quality on Fume Weight

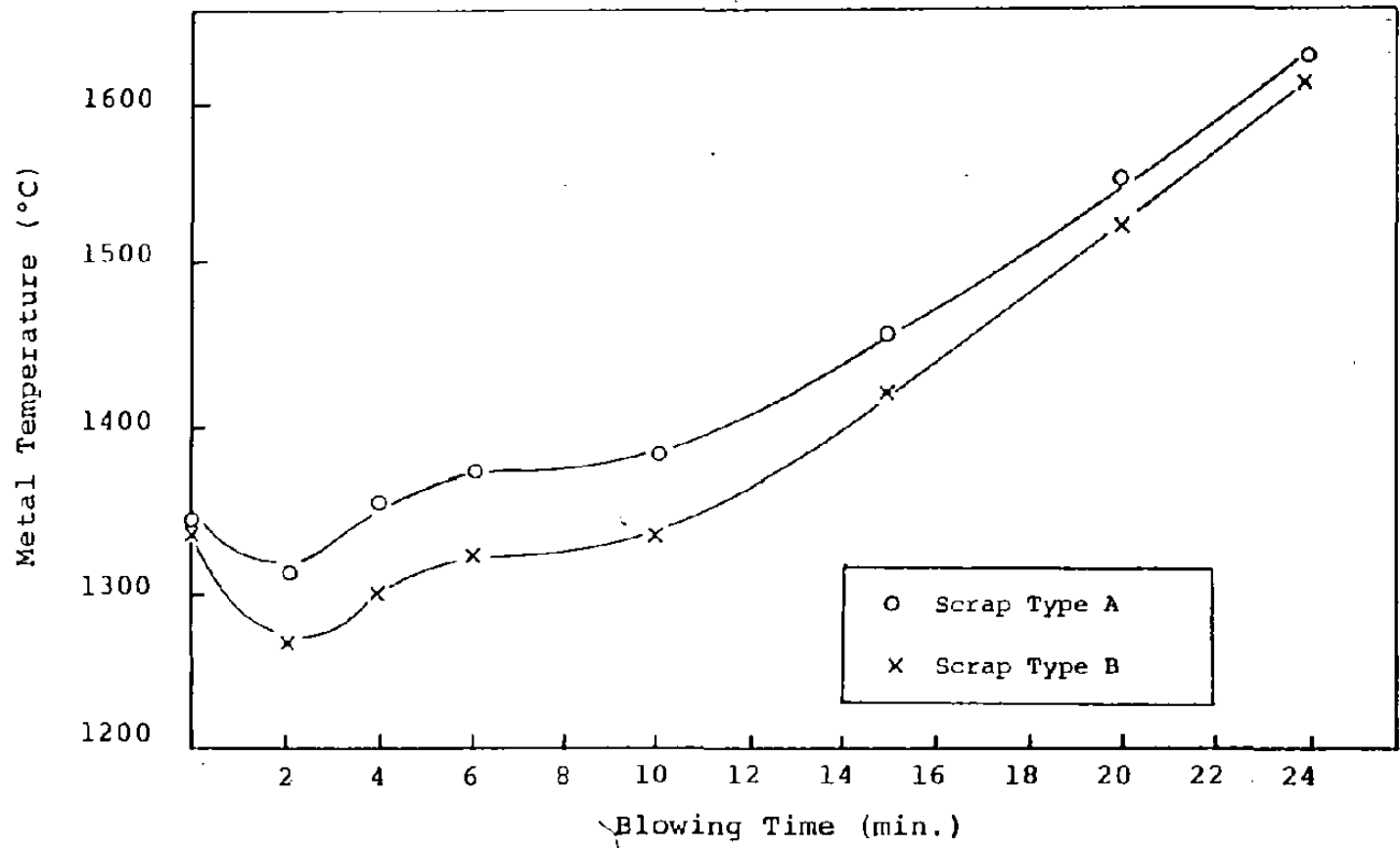


Fig. 49: Metal Temperature Vs. Blowing Time  
 (Each value is average of ten measurements)



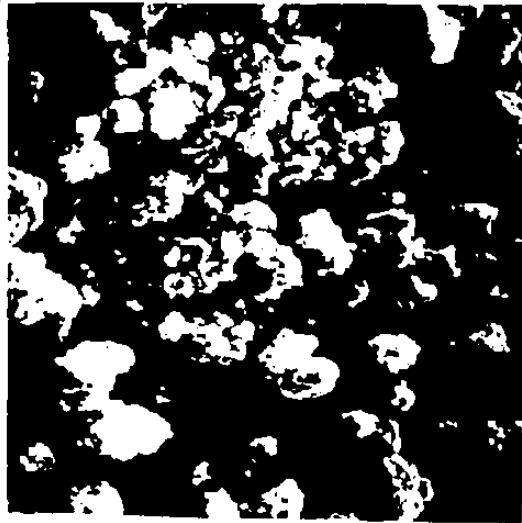
#### 4.6 Microscopic Examination of Fume

The fume collected from 20 random heats was combined according to blowing time to give six bulk samples (1,5,8,12,15 and 20 minute mark). The 20 reblow samples were also combined to give one bulk sample. From these bulk samples, smaller quantities of fume were taken for microscopic observation using the Scanning Electron Microscope (S.E.M.) and the Transmission Electron Microscope (T.E.M.) and for size analysis.

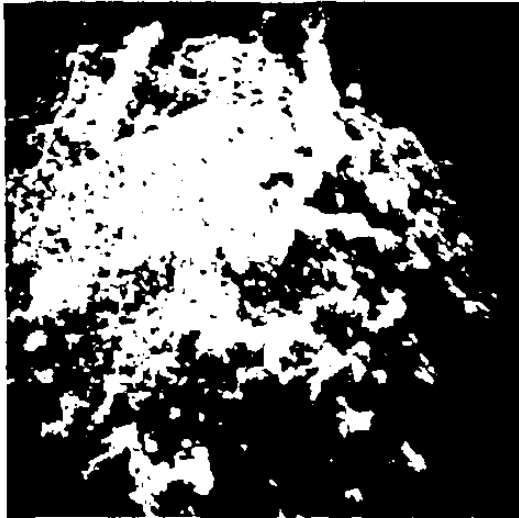
##### S.E.M. Results

To ensure good conductivity of the sample in the S.E.M., the fume samples were coated with aluminum by vapour deposition. S.E.M. photographs of the fume material are shown in Figure 50, the magnification range from 100 to 5000X. These particular photographs are of the 12 minute fume material, but they are typical of all of the fume material collected irrespective of blowing time.

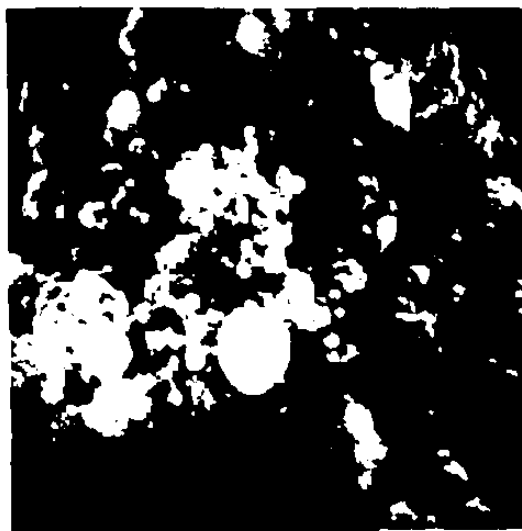
The fume particles as shaken from the filter material consist of angular and spherical particles (Figure 50a). The single spherical particles range in size from 10  $\mu$ m to 1 mm in diameter and are classified (from the definition of fume in Section 2.2) as metallic ejections. At higher magnifications



(a) 100X



(b) 1000X



(c) 5000X

Fig. 50: Scanning Electron Microscope  
Photographs Of 12 Minute Fume

(Figure 50b and c), the angular particles can be observed to consist of agglomerations of many small spherical particles, the majority of which are less than 1  $\mu\text{m}$  in diameter; these are the iron oxide fume particles.

#### T.E.M. Results

Samples of the fume material from each time period were mixed with water (.1 g in 20 ml) and placed in an ultrasonic bath for approximately 30 minutes. This dispersed solution was then placed, using an eye dropper, on 200 mesh copper grids that had been covered with a parlodian film.

T.E.M. photographs of the fume material are shown in Figures 51 and 55; the magnifications range from 1000 to 80000 times. These photographs are also of the 12 minute material, but they are indicative of the fume for all of the time periods sampled.

Even after 30 minutes of ultrasonics, the fume particles still form agglomerates as seen in Figure 51 (1000 magnification) and Figure 52 (10000 magnification), and it is evident that the majority of the individual particles are less than 1  $\mu\text{m}$  in diameter.

At higher magnifications, Figure 53 through 55 (20000, 40000 and 80000X), it can be seen that both spherical and multi-faceted fume particles are present. The presence of both of these shapes were observed in the fume material from every time period sampled. The particular photographs shown are of the 12 minute fume sample. A group of particles, all less than .2  $\mu\text{m}$  in diameter, are shown in Figure 55. It can be seen that even these smaller particles consist of both spherical and faceted shapes.

Fig. 51:

1000X



Fig. 52:

10000X



Fig. 53:

20000X

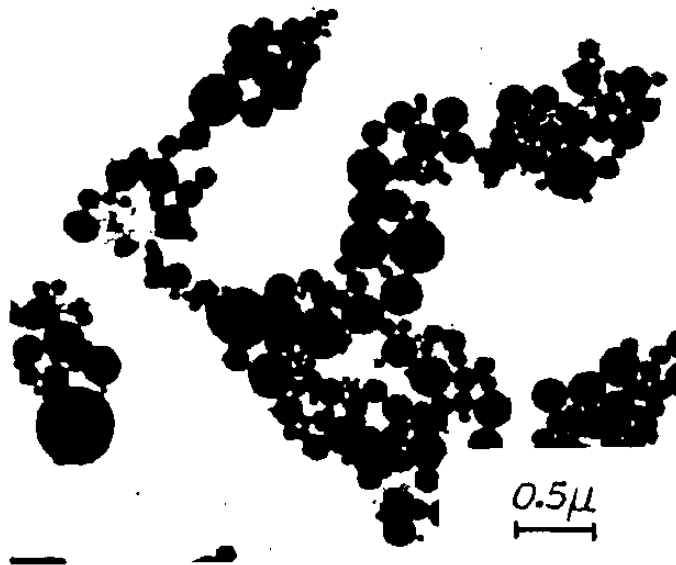


Fig. 51,52,53: Transmission Electron Microscope Photographs of 12 Minute Fume



Fig. 54: T.E.M. Photograph Of 12 Minute  
Fume, 40000X

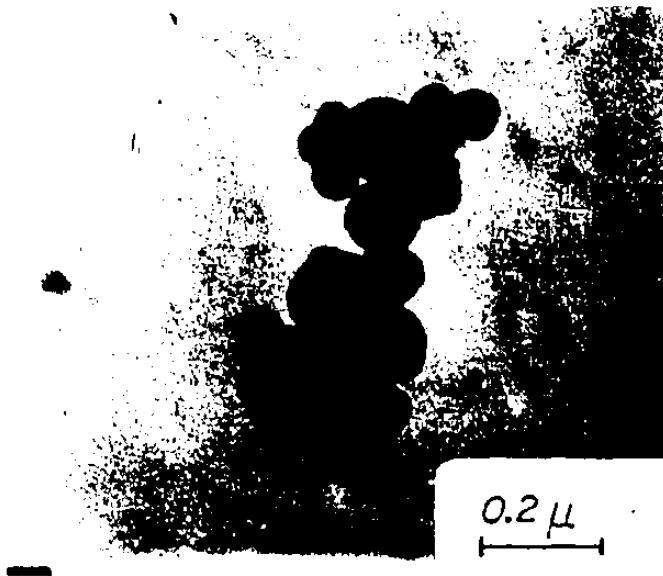


Fig. 55: T.E.M. Photograph Of 12 Minute  
Fume, 80000X

#### 4.7 Size Distributions of Fume Material

##### 4.7.1 Method and Accuracy

Size distributions were performed using T.E.M. photographs and manual sizing with a Zeiss Particle Sizer instrument. T.E.M. photographs were taken of the fume material for each time period at magnifications of 15000 to 20000 times. The fume particles were then manually counted and sized using the Zeiss instrument.

The Zeiss instrument can separate the particle sizes into 45 different ranges. To size the material, it is necessary to line up each particle with a circular light beam and trip a switch that records the particle size on a counter. From 1000 to 1500, particles were counted for each sample. The final number of particles in each size range was then used to determine the frequency distribution. The weight distribution was then calculated from the frequency distribution assuming spherical particles of constant density.

A histogram of one frequency distribution and the corresponding weight distribution (12 minute sample) are shown in Figure 56. The frequency distribution is skewed to the left, but the weight percent distribution resembles a Gaussian curve. This pattern was observed for the distributions from every time period sampled.

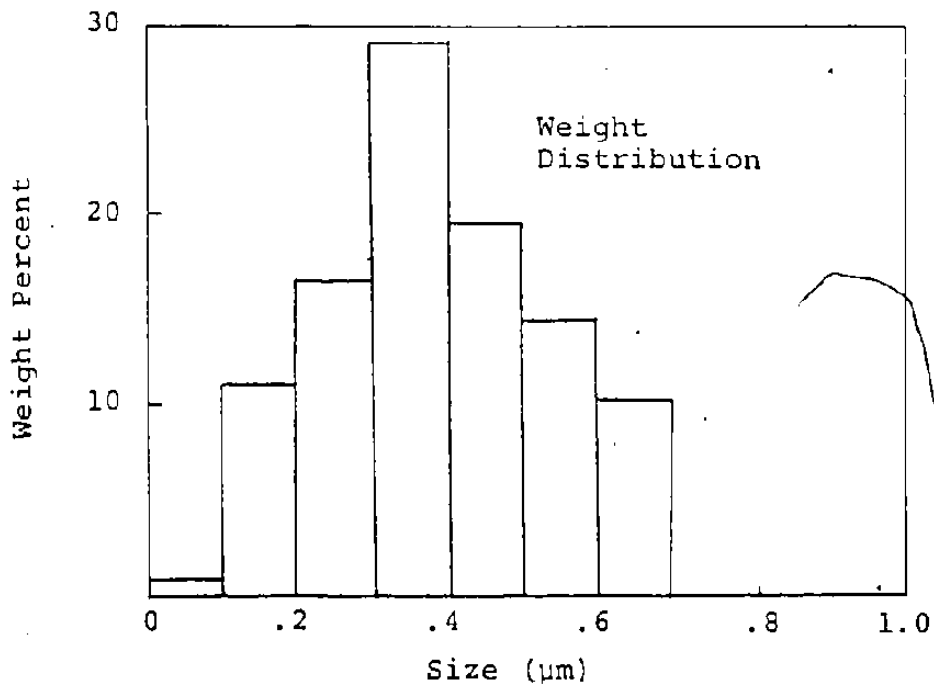
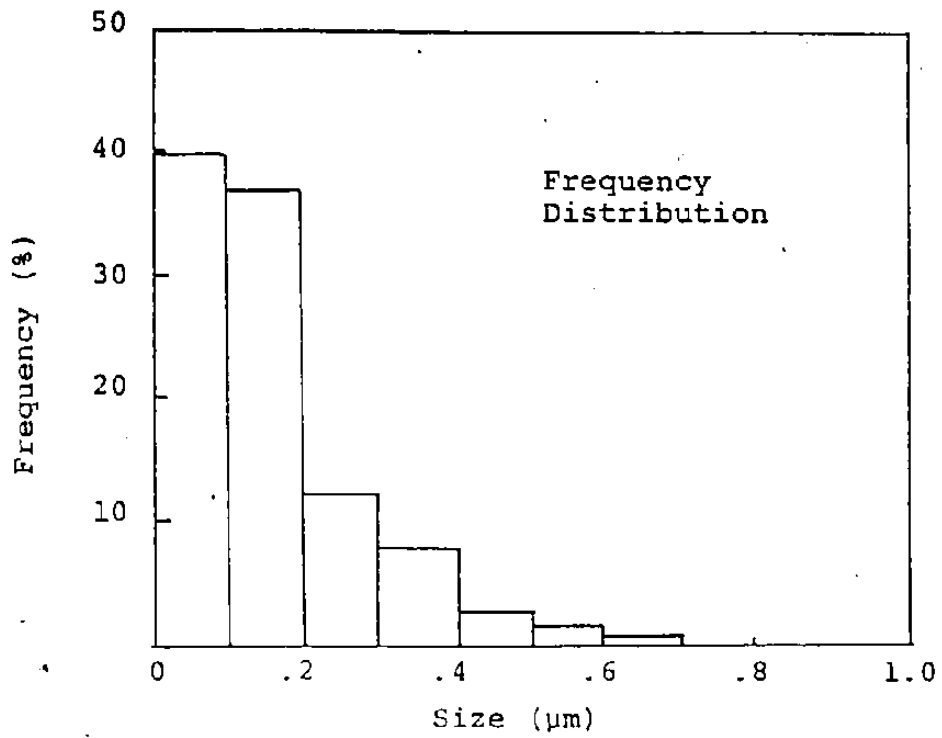


Fig. 56: Typical Frequency and Weight Distributions (20 Minute Sample)



The percentage standard error of the mean size in a frequency distribution is  $100/\sqrt{n}$  where n is the total number of particles counted<sup>86</sup>. In the case of 1000 counts, the error should be about 3.2%. The reproducibility of the size analysis was also checked by sizing three separate samples of the 12 minute fume material. The weight percent distributions of the three samples are shown in Figure 57. They are similar in shape and the calculated mean particle sizes are .36, .37 and .40  $\mu\text{m}$ . The reproducibility of the size analysis is calculated in Table XXI, assuming that the true mean particle size is the average of the three measured values. The reproducibility is about  $\pm 6\%$ , still an acceptable value.

The individual frequency and weight percent data and distributions for the reproducibility tests are shown in Appendix C.

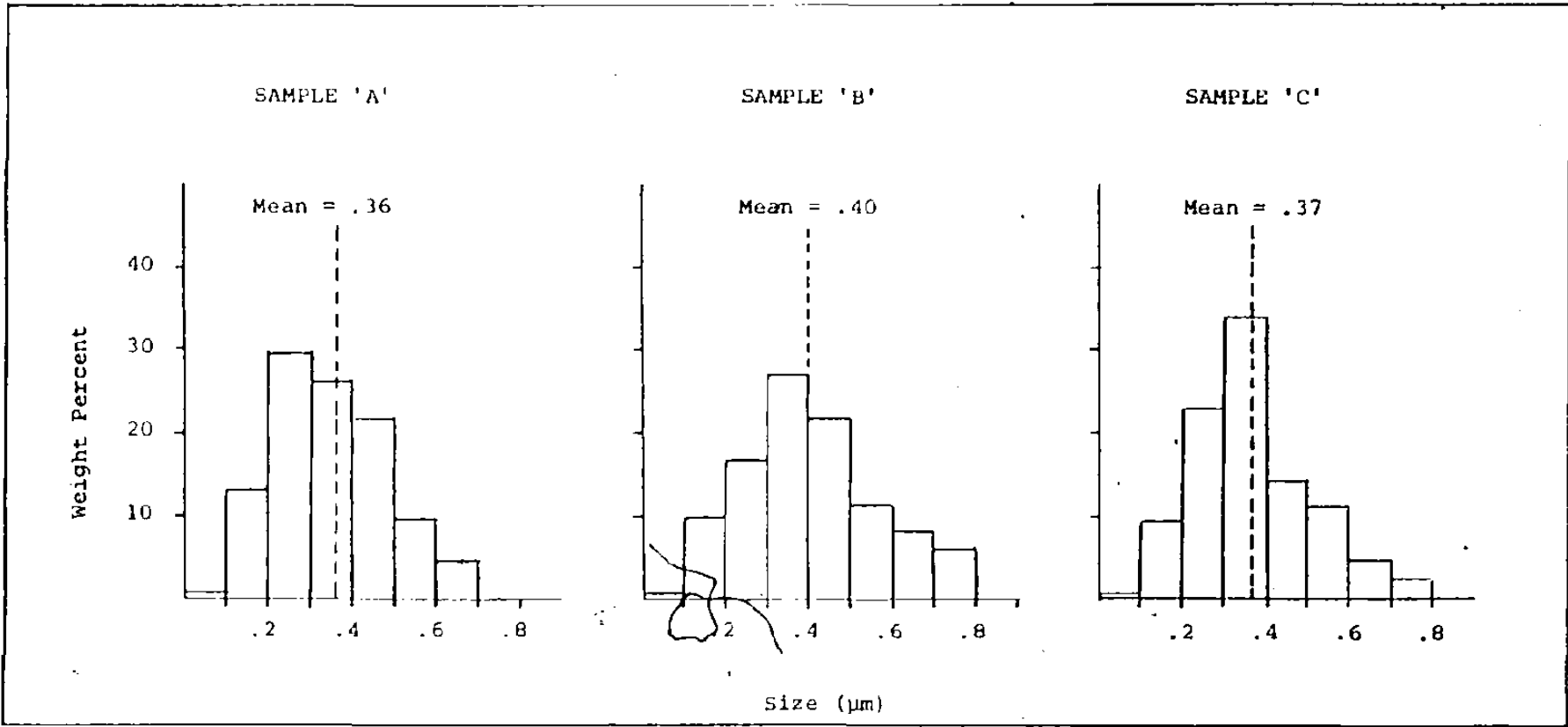


Fig. 57: Reproducibility of Size Analysis - 12 Minute Fume Sample

TABLE XXI  
REPRODUCIBILITY OF SIZE ANALYSIS  
(12 Minute Fume Sample)

Sample	Mean Particle Size (μm)	% Difference From Average*
A	.36	- 4.51
B	.37	- 1.86
C	.40	+ 6.10
Average	.377	

\*  $\frac{\text{Value}-\text{Average}}{\text{Average}} \times 100\%$

#### 4.7.2 Size Analysis Results

Size distributions were determined for the fume material from each time period sampled (1, 5, 8, 12, 15, 20 minutes and reblow). A sample of "pre-ignition" fume was also sized.

The "pre-ignition" sample was taken from one particular heat where ignition did not take place until after the two minute mark of the blow. Ignition usually occurs within the first 15 seconds of the blow.. Since this one minute sample represented a unique part of the refining process, it was sized separately from the other one minute samples. The weight of this sample, at .7 g, was well below the average of 4.8 for the other one minute samples (Table XII).

The individual frequency and weight percent data and distributions for the above-mentioned samples are listed in Appendix D (the 12 minute sample data are in Appendix C).

The weight percent distributions for the fume samples taken during the decarburization period (1, 5, 8, 12, 15, 20 minutes) are shown together in Figure 58. It can be seen that they are similar in shape and that the difference in mean particle size is within the reproducibility of the sizing method. The smallest particles observed in any of these samples were approxi-

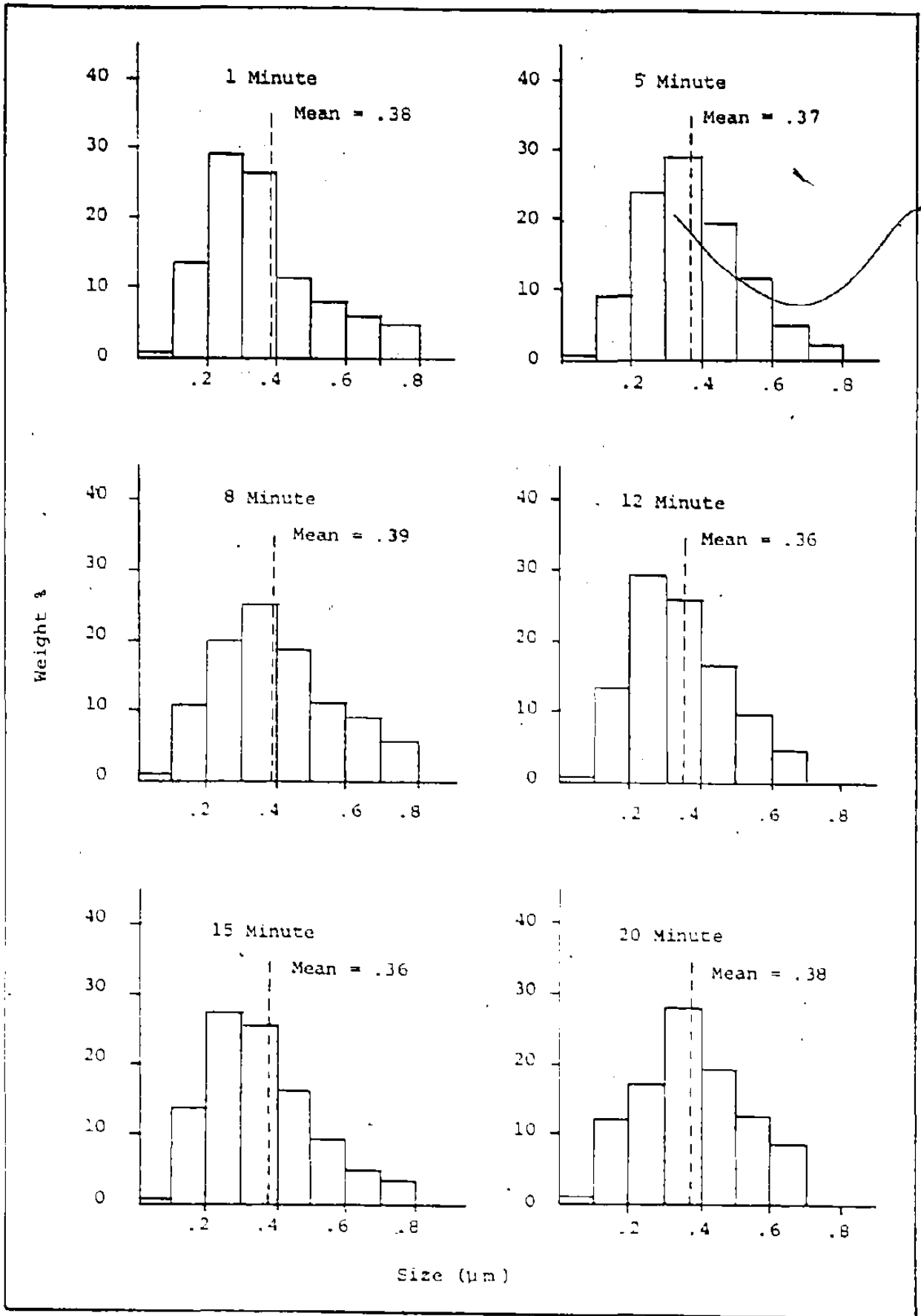


Fig. 58: Comparison of Fume Size Distributions at Various Blowing Times

mately  $.03 \mu\text{m}$ , while the largest was about  $1 \mu\text{m}$ . The majority, 99.5% of the particles, were less than  $.8 \mu\text{m}$  in diameter. The mean diameter (based on the weight percent distribution) ranges from  $.36$  to  $.39 \mu\text{m}$ .

The size distributions of the "pre-ignition" and reblow fume samples are similar to each other but different from the decarburization period fume. For these two samples, 99.5% of the particles were less than  $.5 \mu\text{m}$  in diameter and the smallest were again about  $.03 \mu\text{m}$  in size. The mean particle size was approximately  $.2 \mu\text{m}$ . The contrast between the size distributions of these two samples and a typical decarburization period sample is shown in Figure 59.

The results of the fume size analysis are summarized in Table XXII. The weight percent less than  $.2 \mu\text{m}$  is included as this is the upper limit for the size of vapourization fume<sup>25</sup>.

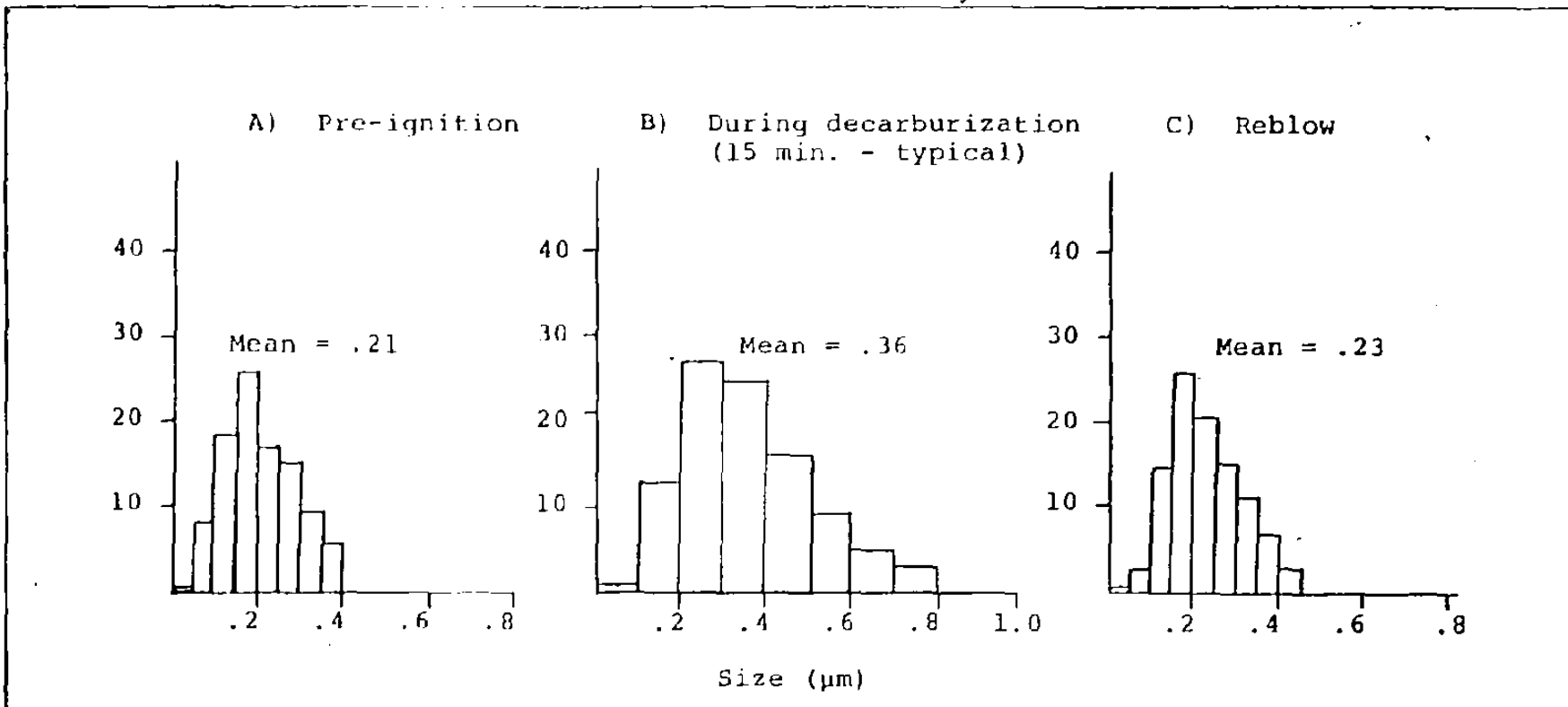


Fig. 59: Size Comparison of Pre-Ignition, Decarburization and Reblow Fume

TABLE XXII  
SUMMARY OF SIZE DISTRIBUTION

Time	Mean Particle Size ( $\mu\text{m}$ )	Weight % Less Than .2 $\mu\text{m}$	95 Weight % Less Than (Approx.) ( $\mu\text{m}$ )
Pre-Ignition	.21	52.80	.35
1	.38	13.98	.70
5	.37	9.25	.60
8	.39	11.07	.70
12	.36	13.54	.60
15	.38	13.86	.70
20	.38	12.38	.60
Reblow	.23	43.23	.40



#### 4.8 Relation Between Fume and Metallic Ejections

##### 4.8.1 Fume and Slopping

Slopping is best described as a sudden and uncontrollable ejection of metal and slag from the furnace. It indicates that the decarburization process is not uniform as large quantities of CO gas are generated intermittently. All of the possible explanations for the occurrence of slopping will not be discussed here except to say that the overcharged condition of Dofasco's furnaces contributes heartily to both the frequency and severity of slopping. The work-volume of the B.O.F. studied in this work is  $.55 \text{ m}^3 \cdot \text{t}^{-1}$  compared to its designed value of  $.8 \text{ m}^3 \cdot \text{t}^{-1}$ .

It has already been demonstrated that the type of scrap used has an influence on the quantity of fume evolved; therefore, to study the effect of slopping on fume evolution, it is necessary to fix the scrap quality. During the study of the "C" scrap type heats, it was visually observed that slopping occurred at the 15 minute mark in half of these heats.

According to the visual observations, these 15 minute fume samples were separated into "slopping" and "non-slopping" categories. The fume weights for these two groups are compared in Table XXIII. On average, fume evolution at the 15 minute mark of these heats was approximately 44% higher when the furnace was slopping.

TABLE XXIII  
FUME WEIGHT AT 15 MINUTES  
 ("C" Type Scrap)

No.	Fume Weight (g) At 15 Minutes	
	Not Slopping	Slopping
1	.66	1.19
2	.76	.93
3	.80	1.33
4	.76	1.36
5	.88	1.58
6	1.09	1.61
7	1.15	1.19
8	.56	.88
9	.56	.61
10	.90	1.02
11	.61	.93
12	.88	1.09
13		1.28
Average	.80	1.15
$\frac{\text{Avg. (Slop-Not Slop)}}{\text{Avg. Not Slop.}} \times 100\%$		43.8%

The individual fume samples were then combined according to category to give two bulk samples for size analysis. Sample preparation and particle size counting were identical to that described in Section 4.6. The individual frequency and weight percent distributions for these two samples are listed in Appendix E.

The two weight percent distributions are compared in Figure 60. The distributions are similar to any of the other decarburization period results as shown in Figure 58.

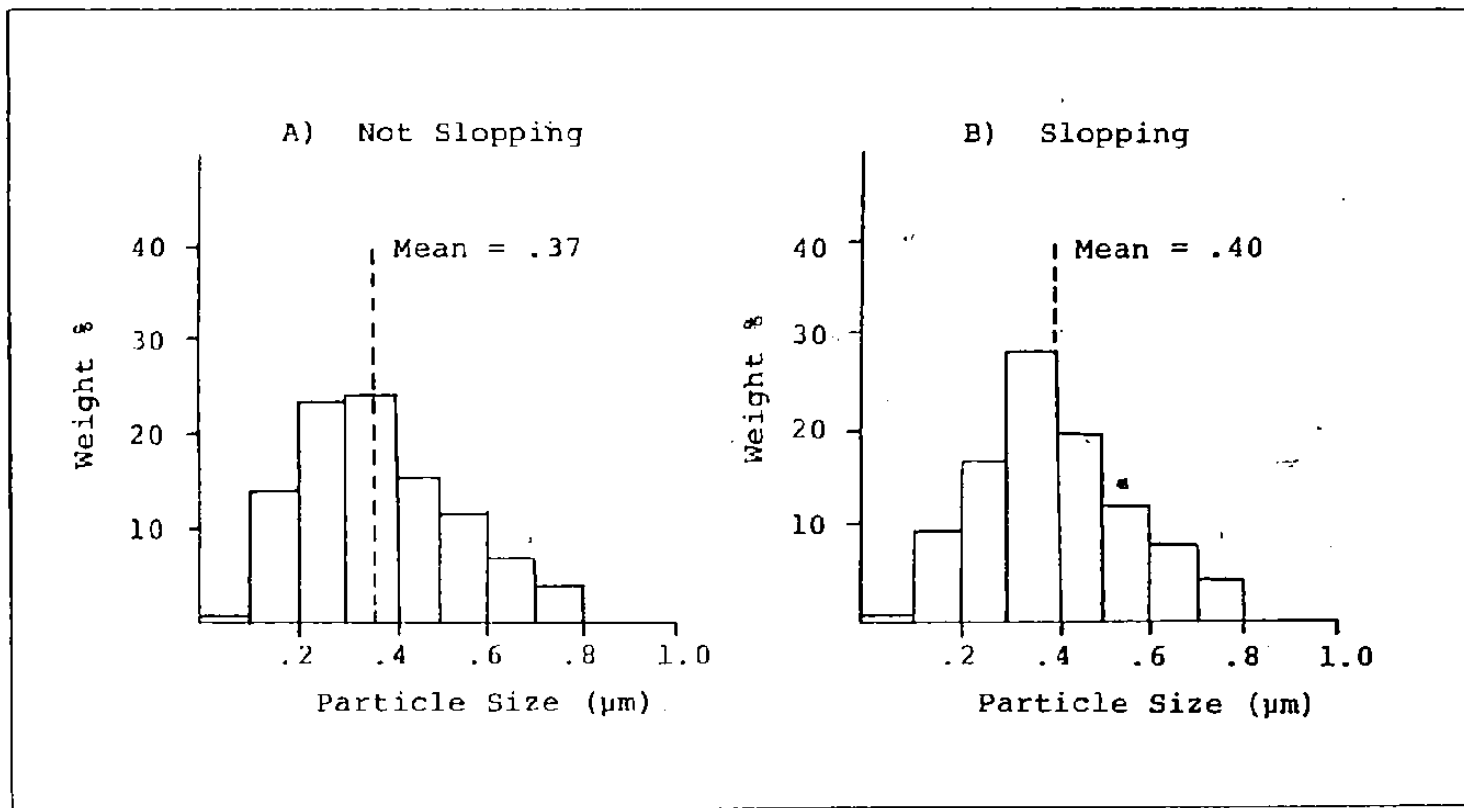


Fig. 60: Comparison of Slopping and Not Slopping 15 Minute Fume

#### 4.8.2 Fume and Metallic Ejections

A device to measure the total quantity of iron lost from the B.O.F. in the form of metallic ejections and slop has been developed at Dofasco. The device and measuring technique are discussed in detail elsewhere<sup>24</sup>. The basic procedure is to suspend a tube sampler (square in cross-section) above the mouth of the furnace. The slop and ejected material that adheres to the device is then weighed and analyzed to determine the amount of iron collected.

During the study of the "B" scrap type heats, the total iron losses in the form of metallic ejections and slop were also measured. This iron loss (kg of iron per heat) is listed along with the corresponding average fume weight in Table XXIV. The average fume weight per heat is the average of the sample weight at the 1, 5, 8, 12, 15 and 20 minute mark.

A linear least squares regression analysis was performed on this data to determine if a relationship between fume weight and metallic ejections existed. The calculated regression equation and the data are plotted in Figure 61. The correlation coefficient ( $r$ ) and the  $T^2$  values are statistically significant.

The fume weight increases with increasing metallic ejections.

TABLE XXIV  
AVERAGE FUME WEIGHT AND  
IRON IN METALLIC EJECTIONS

No.	Average Fume Weight (g)	Iron in Ejections (kg)
1	1.76	522
2	2.12	694
3	2.18	3188
4	2.59	1436
5	1.45	308
6	2.04	1861
7	1.74	173
8	2.06	544
9	2.26	3765
10	2.98	4081
11	2.57	4843
12	2.83	1735
13	3.20	4371
14	2.94	3481
15	2.38	4692
16	1.66	2056
17	2.53	1355
18	3.31	4255
19	2.89	2912
20	1.24	1924
21	1.49	1012
22	1.80	2544
23	1.81	1340
24	1.08	530
25	1.95	2533
Mean	2.19	2246.2
St. Dev.	.74	1494.4
Level of Significance	60%	70%

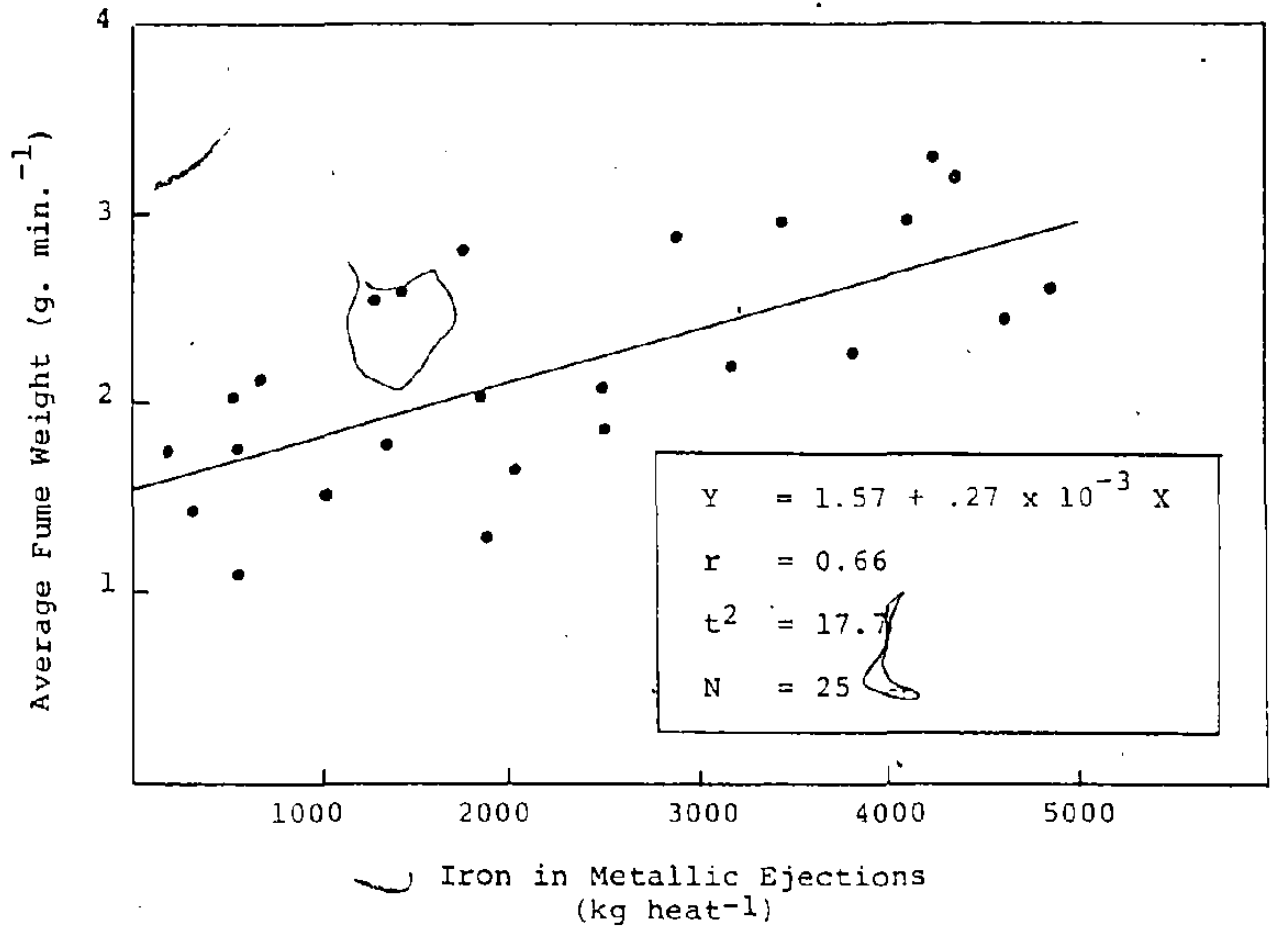


Fig. 61: Fume Weight Vs. Metallic Ejections

## 5. DISCUSSION

### 5.1 Quantity and Chemical Analysis of Fume

The fume weights measured in this study were not an absolute measure of the total quantity of fume emitted during B.O.F. steelmaking; they were relative on proportional values. No attempt was made to scale up the measured fume weight ( $\text{g. min.}^{-1}$ ) to the actual fume losses ( $\text{kg min.}^{-1}$ ). However, it is possible to determine an overall fume loss on the basis of the material which is processed through the cleaning<sup>y</sup> system thickeners.

This material, known as B.O.F. sludge, is the combination of both the spark box and venturi discharges. It amounts to approximately 2800 kg per heat or 117 kg  $\text{min.}^{-1}$  of blowing time. At approximately 50% total iron, this represents a yield loss of 1%. This value is within the range of .7 to 2% reported for other B.O.F. installations<sup>1-4</sup>.

The major chemical components of the fume material are  $\text{Fe}_2\text{O}_3$  (58.4%),  $\text{FeO}$  (11.48%),  $\text{CaO}$  (8.23%) and  $\text{MgO}$  (3.11%). The total iron content is approximately 50% while the metallic iron content is only .4% (See Table XIV).



The metallic iron fraction amounts to less than 1% of the total iron in the fume and is most likely the result of small metallic ejection particles being present in the sample. Fume is classified as particles less than 5  $\mu\text{m}$  in diameter, while particles ranging up to .1 mm were sometimes found in the samples collected. These larger particles are metallic ejections. They have been observed to have a metallic iron core that is covered with an iron oxide layer from 10 to 20  $\mu\text{m}$  in thickness<sup>24</sup>.

The total Fe, CaO and MgO contents vary with the blowing time, the flux components being the highest (and total Fe lowest) during the period of flux additions to the furnace (See Figure 43). The fluxes are added continuously from the 30 second mark to the 8 minute mark of the blow. The high concentration of MgO and CaO in the fume material is the result of fine flux particles being entrained in the furnace off-gases.

After the fluxes are added and start to dissolve in the slag (after the 10 minute mark), the chemical analysis of the fume is relatively constant at 55 to 60% total iron and 4 to 6% CaO + MgO.

The ratio of  $\text{Fe}_2\text{O}_3/\text{FeO}$  in the fume ranged from 3.3 to 6.6 (See Table XIV). This indicates that these particles have been highly oxidized. In comparison, the

$\text{Fe}_2\text{O}_3/\text{FeO}$  ratio in the slag only ranges from .2 to .7 during the course of the blow.

The ratio of Mn/Fe in the fume to that in the metal ranged from 2.19 to 17.20 and averaged 9.8 (See Table XVII). The ratio was lowest at the beginning of the blow, relatively constant during the 5 to 15 minute mark, and highest at the 20 minute mark (See Figure 45). The significance of these results will be discussed later in Section 5.3.

The chemical analysis results are similar to those of Krichevtsov<sup>3</sup> (See Table VI) who studied another industrial B.O.F. with an open hood gas collection system. In the case of Krichevtsov, the flux was added in five batches rather than continuously, and there are peaks in the CaO analysis during each addition. The overall ratio of  $\text{Fe}_2\text{O}_3/\text{FeO}$  was about 8 and the ratio of Mn/Fe in the fume to that in the metal was approximately 15.

## 5.2 Fume and Metallic Ejections

The fume rate ( $\text{g Fe min}^{-1}$ ) decreases rapidly during the first eight minutes ( $1/3$ ) of the blowing time, after which the decrease is more gradual as seen in Fig. 44. Approximately 60% of the total iron lost as fume is lost during this first eight-minute period. These results are similar to those of Krichevtsov<sup>3</sup> shown in Fig. 22 (broken line - no inblow ore additions).

The decrease in fume rate with increasing blowing time can be related to four factors, all of which influence the quantity or size of metal spray produced by the impact of the oxygen jet. In ascending order of importance, these factors are:

- i) lance practice
- ii) bath temperature
- iii) slag volume
- iv) carbon content of metal bath

### i) Lance Practice

The distance the oxygen jet penetrates the metal bath was calculated for a typical Dofasco heat in Table V. During the first one to three minutes of the blow, the mode of jet-melt interaction changes from one of splashing to one of penetration. During the splashing mode,

a large number of fine metal droplets are thrown outwards away from the area of jet impact. During the penetration mode, the metal droplets produced are larger in size and fewer in number. There is a distinct decrease in the fume rate when changing from the splashing to penetrating modes as observed in the hot model studies of Peregudov (Fig. 19).

The lance height also influences the bath velocity. Lower lance heights increase the jet impact force (for a fixed blowing rate), and this will result in higher bath velocities. Water model studies by Li<sup>55</sup> have shown that increased bath velocities decrease the number and increase the size of spray droplets created by the jet impact (Fig. 17).

#### ii) Bath Temperature

As mentioned above for fixed blowing conditions, increasing the bath velocity will result in a decrease in the amount of metal spray. In a B.O.F., one factor that can influence the bath velocity is the bath temperature, as lower temperatures result in higher metal viscosity<sup>65-68</sup>. Yakovlev<sup>64</sup> observed that lower bath temperatures resulted in higher fume losses in an industrial B.O.F. (Fig. 21).

The above effect was also observed in this study. The fume rate ( $\text{g}\cdot\text{min}^{-1}$ ) was observed to increase with increasing scrap iron oxide content (Fig. 48). Higher

scrap iron oxide contents were also observed to result in lower bath temperatures (Fig. 49). The lower temperatures are related to the high heat consumption of the iron oxide, approximately six times (per iron unit) that of pure iron.

As well as influencing the metal viscosity, lower metal temperatures will also result in lower slag temperatures and, therefore, higher slag viscosities. This will hinder the formation of a foamy slag that will physically entrap some part of the metal spray being generated inside the furnace.

### iii) Slag Cover

The fume rate was observed to decrease with increasing slag weight as seen in Fig. 47. A thick slag cover will reduce the fume rate by physically entrapping some of the metal spray that would otherwise be oxidized to fume.

A regression analysis of the average fume weight ( $\text{g. min.}^{-1}$ ) and the total weight of metallic ejections ( $\text{kg. heat}^{-1}$ ) showed a significant relationship (Fig. 61). The fume rate increases with increasing weight of metallic ejections. The ejections are collected at the furnace mouth and, therefore, are an indirect measure of the height the metal spray reaches. These results are in agreement with those of Okhotskii<sup>75</sup> who

also noted an increase in fume rate with increasing height of metal splash (Fig. 28).

For the same period of the blow (15 minute mark), it was observed that the fume rate, when slopping occurred, was approximately 44% higher than that during normal refining (See Table XXIII). This is evidence that the slag properties are more important than the actual weight of slag present. At Dofasco slopping is characterized by low iron oxide and high silica levels in the slag. This type of slag is very viscous and dry and has poor lime dissolution capabilities<sup>89,90</sup>. It has a tendency to coagulate and is readily pushed towards the furnace walls by the force of the oxygen jet. This condition is generally referred to as "slagless" blowing since the jet acts directly on the metal bath. Under these conditions, the slag is less capable of entrapping metal spray; the result is an increase in fume evolution.

Okhotskii<sup>75</sup> also observed that for a fixed bath carbon content, the fume rate increased during "slagless" blowing as seen in his results in Fig. 27.

#### iv) Carbon Content of Metal Bath

The fume rate ( $\text{g Fe} \cdot \text{min.}^{-1}$ ) decreases rapidly until the bath carbon is about 2%, after which the decrease is gradual (See Fig. 46). Similar results have

been recorded in both laboratory experiments<sup>10,22,34,38,39</sup> (Fig. 10) and other industrial B.O.F. studies<sup>1,2,64,75</sup> (Fig. 24).

Carbon influences the fume rate in three ways:

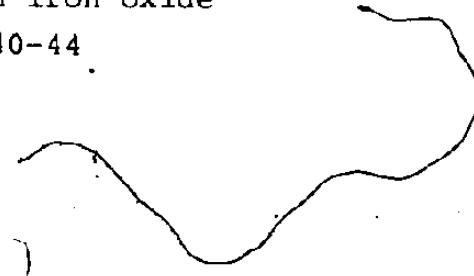
- the bath carbon content affects the number and size of metal spray droplets produced by the bursting of CO bubbles.
- as a result of violent decarburization, metal droplets explode into many smaller particles which are then oxidized to fume.
- the melt decarburization rate controls the residence time of the metal droplets in the oxidizing atmosphere of the jet impact zone.

The significant contribution of the early decarburization reaction to the quantity of metal spray produced is evident in the difference between the pre-ignition and regular one minute fume sample weights. The pre-ignition sample weighed only .7 g, while the other one minute samples ranged from 2 to 7.5 g (avg. 4.8, Table XII).

In laboratory experiments, Morris<sup>22</sup> noted that the size of metal spray produced during decarburization increased in size with decreasing bath carbon content. At high carbon levels (4%), the metal spray was all less than 75  $\mu\text{m}$  in diameter. At lower carbon contents

(< 2% C), the number of spray droplets decreased while their size increased; the majority were in excess of 250  $\mu\text{m}$ . This was then related to the location of the decarburization reaction and the size of the CO bubbles generated (as discussed in Section 2.3.2). The smaller droplets produced at the high melt carbon levels would have a higher probability of decarburizing explosively to fume as a result of their larger surface to volume ratio, thus contributing to the higher fume rates during the first third of the blow.

In hot metal studies<sup>62</sup>, droplets .5-1 mm in diameter were observed to break away from the ridge of the jet impact crater. These Fe-C droplets are oxidized to fume (the majority being less than 1  $\mu\text{m}$  in size) by a mechanism of explosive decarburization, as shown in Fig. 12. At some critical carbon content, the decarburization mechanism of these droplets changes from a quiet surface reaction to a violent CO boil. With further decrease in carbon content, the reaction becomes explosive and the droplet shatters into many smaller fragments that are oxidized to fume (Fig. 12d). The transition from surface to internal decarburization has been observed to occur only after an iron oxide layer has formed on the droplet surface<sup>40-44</sup>.





Metallic ejections collected at the mouth of the furnace were observed to consist of iron droplets 20  $\mu\text{m}$  to 1 mm in diameter. These particles were coated with a layer of iron oxide 5 to 15  $\mu\text{m}$  thick and had carbon contents up to .6% C<sup>24</sup>. At 1500°C in an oxygen atmosphere, these particles should be in the internal decarburization mode as shown in Fig. 12c. With sufficient time, temperature and oxygen supply, these particles would explode and be oxidized to fume. Insufficient residence time inside the furnace is the most likely reason that these ejections were not completely transformed into fume.

Although the carbon content of the metal does not affect the residence time of the metal droplets inside the furnace, the decarburization rate does. The off-gas velocity is directly proportional to the decarburization rate which varies with blowing time as seen in Fig. 62.

Using a calculation similar to that in Appendix A, it is possible to determine the maximum metal droplet size that can be carried out of the furnace by the off-gases. This calculation was done for Dofasco's furnaces by Laciak<sup>24</sup>, and his results are shown in Fig. 63. The maximum droplet diameter increases with increasing decarburization rate (increasing off-gas velocity).

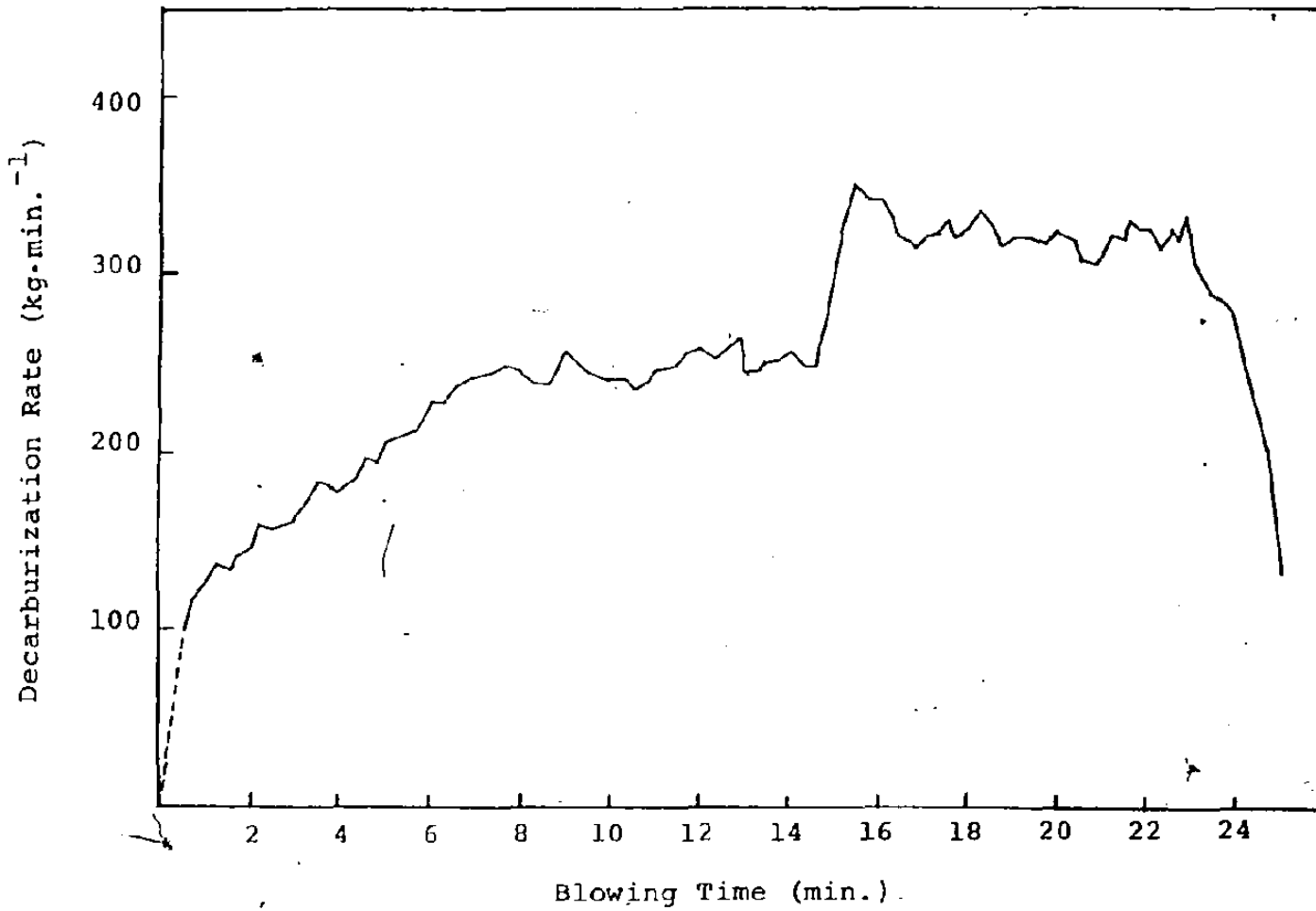


Fig. 62: Decarburization rate versus blowing time  
(Dofasco)

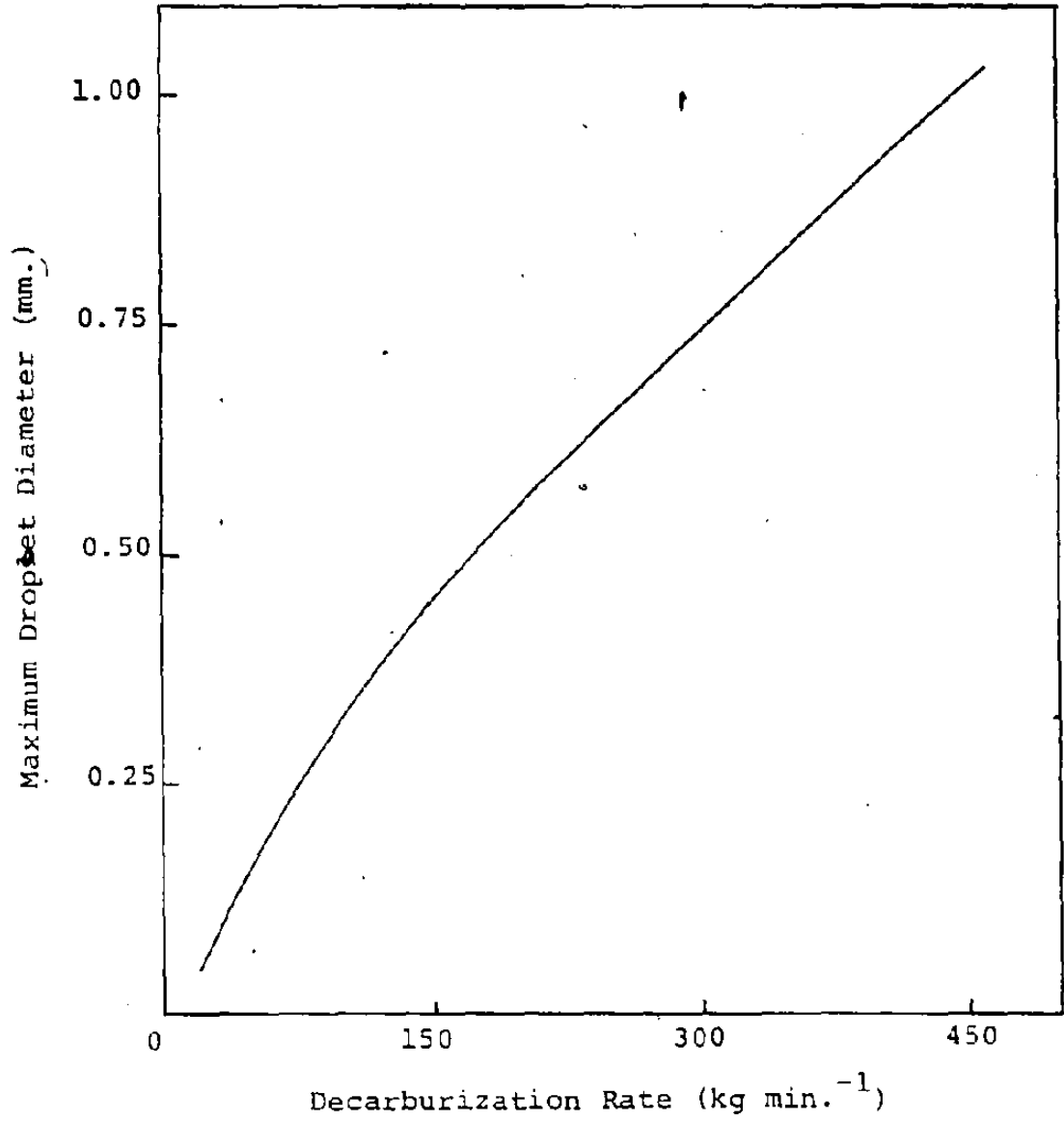


Fig. 63: Plot of the maximum size metal droplet that can be entrained in the off-gas stream (Dofasco) [24]

The metallic ejection and fume rates are plotted together versus blowing time in Fig. 64. The metallic ejection curve is from the work of Laciak<sup>24</sup> (same Dofasco furnace as this study). Although the ejection rate is an absolute measurement while the fume rate is a relative one, the comparison is appropriate because the total ejection and total fume weights are in the same range (1 to 1.5% of the furnace charge weight). The shape of the fume and ejection weight curves in Fig. 64 can be explained by the increase in metal spray size and off-gas velocity with increasing blowing time.

At the beginning of the blow, the conditions of a high lance, low bath velocity, low bath temperature, and high metal carbon content all result in a large quantity of fine metal spray being generated by the oxygen jet impact and bursting of CO bubbles. During this period, the slag volume is small and unable to entrap much of this spray. Due to the low decarburization rates ( $< .1\% \text{ C.min.}^{-1}$ ), the low off-gas velocities would cause larger droplets to fall quickly back into the melt while increasing the residence time of the smaller particles in the oxidizing region below the lance. This combination of small droplet size and long residence time would increase the chances of explosive decarburization and oxidation to fume. In fact, as seen in Fig. 64, the fume rate is high and the ejection rate is low during the first third of the blow.

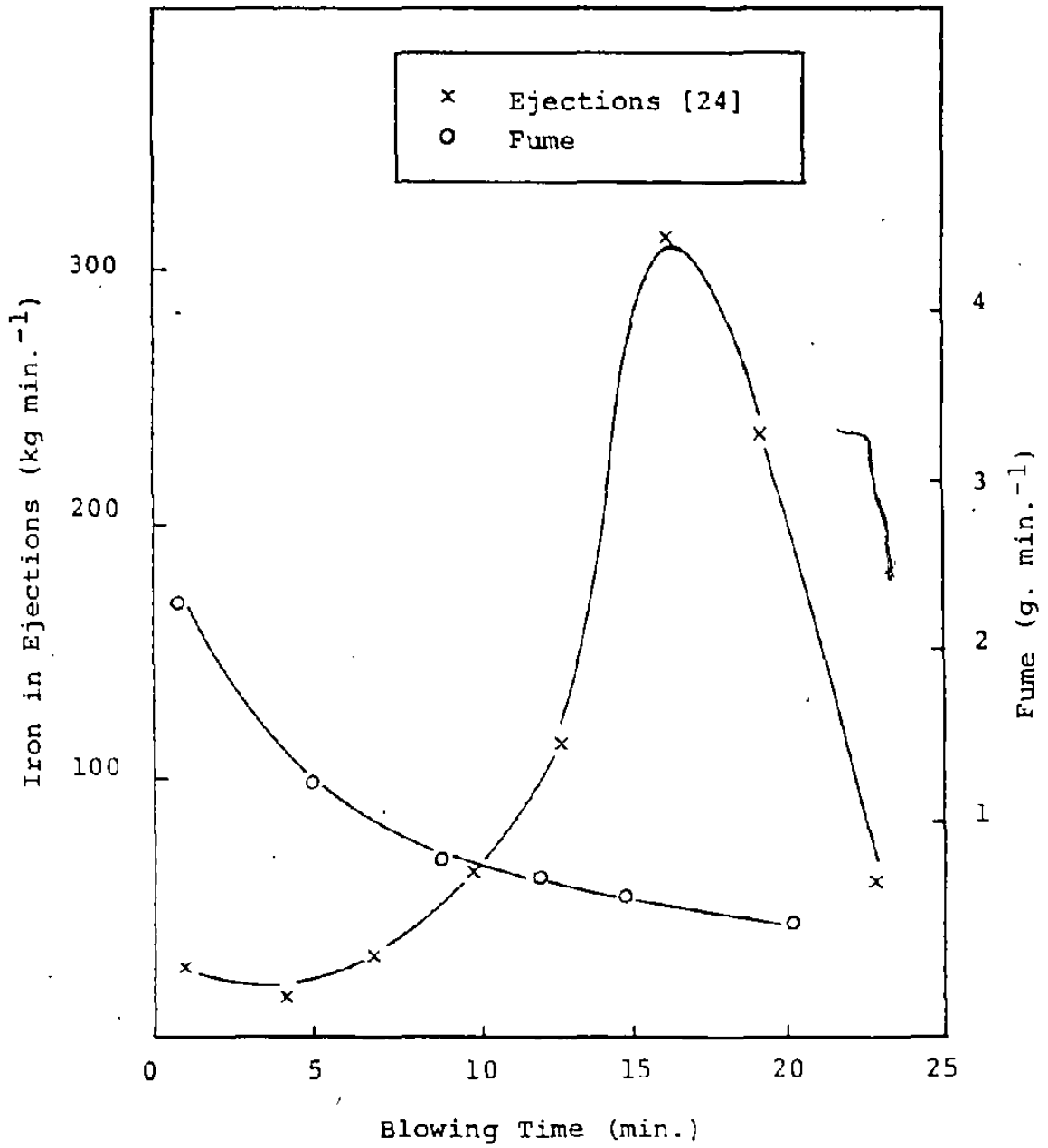


Fig. 64: Fume and ejection rates versus blowing time

With increasing blowing time, the quantity of spray produced decreases in number but increases in size. This is a result of the lower lance, increased bath temperature and velocity and decreased melt carbon content. The slag volume has also increased and is capable of entrapping a larger part of the metal spray. At the same time, the higher off-gas velocities (decarb. rates in the order of .15 to .25% C min.<sup>-1</sup>) decrease the residence time of the metal droplets in the furnace. Although the off-gases can now support larger particles, their shorter residence time and smaller surface to volume ratio may not allow sufficient time for explosive decarburization and oxidation of the total droplet to occur. This could lead to the decrease in fume rate and increase in ejection rate that is seen in Fig. 64.

The oxidation of metal droplets to fume could occur either internally in the lance impact zone or externally in the furnace hood.

Samples of gas taken from 1.2 m inside the mouth of a Dofasco B.O.F. contained less than 1% oxygen<sup>91</sup>. At the same time, fume material collected from the filters of the gas sampling probe contained about 80% iron oxide and less than 1% metallic iron. These results indicate internal fume formation in the oxygen jet impact zone.

It is also possible that a small part of the fume is generated in the furnace hood where large quantities of atmospheric air are present. During the first five minutes of the blow, when the fume evolution is highest, the gas temperature in the hood is less than  $500^{\circ}\text{C}$ <sup>91</sup>. At this temperature, it is unlikely that decarburization would occur to any large extent. External fume generation would be possible only during the 15 to 20 minute period of the blow (peak decarburization) when gas temperatures in the hood reach  $1500^{\circ}\text{C}$ <sup>91</sup>. From the fume measurements (Fig. 44), only about 15% of the total iron weight in the fume is lost during this period.

In summary, fume formation in the B.O.F. has been related to the oxidation of metal spray that is generated by the action of the oxygen jet and CO bubbles. The decrease in fume weight with blowing time is a result of the increasing size and decreasing residence time of these metal droplets in the oxidizing atmosphere of the lance impact zone. Factors such as bath carbon, slag volume, metal temperature and lance practice influence the fume rate by their effect on either the size or number of metal droplets being generated.

Although the majority of the fume particles were spherical in shape (indicating droplet oxidation), some

polygonal particles were also observed as seen in Fig. 53 to 55. The presence of these polygonal particles is proof that vapourization is also occurring. In the next section, the relative contribution of vapourization to the overall fume losses will be determined.

7

2



### 5.3 - Quantity of Vapourization Fume

The quantity of vapourization fume can be determined from the size, shape and chemical analysis of the fume particles.

Fume particles that are formed by condensation from the vapour phase are polygonal in shape<sup>22,25,27</sup> (See Fig. 8). This is due to the crystal structure of the iron oxides; the structure of  $\text{Fe}_2\text{O}_3$  is rhombohedral, while that of  $\text{Fe}_3\text{O}_4$  is octagonal. Vapourization fume is also very fine, the smallest particles being about .02  $\mu\text{m}$  with the majority being less than .2  $\mu\text{m}$  in diameter<sup>25,37</sup>.

Fume particles that are formed as a result of metal spray oxidation are spherical in shape<sup>22,25,40-45</sup>. This type of fume also exists over a larger size range, the smallest being about .03  $\mu\text{m}$ , with the majority being less than 1  $\mu\text{m}$  in diameter<sup>14,25,42,70-72</sup>.

Vapourization fume could be generated in two possible ways. The first is by direct vapourization of the metal bath in the "hot spot" zone. The second is through vapourization of part of the metal spray as a result of oxidation or chemical reaction. Kosmider<sup>26</sup> calculated that during oxidation of iron with pure oxygen, local interfacial temperature could reach 3000°C. With such high local temperatures, vapourization of part of the droplet itself might occur.

From the TEM photographs of the fume material (Fig. 53 to 55), it is apparent that the particles are the result of both vapourization and metal droplet oxidation. Since it was not practical to count the fraction of polygonal particles in each fume sample, the extent of vapourization fume will be based on the Mn/Fe ratios and the fraction of particles less than .2  $\mu\text{m}$  in diameter.

The ratio of Mn/Fe in the fume to that in the metal bath can be used to determine the amount of fume caused by direct vapourization of the metal bath. Since at a given temperature, Mn is more volatile than Fe (Fig. 7) under direct vapourization, the proportion of Mn should be higher in the fume than in the melt. From the work of Bogdandy and Pantke<sup>27</sup> (Fig. 9), it is possible to predict the Mn/Fe ratio for the case of direct vapourization.

If a metal droplet is vapourized, the fume produced will have the same Mn content as the original droplet. Therefore, the fraction of particles less than .2  $\mu\text{m}$  in diameter can be used as an estimate of the total amount of vapourization fume (both direct and from metal droplets). However, the .2  $\mu\text{m}$  limit is not an absolute estimate because not all the particles less than .2  $\mu\text{m}$  are polygonal as seen in Fig. 55. If vapourization of metal droplets is occurring, the quantity of vapourization fume predicted by the .2  $\mu\text{m}$  size limit should be much higher than that predicted by the Mn/Fe ratio.

1) Fume from the Decarburization Period

The size distributions of the decarburization period fume samples (1,5,8,12,15, 20 minutes) can be considered as constant within the reproducibility of the size analysis method. The mean particle size and weight % less than .2  $\mu\text{m}$  in diameter averaged .38  $\mu\text{m}$  and 12.34 weight % respectively.

The measured Mn/Fe ratios are compared to those for 100% direct vapourization in Table XXV. The values for 100% direct vapourization were determined using the chemical analysis of the melt (Table XVII) and the results of Bogdandy and Pantke<sup>27</sup> (Fig. 9). For example, at the eight minute mark, the ratio of Mn/Fe in the metal bath is  $.113 \times 10^{-2}$  (Table XVII). From the work of Bogdandy in Fig. 9, for 100% direct vapourization, the Mn/Fe ratio in the fume would be  $15.9 \times 10^{-2}$ , giving an overall ratio (fume/melt) of 141 ( $15.9 \div .113$ ). The actual measured value at the eight minute mark was 10.0 indicating that about 7.1% ( $10 \div 141 \times 100\%$ ) of the fume was caused by direct vapourization at that time (See Table XXV).

The measured Mn/Fe (fume/melt) ratios are lower at the beginning of the decarburization period, relatively constant during the 5 to 15 minute mark and increase towards the end (See Fig. 45). This variation is most

likely due to the presence of slag particles in the fume samples and not the result of any change in the relative contribution of direct vapourization during this period.

The weight of slag particles in the fume material should increase with increasing off-gas velocity as higher velocities can support larger particles. If this is so, a plot of decarburization rate (directly proportional to off-gas velocity) versus blowing time should resemble the curve for the Mn/Fe ratio. In fact, this is the case as seen in Fig. 65. Therefore, a more accurate estimate of the amount of direct vapourization during the decarburization period is 1.75% (by weight), the value corresponding to the one minute fume sample (Table XXV). At the one minute mark, the decarburization rate is low ( $\approx 100 \text{ kg C min.}^{-1}$ ) and the amount of slag entrained by the off-gases should be at its lowest.

The amount of vapourization fume during the decarburization period can, therefore, be estimated as being between 1.8% by weight, based on the Mn/Fe ratio, and 12.3%, based on the .2  $\mu\text{m}$  size limit. The large difference between the two values, approximately six times, is evidence that both direct melt and metal droplet vapourization are occurring. Since the exact fraction

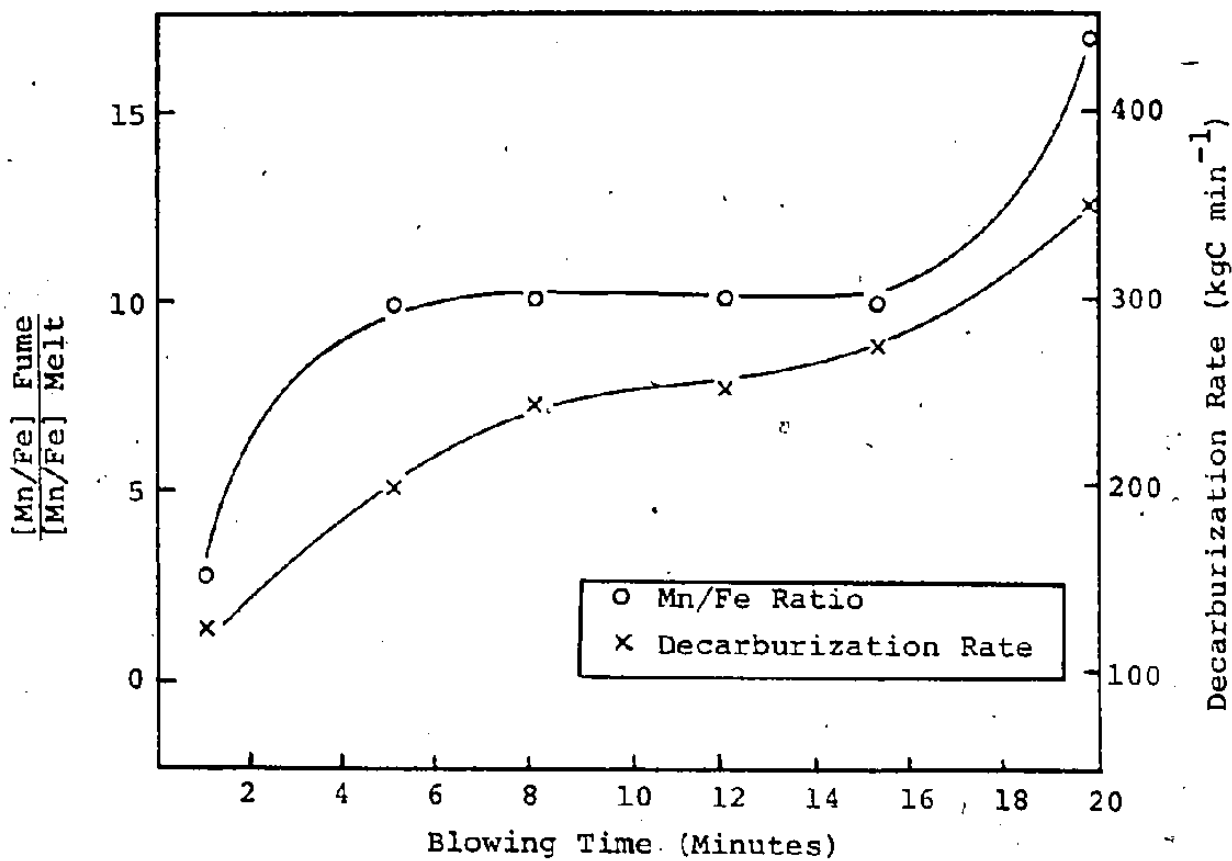


Fig. 65: Mn/Fe Ratio and Decarburization Rate at Various Blowing Times

of polygonal particles is unknown, it is not possible to estimate the relative contributions of direct and metal droplet vapourization.

ii) Pre-ignition and Reblow Samples

The pre-ignition and reblow fume were observed to have similar size distributions. Both samples had a mean particle size of approximately  $.2 \mu\text{m}$  and ranged from  $.02$  to  $.45 \mu\text{m}$ . The weight percent less than  $.2 \mu\text{m}$  was 52.8% for the pre-ignition and 42.2% for the reblow sample. This material is considerably smaller than the decarburization fume (mean size  $.38 \mu\text{m}$ , range  $.03$  to  $.8 \mu\text{m}$ ) as seen in Fig. 59. These size analyses results suggest that the degree of vapourization is higher during these two periods than during the decarburization period.

During the pre-ignition and reblow periods, the decarburization rate is less than that during the one minute mark of the blow; therefore, any contamination of the fume material by slag particles should be minimal. The Mn/Fe ratio for the reblow fume sample was 15.2 compared to 2.2 for the one minute fume sample (decarburization period). This again suggests a higher degree of vapourization during the reblow period. Using the metal bath and fume analyses in Table XVII and the results of Bogdandy<sup>27</sup> in Fig. 9, for pure vapourization of the reblow melt, the Mn/Fe ratio (fume/melt) would

be 143. Therefore, the percent contribution of direct vapourization during a reblow is about 10.6% ( $15.2 \div 143 \times 100\%$ ). Unfortunately, the pre-ignition sample was too small for both chemical and size analyses so its Mn/Fe ratio is unknown. However, it is expected that it would be in the same range as that of the reblow sample.

The refining conditions during the pre-ignition and reblow periods are similar and differ from those of the decarburization period in terms of metal bath velocity and decarburization rate. During both pre-ignition and reblows, the bath is initially stagnant and the decarburization rate is less than  $50 \text{ kg C. min}^{-1}$ . During these periods, the oxidation of iron is the major reaction taking place. This should result in higher hot spot temperatures since little of the reaction heat is leaving the system as sensible heat in gaseous reaction products, and the transfer of this heat to the bulk metal is hindered by very low bath velocities. Therefore, a higher degree of vapourization is expected in comparison to the decarburization period.

The degree of vapourization during pre-ignition and reblows can be estimated as being between 10.6% (by weight) based on the Mn/Fe ratio, and approximately 50%, based on the  $.2 \mu\text{m}$  size limit. This is significantly higher than

the 1.8% (Mn/Fe ratio) to 12.3% (.2  $\mu\text{m}$  limit) for the decarburization period fume. Therefore, it can be concluded that direct vapourization during the reblow and pre-ignition periods is about five times larger than that during the decarburization period of the blow. However, the major mechanism of fume formation remains that of droplet explosion and oxidation.



TABLE XXV

Mn/Fe Ratio and Weight % < .2 μm for Decarburization Period Fume

Blowing Time (min.)	Mean Particle Size (μm)	Mn/Fe Fume / Mn/Fe Melt			Weight % < 0.2 μm
		(A) Test Results*	(B) Ratio for Vapourization only from Bogdandy [27]	(A) / (B) x 100%	
1	.38	2.19	125	1.75	13.98
5	.37	9.68	142	6.82	9.25
8	.39	10.00	141	7.09	11.07
12	.36	10.08	144	7.00	13.54
15	.38	9.42	145	6.49	13.86
20	.38	17.20	162	10.61	12.38
Average	.38			6.63	12.34

\* From Table XVII

## 6. CONCLUSIONS

1. There are two mechanisms of fume formation occurring during B.O.F. steelmaking:
  - i) Oxidation of exploded metal droplets in the oxygen impact zone
  - ii) Vaporization
2. During the blowing period, the majority of the fume (approximately 90% by weight) originates from the oxidation of a fine metal spray produced by the explosive decarburization of larger metal droplets.
3. Vaporization accounts for less than 10% (by weight) of the fume iron losses during the blowing period.
4. Both direct vaporization of the metal bath and vaporization of bubble films and metal droplet spray are occurring.
5. During the pre-ignition and reblow periods, the vaporization mechanism accounts for as much as 50% (by weight) of the fume generated.
6. The fume rate decreases with increasing time into the blow, with approximately 60% of the fume iron emissions being lost during the first one-third of the blowing time.

7. Process variables that influence the fume rate are: carbon content of the metal bath, slag volume, metal bath temperature and lance practice.

BIBLIOGRAPHY

1. Rajkumar, R. and Krishna, P., Trans. Indian Institute of Metals, June 1969, p. 16.
2. Krichevtsov, E., Stal, Feb. 1970, p. 99.
3. Hopkins, D.W. et al, Ironmaking and Steelmaking (Quarterly), 1, 1975, p. 25.
4. Sargent, K.K., "Recent Advances with Oxygen in Iron and Steelmaking", Butterworth and Co., London, 1964, p. 296.
5. B.O.F. Steelmaking, Vol. 3, Iron and Steel Society of AIME, New York, 1976.
6. Harrop, J.A., Pickin, G.A., Steelmaking Proceedings AIME, Pittsburgh, 1977, p. 174.
7. Ito Tanaka et al, Steelmaking Proceedings AIME, Pittsburgh, 1977, p. 67.
8. Hoff, H., Stahl und Eisen, 81, 1961, p. 562.
9. Ontario Ministry of the Environment.
10. Lait, J.E., et al, McMaster Symposium on Iron and Steel-making No. 4, McMaster University Press, 1976, p. 8-1.
11. Afanasev, M.V. et al, Stal, Nov. 1965, p. 880.
12. Nikami, K. et al, Tetsu to Hagne, 52, 1966, p. 1491.
13. Baum, J., Steelmaking Proceedings AIME, Pittsburgh, 1977, p. 87.
14. B.O.F. Steelmaking, Vol. 4, ISS-AIME, New York, 1976.
15. Wheeler, D.H., A.P.C.A. Journal, 18, 1968, p. 98.
16. Price, D.J., "Chemical Metallurgy of Iron and Steel", I.S.I. Publication, 1973, p. 8.
17. Meyer, H.W., J.I.S.I., 207, 1969, p. 781.
18. Okhotskii, V.B., Steel in the U.S.S.R., 3, 1973, p. 473.
19. Walker, R.D. and Anderson, D., Iron and Steel, 45, 1972, p. 271.
20. Lange, K.W., and Rees, H., Arch. Eisen, 44, 1973, p. 813.

21. Distin, P.A. et al, J.I.S.I., 206, 1968, p. 821.
22. Morris, J.P. et al, Journal of Metals, 18, 1966, p. 803.
23. Physical Chemistry of Metals in Metallurgy, Vol. 2, Richardson, F.D., Academic Press, New York, 1974.
24. Laciak, S., Master of Engineering Thesis, McMaster University, 1977.
25. Ellis, A.F. and Glover, J., J.I.S.I., 209, 1971, p. 593.
26. Kosmider, H. et al, Stahl und Eisen, 74, 1954, p. 1045.
27. Bogdandy, L. and Pantke, D., Stahl und Eisen, 78, 1958, p. 792.
28. Naeser, G. et al, Stahl und Eisen, 75, 1955, p. 1244.
29. Urbain, G., Revue de Metallurgie, 59, 1962, p. 725.
30. Kocho, V.S. et al, Steel in the U.S.S.R., 1, 1971, p. 614.
31. Kawakami, K., Journal of Metals, 18, 1966, p. 836.
32. Beitelman, L.S. et al, Stal in English, 3, 1963, p. 271.
33. JANAF Thermochemical Tables, Second Edition, U.S. Department of Commerce, 1971.
34. Turkdogan, E.T. and Leake, L.E., J.I.S.I., 192, 1959, p. 162.
35. Brewer, L. and Mastick, D.F., Journal of Chemical Physics, 19, 1951, p. 834.
36. Wartenberg, H., Archiv fur das Eisenhüttenwesen, 1959, p. 585.
37. Meldan, R., Archiv fur das Eisenhüttenwesen, 1956, p. 673.
38. Kohlemeyer, E.J. and Spandou, H., Archiv fur das Eisenhüttenwesen, 18, 1944, p. 1.
39. Bates, R.E., J.I.S.I., 201, 1963, p. 747.
40. Hulholland, E.W. et al, J.I.S.I., 211, 1973, p. 632.
41. Baker, L.A. and Ward, R.G., J.I.S.I., 205, 1967, p. 714.
42. See, J.B. and Warner, N.A., J.I.S.I., 211, 1973, p. 44.
43. Rodis, P.G., J.I.S.I., 211, 1973, p. 53.

44. Baker, L.A. et al, Transactions of the Metals Society of AIME, 239, 1967, p. 857.
45. Peregudov, A.S. et al, Steel in the U.S.S.R., 4, 1974, p. 24.
46. Li, et al, Trans. AIME, 230, 1964, p. 71.
47. Nomura, H. and Mori, K., Trans. ISIJ, 13, 1973, p. 325.
48. Nomura, H. and Mori, K., Trans. ISIJ, 13, p. 265.
49. Turkdogan, E.T. et al, Journal of Metals, 14, 1962, p. 521.
50. Swisher, J.H. and Turkdogan, E.T., Trans. AIME, 239, 1967, p. 602.
51. Goto, K. et al, Trans. AIME, 245, 1969, p. 293.
52. Newitt, D.M. et al, Trans. Inst. Chem. Engrs., 32, 1954, p. 244.
53. Rosler, R.S. and Stewart, G.H., J. Fluid Mech., 31, 1968, p. 163.
54. Molloy, N.A., JISI, 208, 1970, p. 943.
55. Kun Li, JISI, 196, 1960, p. 275.
56. Kapalun, P.R. et al, Izv. VUZ Chem. Met., 1974, p. 43.
57. Jawoiskii, V.I. et al, Steel in the U.S.S.R., 4, 1974, p. 20.
58. Baptizanskii, V.I. et al, Steel in the U.S.S.R., 3, 1973, p. 14.
59. Afanasev, S.G. et al, Steel in the U.S.S.R., 1, 1971, p. 515.
60. Baptizanskii, V.I. and Paniotov, Y.S., Steel in the U.S.S.R., 4, 1974, p. 801.
61. Chernyatevich, A.G. et al, Steel in the U.S.S.R., 5, 1975, p. 79.
62. Okhotskii, V.B. et al, Steel in the U.S.S.R., 2, 1972, p. 443.
63. Ogryzkin, E.M., Ijvest. Akad. Nauk. SSSR, 1963, p. 17.
64. Yakovlev, V.V. and Filippov, S.I., Steel in the U.S.S.R., 2, 1972, p. 274.

65. Hartog, H.W. et al, C.R.M., 37, 1973, p. 13.
66. Bondarenko, V.P. et al, Steel in the U.S.S.R., 1, 1971, p. 785.
67. Asai, S. and Muchi, I., Trans. ISIJ, 11, 1971, p. 107.
68. Baptizanskii, V.I. et al, Steel in the U.S.S.R., 5, 1975, p. 71.
69. Ende, H., and Liestmann, W.D., Stahl und Eisen, 1965, p. 721.
70. Rossi, G. and Perrin, A., JISI, 207, 1969, p. 1365.
71. Bogdandy, L., Archiv. fur das Eisenhüttenwesen, 1961, p. 287.
72. Winklepleck, R.G. et al, Steel in the U.S.S.R., 5, 1975, p. 79.
73. Afanasev, S.G. et al, Stal, October 1960, p. 719.
74. Didkovskii, V.K. et al, Stal, Jan. 1967, p. 18.
75. Okhotskii, V.B. and Gorbik, A.S., Izvestiya VUZ Chermaya Metallurgiya, Oct. 1974, p. 48.
76. Munro, A.J. and Mosdin, E.G., Journal of the Institute of Fuel, 1971, p. 156.
77. Rengstorff, G.W., Proc. National Open Hearth Steel Committee of AIME, 204, 1962, p. 45.
78. Trentini, B., JISI, 195, 1960, p. 464.
79. Meyer, F. and Kaell, N., McMaster Symposium on Iron and Steelmaking No. 4, McMaster University Press, 1976, p. 5-1.
80. Nilles, P. and Holper, R., C.R.M., 35, 1973, p. 23.
81. Chatterjee, A. et al, Ironmaking and Steelmaking, 3, 1976, p. 21.
82. Stairmond, C.T., Trans. Instn. Chem. Engrs., 29, 1951, p. 18.
83. Little, A.D., American Gas Association, Project NFX-12, Project PF-15, New York, Nov. 1957.
84. ASTM Designation, D2009-65.

85. Dofasco Internal Report, F. Goetz, 1976.
86. Allen, T., Particle Size Measurement, Chapman and Hall, London, 1974.
87. Cheslak, F.R. et al, J. Fluid Mech., 36, 1969, p. 55.
88. Sharma, S.K. et al, Iron and Steelmaker, 4, July 1977, p. 7.
89. Turkdogan, E.T., Chem. Eng. Sci., 21, 1966, p. 1133.
90. Yamada, K. et al, "The Role of Slag in the Basic Oxygen Steelmaking Process", W-K Lu (Ed), McMaster University Press, Hamilton, 1976.
91. Dofasco Internal Report, R. Taylor, 1979.



APPENDIX AMAXIMUM PARTICLE SIZE CARRIED IN GAS CLEANING SYSTEM

All the particles in the gas collection system are acted on by the drag force ( $F_D$ ) of the moving gases. If this drag force is large enough to overcome the gravitational force on a particle, then that particle will be carried along with the gases.

From Stokes law an expression for the drag force on a spherical particle is: (All symbols are defined in Table A-I).

$$F_D = C_D \rho_g U_g^2 \frac{\pi d^2}{8} \quad (A-1)$$

The gravitational force is:

$$F_G = \frac{\pi d^3}{6} \rho_s G \quad (A-2)$$

The condition that must be satisfied to determine the maximum particle size that can be carried by the gas stream is:

$$F_D > F_G \quad (A-3)$$

The drag coefficient ( $C_D$ ) is a function of the particles Reynolds Number ( $Re$ ). The Reynolds Number can be expressed as:

$$Re = \frac{U_g \rho_g d}{\mu} \quad (A-4)$$

Relationships to determine the drag coefficient for various ranges of Reynolds Number are listed in Table A-II. These equations are of the form:

$$C_D = \frac{C_1}{Re} + \frac{C_2}{Re^2} + C_3 \quad (A-5)$$

where  $C_1$ ,  $C_2$ , and  $C_3$  are constants.

Substituting (A-1), (A-2), (A-4) and (A-5) in (A-3) gives:

$$+ \frac{4}{3} \rho_s G d^3 + C_3 \rho_g U_g^2 d^2 + \frac{C_1 \mu U_g d}{\rho_g} > 0 \quad (A-6)$$

This equation can then be solved to determine the maximum particle diameter (d):

The following assumptions and data are used:

### Assumptions

1. The particles in question are iron oxide ( $\text{Fe}_x\text{O}_y$ ).
2. The maximum particle size is in the range 10  $\mu\text{m}$ .

### Data

1. The gas velocity is 2500  $\text{cm}\cdot\text{s}^{-1}$ .
2. The gas density is .02  $\text{g}\cdot\text{cm}^{-3}$ .
3. The dynamic gas viscosity ( $\mu$ ) is  $6.16 \times 10^{-4} \text{ g}\cdot\text{cm}^{-1}\cdot\text{sec}^{-1}$ .
4. The value of the gravitational constant (G) is 981  $\text{cm}\cdot\text{sec}^{-2}$ .
5. The density of iron oxide is 5  $\text{g}\cdot\text{cm}^{-3}$ .

### Calculations

1. The approximate Reynolds Number (to determine the constants for  $C_D$ )

$$Re = \frac{U_g \rho_g d}{\mu} = \frac{2500 \times .02 \times 10 \times 10^{-4}}{6.16 \times 10^{-4}}$$

$$= 81.2$$

Assuming  $Re$  is in the range 100 to 1000, then from Table A-II, the coefficients in equation (A-5) are:

$$C_1 = 98.33$$

$$C_2 = -2778$$

$$C_3 = .3644$$

2. The maximum particle diameter:

Substituting all of the data into equation (A-6) gives:

$$+ \frac{4}{3} \times 5 \times 981 d^3 + .3644 \times .02 \times (2500)^2 d^2$$

$$+ 98.33 \times 6.16 \times 10^{-4} \times 2500 d - \frac{2778 \times (6.16 \times 10^{-4})^2}{.02} > 0$$

$$\text{or } + 6540 d^3 + 45550 d^2 + 151.4 d - .05 \geq 0$$

For solution this equation can be simplified to:

$$+ 6540 d^2 + 45550 d + 151.4 \geq 0$$

The solution is:

$$d \leq .0033 \text{ cm} \quad (33 \mu\text{m})$$

TABLE A-I

Symbols

<u>Symbol</u>	<u>Definition</u>	<u>Units</u>
$C_1, C_2, C_3$	constants	unitless
$C_D$	drag coefficient	unitless
$d$	particle diameter	cm
$F_D$	drag force	$\text{g}\cdot\text{cm}\cdot\text{s}^{-2}$
$F_G$	gravitational force	$\text{g}\cdot\text{cm}\cdot\text{s}^{-2}$
$G$	gravitational constant	$\text{cm}\cdot\text{s}^{-2}$
$Re$	Reynolds Number	unitless
$U_g$	Gas velocity	$\text{cm}\cdot\text{s}^{-1}$
$\rho_g$	density of gas	$\text{g}\cdot\text{cm}^{-3}$
$\rho_s$	density of solid particles	$\text{g}\cdot\text{cm}^{-3}$
$\mu$	dynamic gas viscosity	$\text{g}\cdot\text{cm}^{-1}\cdot\text{s}^{-1}$

TABLE A-II

Drag Coefficients as a function of  $Re^*$ 

$$C_d = 24.0/R_N \text{ for } R_N < 0.1,$$

$$C_d = 22.73/R_N + 0.0903/R_N^2 + 3.69 \text{ for } 0.1 < R_N < 1.0,$$

$$C_d = 29.1667/R_N - 3.8889/R_N^2 + 1.222 \text{ for } 1.0 < R_N < 10.0,$$

$$C_d = 46.5/R_N - 116.67/R_N^2 + 0.6167 \text{ for } 10.0 < R_N < 100.0,$$

$$C_d = 98.33/R_N - 2778/R_N^2 + 0.3644 \text{ for } 100.0 < R_N < 1000.0,$$

$$C_d = 148.62/R_N - 4.75 \times 10^4/R_N^2 + 0.357 \text{ for } 1000.0 < R_N < 5000.0,$$

$$C_d = -490.546/R_N + 57.87 \times 10^4/R_N^2 + 0.46 \text{ for } 5000.0 < R_N < 10000.0,$$

$$C_d = -1682.5/R_N + 5.4167 \times 10^6/R_N^2 + 0.5191 \text{ for } 10000.0 < R_N < 50000.0.$$

\* Morsi and Alexander, J. Fluid Mech., 55, 1972, p. 193

APPENDIX BCHI-SQUARE TEST FOR DISTRIBUTION NORMALITY

The frequency distribution of a small number of measurements generally provides only sketchy information about the parent distribution whose characteristics are sought. The problem is to decide whether or not the experimental distribution can be satisfactorily assumed to be a sample from a normal parent distribution.

A very useful quantitative test for the goodness of fit of the experimental distribution is the so-called  $X^2$  (Chi-Square) test. The  $X^2$  test gives a single numerical measure of the overall goodness of fit for the entire range of deviations. In a general view, the  $X^2$  test determines the probability that a purely random sample set of measurements taken from the assumed model parent distribution would show better agreement with the model than is shown by the actual set. This probability is called the level of significance of the distribution.

In performing this test, a minimum of about 20 measurements is normally required. The mean and standard deviation of the data points are first obtained. The entire range of observations is divided into  $M$  intervals, normally of the same size. Ideally, each interval should contain more than five measurements, but this is not possible with small data sets. In this test, the observed frequencies ( $f_{obs}$ ) in the

intervals are compared with the theoretical model values ( $f_{th}$ ). These theoretical values are obtained from a normal distribution model based on the calculated mean and standard deviation values. The quantity  $X^2$  is defined as the sum:

$$X^2 = \sum_{j=1}^M \left[ \frac{(f_{obs})_j - (f_{th})_j}{(f_{th})_j} \right]^2$$

Based on this  $X^2$  value and  $M-3$  degrees of freedom, the level of significance of the experimental distribution can be obtained from Table B-I.

An example of a computation of the level of significance is now given.

#### EXAMPLE

1. DATA SET: Number of observations =  $N = 18$

13.5	13.8	11.2
14.5	14.5	10.8
17.8	12.8	13.0
16.4	15.5	14.1
17.6	11.9	14.1
15.8	14.5	12.3

$$\text{Mean} = \bar{X} = \frac{\sum X}{N} = 14.12$$

$$\text{Standard Deviation} = s = \left[ \frac{\sum (\bar{X} - X)^2}{N - 1} \right]^{0.5} = 1.99$$

2. FREQUENCY DISTRIBUTION:

<u>Date Range</u>	<u>Number of Observations in Interval</u>
10-12	3
12-14	5
14-16	7
16-18	3

3. X<sup>2</sup> TEST

<u>Range</u>	<u>f<sub>obs</sub></u>	<u>U<sub>i</sub></u>	<u>P<sub>c<sub>i</sub></sub></u>	<u>P<sub>i</sub></u>	<u>NP<sub>i</sub></u>	<u>X<sup>2</sup></u>
10-12	3	-1.0644	0.1436	0.1436	2.585	0.066
12-14	5	-0.0588	0.4766	0.3330	5.994	0.165
14-16	7	0.9467	0.8271	0.3505	6.309	0.076
16-18	3	1.9522	0.9745	0.1474	2.653	0.045
				<u>0.9745</u>	<u>17.541</u>	<u>0.352</u>

$$U = \frac{X_i^1 - \bar{X}}{s} \quad \text{where } X_i^1 = \text{right hand interval end point}$$

$$P_{c_i} = 0.5 \pm (U_i) \quad \text{Table B-II}$$

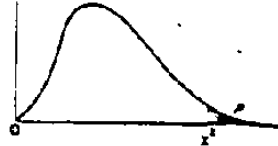
$$P_i = P_{c_i} - P_{c_{i-1}} \quad (P_{c_0} = 0)$$

$$X^2 = \frac{(NP_i - f_{obs})^2}{NP_i}$$

The total X<sup>2</sup> value is .0.354. The degrees of freedom are M-3 or 1. Therefore, from Table B-I, the level of significance > 50%.

TABLE B-I  
VALUES OF  $\chi^2$

$P$  equals the probability of exceeding a given value of  $\chi^2$  corresponding to a degree of freedom.



$P$	0.99	0.95	0.90	0.80	0.70	0.60	0.50	0.40	0.30	0.20	0.10	0.05	0.01
1	0.0001	0.0006	0.0009	0.0118	0.455	1.708	3.841	5.024	6.635	7.879	9.488	10.828	16.013
2	0.0201	0.0507	0.1013	0.2108	0.575	1.890	3.000	3.841	4.605	5.581	6.708	7.378	10.597
3	0.0717	0.1415	0.2167	0.3518	0.713	1.924	2.366	3.000	3.841	4.605	5.581	6.708	10.597
4	0.2147	0.2978	0.3745	0.4786	0.878	2.003	1.924	2.366	3.000	3.841	4.605	5.581	10.597
5	0.3546	0.4558	0.5379	0.6368	1.064	2.076	1.676	1.924	2.366	3.000	3.841	4.605	10.597
6	0.5541	0.6758	0.7793	0.8770	1.279	2.132	1.509	1.676	1.924	2.366	3.000	3.841	10.597
7	0.8123	0.9378	1.0541	1.1629	1.515	2.177	1.370	1.509	1.676	1.924	2.366	3.000	10.597
8	1.0645	1.2017	1.3197	1.4216	1.764	2.209	1.252	1.370	1.509	1.676	1.924	2.366	10.597
9	1.3121	1.4601	1.5795	1.6758	2.015	2.230	1.146	1.252	1.370	1.509	1.676	1.924	10.597
10	1.5558	1.7145	1.8350	1.9213	2.278	2.242	1.050	1.146	1.252	1.370	1.509	1.676	10.597
11	1.8029	1.9724	2.0941	2.1713	2.547	2.246	0.963	1.050	1.146	1.252	1.370	1.509	10.597
12	2.0530	2.2337	2.3565	2.4253	2.823	2.242	0.884	0.963	1.050	1.146	1.252	1.370	10.597
13	2.3055	2.4973	2.6212	2.6813	3.106	2.229	0.812	0.884	0.963	1.050	1.146	1.252	10.597
14	2.5618	2.7654	2.8903	2.9420	3.395	2.212	0.748	0.812	0.884	0.963	1.050	1.146	10.597
15	2.8214	3.0383	3.1691	3.2122	3.690	2.191	0.691	0.748	0.812	0.884	0.963	1.050	10.597
16	3.0839	3.3161	3.4478	3.4883	4.000	2.166	0.641	0.691	0.748	0.812	0.884	0.963	10.597
17	3.3491	3.5988	3.7315	3.7725	4.323	2.138	0.597	0.641	0.691	0.748	0.812	0.884	10.597
18	3.6168	3.8864	4.0151	4.0565	4.660	2.107	0.558	0.597	0.641	0.691	0.748	0.812	10.597
19	3.8868	4.1789	4.3076	4.3494	5.010	2.074	0.524	0.558	0.597	0.641	0.691	0.748	10.597
20	4.1588	4.4763	4.6098	4.6520	5.372	2.038	0.494	0.524	0.558	0.597	0.641	0.691	10.597
21	4.4326	4.7786	4.9141	4.9567	5.746	2.000	0.467	0.494	0.524	0.558	0.597	0.641	10.597
22	4.7081	5.0857	5.2219	5.2649	6.132	1.960	0.442	0.467	0.494	0.524	0.558	0.597	10.597
23	4.9851	5.3975	5.5353	5.5787	6.530	1.918	0.419	0.442	0.467	0.494	0.524	0.558	10.597
24	5.2635	5.7140	5.8529	5.8967	6.940	1.874	0.398	0.419	0.442	0.467	0.494	0.524	10.597
25	5.5432	6.0352	6.1752	6.2194	7.362	1.828	0.379	0.398	0.419	0.442	0.467	0.494	10.597
26	5.8241	6.3611	6.5021	6.5467	7.796	1.780	0.361	0.379	0.398	0.419	0.442	0.467	10.597
27	6.1061	6.6917	6.8337	6.8787	8.242	1.730	0.344	0.361	0.379	0.398	0.419	0.442	10.597
28	6.3891	7.0270	7.1700	7.2154	8.700	1.678	0.328	0.344	0.361	0.379	0.398	0.419	10.597
29	6.6731	7.3670	7.5110	7.5568	9.170	1.624	0.313	0.328	0.344	0.361	0.379	0.398	10.597
30	6.9581	7.7117	7.8567	7.9029	9.652	1.568	0.300	0.313	0.328	0.344	0.361	0.379	10.597
31	7.2441	8.0611	8.2071	8.2537	10.146	1.510	0.288	0.300	0.313	0.328	0.344	0.361	10.597
32	7.5311	8.4151	8.5621	8.6091	10.652	1.450	0.277	0.288	0.300	0.313	0.328	0.344	10.597
33	7.8191	8.7737	8.9217	8.9691	11.170	1.388	0.267	0.277	0.288	0.300	0.313	0.328	10.597
34	8.1081	9.1370	9.2859	9.3337	11.700	1.324	0.258	0.267	0.277	0.288	0.300	0.313	10.597
35	8.3981	9.5050	9.6549	9.7029	12.242	1.258	0.250	0.258	0.267	0.277	0.288	0.300	10.597
36	8.6891	9.8777	10.0286	10.0769	12.796	1.190	0.243	0.250	0.258	0.267	0.277	0.288	10.597
37	8.9811	10.2551	10.4070	10.4557	13.362	1.120	0.237	0.243	0.250	0.258	0.267	0.277	10.597
38	9.2741	10.6372	10.7899	10.8391	13.940	1.048	0.232	0.237	0.243	0.250	0.258	0.267	10.597
39	9.5681	11.0240	11.1829	11.2317	14.530	0.974	0.228	0.232	0.237	0.243	0.250	0.258	10.597
40	9.8631	11.4155	11.5754	11.6245	15.132	0.900	0.225	0.228	0.232	0.237	0.243	0.250	10.597
41	10.1591	11.8117	11.9726	12.0221	15.746	0.826	0.222	0.225	0.228	0.232	0.237	0.243	10.597
42	10.4561	12.2126	12.3755	12.4235	16.372	0.752	0.220	0.222	0.225	0.228	0.232	0.237	10.597
43	10.7541	12.6182	12.7831	12.8315	17.010	0.678	0.218	0.220	0.222	0.225	0.228	0.232	10.597
44	11.0531	13.0285	13.1944	13.2423	17.660	0.604	0.216	0.218	0.220	0.222	0.225	0.228	10.597
45	11.3531	13.4435	13.6154	13.6637	18.322	0.530	0.215	0.216	0.218	0.220	0.222	0.225	10.597
46	11.6541	13.8642	14.0414	14.0925	19.000	0.456	0.214	0.215	0.216	0.218	0.220	0.222	10.597
47	11.9561	14.2906	14.4724	14.5327	19.690	0.382	0.213	0.214	0.215	0.216	0.218	0.220	10.597
48	12.2591	14.7227	14.9084	14.9733	20.390	0.308	0.212	0.213	0.214	0.215	0.216	0.218	10.597
49	12.5631	15.1605	15.3494	15.4137	21.100	0.234	0.211	0.212	0.213	0.214	0.215	0.216	10.597
50	12.8681	15.6040	15.7944	15.8783	21.820	0.160	0.210	0.211	0.212	0.213	0.214	0.215	10.597
51	13.1741	16.0532	16.2454	16.3627	22.550	0.086	0.209	0.210	0.211	0.212	0.213	0.214	10.597
52	13.4811	16.5081	16.6934	16.7677	23.290	0.012	0.208	0.209	0.210	0.211	0.212	0.213	10.597
53	13.7891	16.9687	17.1544	17.2733	24.040	0.000	0.207	0.208	0.209	0.210	0.211	0.212	10.597
54	14.0981	17.4350	17.6414	17.7793	24.800	0.000	0.206	0.207	0.208	0.209	0.210	0.211	10.597
55	14.4081	17.9070	18.1534	18.2857	25.570	0.000	0.205	0.206	0.207	0.208	0.209	0.210	10.597
56	14.7191	18.3847	18.6714	18.8027	26.350	0.000	0.204	0.205	0.206	0.207	0.208	0.209	10.597
57	15.0311	18.8681	19.1954	19.3203	27.140	0.000	0.203	0.204	0.205	0.206	0.207	0.208	10.597
58	15.3441	19.3572	19.7294	19.8387	27.940	0.000	0.202	0.203	0.204	0.205	0.206	0.207	10.597
59	15.6581	19.8520	20.2694	20.3577	28.750	0.000	0.201	0.202	0.203	0.204	0.205	0.206	10.597
60	15.9731	20.3525	20.8154	20.8773	29.570	0.000	0.200	0.201	0.202	0.203	0.204	0.205	10.597
61	16.2891	20.8587	21.3674	21.3973	30.400	0.000	0.199	0.200	0.201	0.202	0.203	0.204	10.597
62	16.6061	21.3706	21.9254	21.9177	31.240	0.000	0.198	0.199	0.200	0.201	0.202	0.203	10.597
63	16.9241	21.8882	22.4894	22.4893	32.090	0.000	0.197	0.198	0.199	0.200	0.201	0.202	10.597
64	17.2431	22.4115	23.0594	23.0607	32.950	0.000	0.196	0.197	0.198	0.199	0.200	0.201	10.597
65	17.5631	22.9405	23.6354	23.6377	33.820	0.000	0.195	0.196	0.197	0.198	0.199	0.200	10.597
66	17.8841	23.4752	24.2174	24.2407	34.700	0.000	0.194	0.195	0.196	0.197	0.198	0.199	10.597
67	18.2061	24.0156	24.8054	24.8307	35.590	0.000	0.193	0.194	0.195	0.196	0.197	0.198	10.597
68	18.5291	24.5617	25.3994	25.4277	36.490	0.000	0.192	0.193	0.194	0.195	0.196	0.197	10.597
69	18.8531	25.1135	25.9994	26.0267	37.400	0.000	0.191	0.192	0.193	0.194	0.195	0.196	10.597
70	19.1781	25.6710	26.6054	26.6377	38.320	0.000	0.190	0.191	0.192	0.193	0.194	0.195	10.597
71	19.5041	26.2342	27.2174	27.2707	39.250	0.000	0.189	0.190	0.191	0.192	0.193	0.194	10.597
72	19.8311	26.8031	27.8354	27.8857	40.190	0.000	0.188	0.189	0.190	0.191	0.192	0.193	10.597
73	20.1591	27.3777	28.4594	28.4427	41.140	0.000	0.187	0.188	0.189	0.190	0.191	0.192	10.597
74	20.4881	27.9580	29.0894	29.0907	42.100	0.000	0.186	0.187	0.188	0.189	0.190	0.191	10.597
75	20.8181	28.5440	29.7254	29.6977	43.070	0.000	0.185	0.186	0.187	0.188	0.189	0.190	10.597
76	21.1491	29.1357	30.3674	30.3107	44.050	0.000	0.184	0.185	0.186	0.187	0.188	0.189	10.597
77	21.4811	29.7331	31.0154	30.9297	45.040	0.000	0.183	0.184	0.185	0.186	0.187	0.188	10.597
78	21.8141	30.3362	31.6694	31.5547	46.040	0.000	0.182	0.183	0.184	0.185	0.186	0.187	10.597
79	22.1481	30.9450	32.3294	32.1857	47.050	0.000	0.181	0.182	0.183	0.184	0.185	0.186	10.597
80	22.4831	31.5595	32.9954	32.8227	48.070	0.000	0.180	0.181	0.182	0.183	0.184	0.185	



## APPENDIX C

Size Analysis Reproducibility Data  
(12 Minute Fume)

Table	Description
C1	Sample A
C2	Sample B
C3	Sample C

TABLE C1

SIZE ANALYSIS OF 12 MINUTE FUME SAMPLE "A"

Class Size ( $\mu\text{m}$ )	Actual Frequency	Relative Frequency (%)	Volume ( $\mu\text{m}^3$ )	Weight Percent
0 - .1	499	38.62	.033	.52
.1 - .2	463	35.84	.818	13.02
.2 - .3	226	17.49	1.847	29.41
.3 - .4	73	5.62	1.639	26.07
.4 - .5	22	1.70	1.050	16.70
.5 - .6	7	.54	.610	9.70
.6 - .7	2	.16	.288	4.58
.7 - .8	0	0	0	0
Total	1292	100.0	6.285	100.0

Mean particle size (wt. % distribution) = .36  $\mu\text{m}$

TABLE C2

SIZE ANALYSIS OF 12 MINUTE FUME SAMPLE "B"

Class Size ( $\mu\text{m}$ )	Actual Frequency	Relative Frequency (%)	Volume ( $\mu\text{m}^3$ )	Weight Percent
0 - .1	494	41.83	.033	.45
.1 - .2	406	34.38	.717	9.91
.2 - .3	149	12.62	1.218	16.83
.3 - .4	84	7.11	1.886	26.07
.4 - .5	33	2.79	1.574	21.76
.5 - .6	9	.76	.789	10.91
.6 - .7	4	.34	.575	7.95
.7 - .8	2	.17	.442	6.10
Total	1181	100.0	7.234	100.0

Mean particle size (wt. % distribution) = .40  $\mu\text{m}$

TABLE C3

SIZE ANALYSIS OF 12 MINUTE FUME SAMPLE "C"

Class Size ( $\mu\text{m}$ )	Actual Frequency	Relative Frequency (%)	Volume ( $\mu\text{m}^3$ )	Weight Percent
0 - .1	483	33.54	.032	.35
.1 - .2	509	35.34	.899	9.70
.2 - .3	263	18.26	2.151	23.22
.3 - .4	142	9.86	3.188	34.41
.4 - .5	27	1.89	1.288	13.90
.5 - .6	12	.83	1.053	11.38
.6 - .7	3	.21	.431	4.65
.7 - .8	1	.07	.221	2.38
Total	1440	100.0	9.263	100.0

Mean particle size (wt. % distribution) = .37  $\mu\text{m}$

## APPENDIX D

## Size Analysis Data for Fume Samples

Table	Description
D1	One minute sample
D2	Five minute sample
D3	Eight minute sample
D4	Fifteen minute sample
D5	Twenty minute sample
D6	Reblow sample
D7	Pre-ignition sample

TABLE D1

SIZE ANALYSIS OF ONE MINUTE FUME SAMPLE

Class Size ( $\mu\text{m}$ )	Actual Frequency	Relative Frequency (%)	Volume ( $\mu\text{m}^3$ )	Weight Percent
.0 - .1	507	30.97	.033	.36
.1 - .2	678	41.42	1.198	13.62
.2 - .3	314	19.18	2.568	29.19
.3 - .4	104	6.32	2.335	26.54
.4 - .5	20	1.22	.954	10.84
.5 - .6	8	.49	.697	7.92
.6 - .7	4	.25	.570	6.48
.7 - .8	2	.13	.442	5.05
TOTAL	1637	100.0	8.797	100.0

Mean particle size (wt. % distribution) = .38  $\mu\text{m}$

TABLE D2

SIZE ANALYSIS OF FIVE MINUTE FUME SAMPLE

Class Size ( $\mu\text{m}$ )	Actual Frequency	Relative Frequency (%)	Volume ( $\mu\text{m}^3$ )	Weight Percent
0 - .1	516	35.42	.034	.35
.1 - .2	482	33.08	.852	8.90
.2 - .3	281	19.29	2.299	24.02
.3 - .4	122	8.37	2.739	28.63
.4 - .5	39	2.68	1.861	19.45
.5 - .6	13	.89	1.132	11.83
.6 - .7	3	.20	.431	4.51
.7 - .8	1	.07	.221	2.31
TOTAL	1457	100.0	9.569	100.0

Mean particle size (wt. % distribution) = .37  $\mu\text{m}$

TABLE D3

SIZE ANALYSIS OF EIGHT MINUTE FUME SAMPLE

CLASS SIZE ( $\mu\text{m}$ )	ACTUAL FREQUENCY	RELATIVE FREQUENCY (%)	VOLUME ( $\mu\text{m}^3$ )	WEIGHT PERCENT
0 - .1	454	35.66	.030	.37
.1 - .2	485	38.10	.857	10.70
.2 - .3	197	15.48	1.612	20.13
.3 - .4	89	6.99	1.998	24.95
.4 - .5	31	2.44	1.479	18.47
.5 - .6	10	.79	.871	10.88
.6 - .7	5	.38	.719	8.98
.7 - .8	2	.16	.442	5.52
TOTAL	1273	100.0	8.008	100.0

Mean particle size (wt. % distribution) = .39  $\mu\text{m}$



TABLE D4

## SIZE ANALYSIS OF 15 MINUTE FUME SAMPLE

CLASS SIZE ( $\mu\text{m}$ )	ACTUAL FREQUENCY	RELATIVE FREQUENCY (%)	VOLUME ( $\mu\text{m}^3$ )	WEIGHT PERCENT
0 - .1	581	44.49	.038	.65
.1 - .2	437	33.46	.772	13.21
.2 - .3	194	14.85	1.590	27.21
.3 - .4	65	4.98	1.459	24.97
.4 - .5	20	1.53	.954	16.33
.5 - .6	6	.49	.526	9.07
.6 - .7	2	.15	.284	4.86
.7 - .8	1	.07	.221	3.70
TOTAL	1306	100.0	5.844	100.0

Mean particle size (wt. % distribution) = .36  $\mu\text{m}$

TABLE D5

SIZE ANALYSIS OF 20 MINUTE FUME SAMPLE

CLASS SIZE ( $\mu\text{m}$ )	ACTUAL FREQUENCY	RELATIVE FREQUENCY (%)	VOLUME ( $\mu\text{m}^3$ )	WEIGHT PERCENT
0 - .1	422	40.20	.028	.48
.1 - .2	392	37.33	.693	11.90
.2 - .3	125	11.90	1.023	17.54
.3 - .4	72	6.85	1.616	27.77
.4 - .5	23	2.49	1.097	18.85
.5 - .6	9	.86	.789	13.56
.6 - .7	4	.38	.575	9.90
.7 - .8	0			
TOTAL	1050	100.0	5.821	100.0

Mean particle size (wt. % distribution) = .38  $\mu\text{m}$

TABLE D6

SIZE ANALYSIS OF REBLOW FUME SAMPLE

CLASS SIZE ( $\mu\text{m}$ )	ACTUAL FREQUENCY	RELATIVE FREQUENCY (%)	VOLUME ( $\mu\text{m}^3$ )	WEIGHT PERCENT
0 - .05	84	6.67	.0007	.02
.05 - .10	335	26.60	.0740	2.59
.10 - .15	409	32.49	.4182	14.62
.15 - .20	265	21.05	.7436	26.00
.20 - .25	99	7.86	.5904	20.65
.25 - .30	40	3.18	.4355	15.23
.30 - .35	18	1.45	.3235	11.32
.35 - .40	7	.55	.1933	6.76
.40 - .45	2	.15	.0804	2.81
TOTAL	1259	100.0	2.859	100.0

Mean particle size (wt. % distribution) = .23  $\mu\text{m}$

TABLE D7

SIZE ANALYSIS OF PRE-IGNITION FUME SAMPLE

CLASS SIZE ( $\mu\text{m}$ )	ACTUAL FREQUENCY	RELATIVE FREQUENCY (%)	VOLUME ( $\times 10$ ) ( $\mu\text{m}^3$ )	WEIGHT PERCENT
0 - .05	412	28.91	.034	.23
.05 - .10	536	37.61	1.184	8.04
.10 - .15	268	18.80	2.741	18.61
.15 - .20	136	9.54	3.816	25.92
.20 - .25	42	2.94	2.505	17.02
.25 - .30	20	1.40	2.178	14.97
.30 - .35	8	.56	1.438	9.77
.35 - .40	3	.24	.828	5.63
TOTAL	1425	100.0	14.72	100.0

Mean particle size (wt. % distribution) = .21  $\mu\text{m}$

## APPENDIX E

## Size Analysis Data for Slopping and Not-Slopping Fume Samples (15 minutes)

Table	Description
E1	Slopping fume sample
E2	Not-slopping fume sample

TABLE E1

SIZE ANALYSIS OF 15 MINUTE "SLOPPING" FUME SAMPLE

Class Size ( $\mu\text{m}$ )	Actual Frequency	Relative Frequency (%)	Volume ( $\mu\text{m}^3$ )	Weight Percent
0 - .1	394	29.03	.026	.25
.1 - .2	554	40.82	.982	9.53
.2 - .3	212	15.62	1.737	16.87
.3 - .4	131	9.65	2.934	28.54
.4 - .5	42	3.10	2.004	19.44
.5 - .6	15	1.10	1.307	12.68
.6 - .7	6	.44	.863	8.38
.7 - .8	2	.15	.442	4.28
TOTAL	1357	100.0	10.295	100.0

Mean particle size (wt. % distribution) = .40  $\mu\text{m}$

TABLE E2

## SIZE ANALYSIS OF 15 MINUTE "NOT SLOPPING" FUME SAMPLE

Class Size ( $\mu\text{m}$ )	Actual Frequency	Relative Frequency (%)	Volume ( $\mu\text{m}^3$ )	Weight Percent
0 - .1	563	43.27	.037	.62
.1 - .2	471	36.20	.832	13.94
.2 - .3	172	13.22	1.407	23.58
.3 - .4	64	4.92	1.437	24.08
.4 - .5	19	1.46	.906	15.19
.5 - .6	8	.62	.697	11.68
.6 - .7	3	.23	.431	7.23
.7 - .8	1	.08	.220	3.68
TOTAL	1301	100.0	5.967	100.0

Mean particle size (wt. % distribution) = .37  $\mu\text{m}$